Thèse présentée pour l'obtention du grade de

DOCTEUR de SORBONNE UNIVERSITÉ

Spécialité

Ingénierie / Systèmes Informatiques

École doctorale

Informatique, Télécommunication et Électronique Paris (ED130)

LARGE-SCALE OPTIMISATION OF 5G TERRESTRIAL AND NON-TERRESTRIAL NETWORKS

Henri Alam

Soutenue publiquement le : *17 Septembre 2025*

Devant un jury composé de :

Marios KOUNTOURIS, Professeur, Eurecom	*Président du Jury*
Beatriz SORET, Professeure, University of Malaga	*Rapporteuse*
Cicek CAVDAR, Professeure, KTH Royal Institute of Technology	*Rapporteuse*
Marceau COUPECHOUX, Professeur, Télécom Paris	*Examinateur*
Florian KALTENBERGER, Professeur, Eurecom	*Directeur de Thèse*

Abstract

This thesis addresses the optimisation of integrated Terrestrial and Non-Terrestrial Networks (TN-NTNs) in the context of 5G and beyond. As user demand for seamless, high-capacity connectivity intensifies, conventional terrestrial networks face limitations in coverage—particularly in remote or underserved regions. Non-Terrestrial Networks, including low-earth orbit (LEO) satellites, offer a promising complement by extending coverage and providing support for the terrestrial network. This work proposes and analyses three major contributions for the large-scale optimisation of TN-NTNs.

First, a utility-based optimisation framework is developed for high-traffic scenarios, enhancing user association and resource allocation by dynamically adjusting power levels and bandwidth sharing between terrestrial and satellite tiers. Then, the BLASTER algorithm is introduced, enabling traffic-aware management by optimising user association, macro base station activation, and bandwidth allocation throughout the day. This method significantly reduces energy consumption while enhancing sum log-throughput (SLT). Finally, a decentralised online learning framework based on the Bandit-feedback Constrained Online Mirror Descent (BCOMD) algorithm is presented. This distributed solution adapts to stochastic traffic conditions, ensuring Quality of Service (QoS) while reducing energy consumption without requiring centralised control.

Through theoretical analysis and extensive simulations, this thesis demonstrates how integrated TN-NTNs can dynamically adapt to varying traffic loads to optimise network performance, reduce energy usage, and provide robust connectivity across diverse environments.

Keywords: Non-Terrestrial Networks, Low Earth Orbit Satellites, Load Balancing, Energy Efficiency, Resource Allocation

Résumé

Cette thèse porte sur l'optimisation des réseaux intégrés terrestres et non-terrestres (TN-NTN) dans le contexte de la 5G et au-delà. Avec l'augmentation de la demande des utilisateurs pour une connectivité fluide et à haute capacité, les réseaux terrestres conventionnels montrent leurs limites en matière de couverture, notamment dans les régions éloignées ou mal desservies. Les réseaux non-terrestres, tels que les satellites en orbite terrestre basse (LEO), apparaissent comme un complément prometteur, en étendant la couverture et en apportant un soutien au réseau terrestre. Ce travail propose et analyse trois contributions majeures pour l'optimisation à grande échelle des réseaux TN-NTN.

Dans un premier temps, un cadre d'optimisation basé sur une fonction d'utilité est développé pour les scénarios de forte affluence, en améliorant l'association des utilisateurs et l'allocation des ressources grâce à un ajustement dynamique de la puissance d'émission et au partage de bande passante entre les couches terrestre et satellite. Ensuite, l'algorithme BLASTER est introduit ; il permet une gestion adaptative au trafic en optimisant l'association des utilisateurs, l'activation des stations de base macro et la répartition de la bande passante au fil de la journée. Cette méthode permet de réduire significativement la consommation d'énergie tout en améliorant le sum log-throughput (SLT). Enfin, un cadre d'apprentissage en ligne décentralisé, basé sur l'algorithme Bandit-feedback Constrained Online Mirror Descent (BCOMD), est présenté. Cette solution distribuée s'adapte aux variations stochastiques du trafic, garantit la qualité de service (QoS), et réduit la consommation d'énergie sans nécessiter de contrôle centralisé.

À travers des analyses théoriques et de nombreuses simulations, cette thèse démontre comment les réseaux intégrés TN-NTN peuvent s'adapter dynamiquement aux variations de charge pour optimiser les performances

du réseau, réduire la consommation énergétique et assurer une connectivité robuste dans des environnements variés.

Mots-clés: Réseaux non terrestres, Satellites en orbite terrestre basse, Répartition des charges, Efficacité énergétique, Allocation des ressources

Acknowledgements

First, I would like to take this opportunity to thank all those who have supported and accompanied me throughout this journey. I would not be where I am today without your guidance and/or encouragement.

I wish to express my deepest gratitude to my academic supervisor, Dr. Florian Kaltenberger, for his support and mentorship. Your genuine interest in my research and professional development, as well as your guidance through both the scientific and administrative aspects of my doctoral work, have been invaluable. I would also like to extend my sincere thanks to my industrial supervisor, Dr. Antonio de Domenico. Over the past four years, I have learnt a great deal from working alongside you. The confidence and trust you placed in me from the first time we met allowed me to grow both personally and professionally, and I am truly grateful for your continuous guidance and support. I could not have asked for a better mentor and colleague to share this journey with.

I would like to express my heartfelt appreciation to the NETOP team at Huawei. I am especially grateful to Harvey Bao for giving me the opportunity to embark on this journey and for making me feel truly part of such a wonderful team. David, you have been a true role model to me, and I will always fondly remember how you took me under your wing at the start of my professional journey, as well as our numerous conversations from which I learnt so much. Many thanks to Nicola, Ali, Mohammed, Wenjie, Tareq, and especially Fadhel, for your constant positivity and readiness to help whenever I needed it. You all helped create a work environment that became a cornerstone of my personal and professional growth. The memories we shared will always be cherished and never forgotten.
Lastly, I would like to thank my desk and PhD buddy Matteo. We suffered together and helped each other at tough times. I deeply value our friendship, and I am proud of what we have achieved together!

During my time at Huawei, I met many people whom I am proud to call my friends, and who made my time there so much more enjoyable. Therefore, I would like to thank Harenome, Samuel, Gianpietro, Charles, Marlene, Ruixuan and Dory for the great memories that we have created these past few years.

During my time at Huawei, I met many people whom I am proud to call my friends, and who made my time there so much more enjoyable. Therefore, I would especially like to thank Harenome, Alberto, Samuel, Gianpietro, Charles, Marlene, Ruixuan, and Dory for the wonderful memories we have shared over the past few years. Salma, you have been like a sister to me and I am so grateful for your advices. I will always cherish the endless chats we had in the coffee room. Lastly, I would like to thank Celena for your unwavering support over the past three years. We met at the perfect time, and your positivity and ever-lasting cheerfulness helped me through every rough patch of this journey. Keep spreading joy wherever you go, and never stop wearing that infectious smile of yours!

I want to wholeheartedly thank my childhood friends Aurélien, Yassine, Amine, and Zidane, who grew up with me and made my early years so memorable and full of joy. I would also like to express my sincere gratitude to my PIMA family — Ulysse, Nadym, Simon, Rachid, Ferhat, Youcef, Karim, Idriss, and Mazigh. I will always look back on our years together with great fondness, and each of you has helped me become a better person in your own way. It is often said that there are two families in life: the one you are born into and the one you create. You are all part of my family, and our bond goes far beyond friendship — may it continue for many years to come.

Finally, I would like to thank those behind my success, without whom none of this would have been possible: my family. Baba, you have shaped the man I am today, and I owe everything to you. I hope you are as proud of me as I am of you. Mama, you are my heartbeat — the beam of light that guided us through every hardship we faced. This is my way of giving back a drop of all that you have done for me. Bhai, thank you for being tough on me when needed, and for always showing such strength. I will never stop admiring the sheer focus and unrelenting discipline you display when you set your mind to something. I aspire to be a little more like you every day. Mohib, my partner

in mischief, never stop wearing that smile of positivity. Keep dreaming, keep working hard, and never forget that you are special, because you truly are.

I love you all.

List of Abbreviations

3GPP	3rd Generation Partnership Project
AI	artificial intelligence
ARQ	automatic repeat request
BCGA	block coordinate gradient ascent
BCOMD	bandit-feedback constrained online mirror descent
BER	bit error rate
BS	base station
CDF	cumulative distribution function
CHO	Conditional Handover
CIO	cell individual offset
CN	core network
DDPG	deep deterministic policy gradient
DL	downlink
EE	energy efficiency
eMBB	enhanced mobile broadband
GEO	geostationary orbit
GNSS	Global Navigation Satellite Systems
GSO	geostationary orbit
HAPS	high-altitude platform station
HARQ	hybrid automatic repeat request
HetNet	heterogeneous network
IoT	Internet of Things
KPI	key performance indicator
LEO	low-earth orbit
LoS	line-of-sight
LSTM	long short-term memory
LTE	long term evolution
MAB	multi-armed bandit
MBS	macro base station

MEO medium-earth orbit
MIMO multiple-input multiple-output
ML machine learning
mMTC massive machine type communication
mmWave millimeter-wave
NOMA non-orthogonal multiple access
NR new radio
NTN non-terrestrial network
O2I outdoor-to-indoor
OCC orthogonal cover codes
OMD online mirror descent
OPEX operational expenditure
PRB physical resource block
QoS Quality of Service
RACH random access channel
RAN radio access network
RE resource element
RF radio frequency
RL reinforcement learning
RLC radio link control
RRM radio resource management
RSRP reference signal received power
RTT round trip time
SI study item
SINR signal-to-interference-plus-noise ratio
SLT sum log-throughput
SMTC SSB measurement timing configuration
SNR signal-to-noise ratio
SON self-organising network
SSB synchronisation signal block
ST sum throughput
TA timing advance
TD3 twin delayed deep deterministic
TN terrestrial network
TN-NTN terrestrial and non-terrestrial network
UAV unmanned aerial vehicle

UE user equipment
UL uplink
WI work item

List of Figures

1.1 Breakdown of Network Operational Costs [6]. 24
1.2 Energy Consumption Distribution across Network Components [7]. 25
1.3 Daily Network Traffic Load Pattern [13]. 26

2.1 Different non-terrestrial network (NTN) technologies available [14]. 32
2.2 Integrated terrestrial and non-terrestrial network (TN-NTN) architecture (Inspired from [3]). 33
2.3 Bent-pipe and regenerative architectures [41]. 40
2.4 Earth-moving (left) and Earth-fixed (right) moving beams [42]. 41
2.5 Timeline of 3GPP Standardisation Advancements. 46

3.1 Representation of the area of study. 56
3.2 Distance and height parameter definitions for outdoor and indoor user equipments (UEs) [91]. 57
3.3 Representation of satellite elevation angle [44]. 60
3.4 Representation of the satellite positions considered for the area of study (in red). 61

4.1 Evolution of the bandwidth allocation proportion and the utility function of our framework. 77
4.2 CDFs of the UE RSRP, with (ε_{opt}, `3GPP-NTN`) and without ($\varepsilon = 0$, `3GPP-TN`) an active satellite. 79
4.3 CDFs of UE data rates for various bandwidth allocation settings. 80

5.1 Sum Log Throughput distribution achieved by `BLASTER` in high traffic for various $\lambda_{\max}$. 100
5.2 Sum Log Throughput distribution achieved by `BLASTER` in low traffic for various $\lambda_{\max}$. 101

5.3 Daily profile of the terrestrial network energy consumption achieved by BLASTER for various $\lambda_{\max}$. 102
5.4 Daily profile of the complexity of BLASTER and HEURISTIC. . . . 103
5.5 Average relative gain per iteration for BLASTER. 104
5.6 Daily profile of the proportion of UEs associated to the satellite network. 105
5.7 Daily profile of the sum log throughput. 106
5.8 Relative gain of the sum log throughput compared to 3GPP-TN. . 107
5.9 Daily profile of the terrestrial network (TN) energy consumption.108
5.10 Daily profile of the satellite energy consumption 109

6.1 Time-averaged cost for various window sizes. 125
6.2 Performance comparison of vanilla and windowed estimators under the BCOMD algorithm ($T_w = 50$). 126
6.3 Convergence of BCOMD: time-averaged cost and constraint violations. 127
6.4 Daily profile of the proportion of UEs associated to the satellite. 130
6.5 Daily profile of the TN energy consumption. 131
6.6 Daily profile of the proportion of unsatisfied UEs. 132
6.7 Daily network sum throughput (ST) profile. 133

List of Tables

3.1 Line-of-Sight Probability. 62
3.2 Shadow fading and clutter loss for urban and rural scenarios (S-band) [44, Section 6.6.2]. 63

4.1 Simulation parameters. 76
4.2 Data-rate analysis. 79

5.1 Simulation parameters. 99

6.1 Simulation parameters. 124
6.2 Most probable parameter values across time-of-day for BCOMD-NETOP.128

Contents

1 Introduction **23**

1.1 Context 23

1.2 Motivations and Contributions 25

1.3 Thesis Outline 27

2 Integrated TN-NTNs: Technologies, Challenges, and State-of-the-Art **31**

2.1 Perspectives on Integrated TN-NTN Architectures 31

2.2 Emerging Technologies for NTN 33

2.2.1 UAVs 33

Key Advantages 34

Related challenges 34

2.2.2 HAPS 35

Key Advantages 35

Related challenges 36

2.2.3 Satellites 37

Key Advantages 37

Related challenges 38

Payload Type 39

Beam Coverage Type 40

2.3 3GPP NR Standardisation Outline 41

2.3.1 Release 14 - Preliminary Phase 41

2.3.2 Release 15 (2016 - 2018) 42

2.3.3 Release 16 (2018-2020) 42

2.3.4 Release 17 (2020 - 2022) 43

2.3.5 Release 18 (2022 - 2024) 44

2.3.6 Release 19 (Ongoing) 45

2.4 Integrated TN-NTN Large-Scale Optimisation: State-of-the-art 47

2.4.1 Load Balancing in Integrated TN-NTN 47

2.4.2 Resource Allocation in Integrated TN-NTN 49
2.4.3 Interference Management in Integrated TN-NTN 50
2.4.4 Mobility and Cell Switching in Integrated TN-NTN . . 52
2.4.5 Summary and Open Challenges 53

3 System Model **55**
3.1 System Parameters and Notation 55
3.2 Channel modelling 56
3.2.1 Terrestrial Link 56
Line-of-sight Probability 56
Large-scale channel gain 57
3.2.2 Satellite Link 60
Elevation angle 60
Line-of-sight Probability 62
Large-scale channel gain 62
3.3 Signal-to-interference-plus-noise ratio 63
3.4 Data-rate 64
3.4.1 Full-buffer scenario 64
3.4.2 User-Specific scenario 64
3.5 Physical Resource Block Allocation 65
3.6 Energy Consumption model 65

4 Integrated TN-NTN in High Traffic: a Load Balancing Option **67**
4.1 Introduction 67
4.2 Contribution 67
4.3 Related Works 68
4.4 Problem Formulation 69
4.5 Utility Optimisation 70
4.5.1 Utility optimisation under fixed transmit power 70
4.5.2 Transmit power optimisation under fixed association . 73
4.6 Simulation Results & Analysis 75
Benchmarks 76
4.6.1 Framework convergence analysis 77
4.6.2 Network coverage analysis 78
4.6.3 UE rate analysis 78
4.7 Conclusion & Perspectives 81

5 BLASTER: A Tool for Traffic-Aware Network Optimisation 83
5.1 Introduction . . . 83
5.2 Contribution . . . 84
5.3 Related Works . . . 85
5.4 Problem Formulation . . . 86
5.5 Designed Solutions . . . 88
5.5.1 BLASTER . . . 88
Utility optimisation under fixed transmit power . . . 88
Transmit power optimisation under fixed association . 93
5.5.2 Heuristic development . . . 94
5.5.3 Complexity Analysis . . . 97
BLASTER complexity . . . 97
Heuristic complexity . . . 97
5.6 Simulation Results & Analysis . . . 98
Benchmarks . . . 98
5.6.1 Optimisation of the regularisation parameter . . . 99
5.6.2 Complexity and Convergence Analysis . . . 102
5.6.3 Impact of the Satellite Network on Traffic Distribution 103
5.6.4 Analysis on the Network Sum Log-Throughput . . . 105
5.6.5 Analysis on the Network Energy Consumption . . . 107
5.7 Conclusion & Perspectives . . . 110

6 A Distributed Approach to Integrated TN-NTN Optimisation Using Online Learning Methods 111
6.1 Introduction . . . 111
6.2 Contribution . . . 112
6.3 Related Works . . . 113
6.4 Problem Formulation . . . 114
6.5 Designed Solution . . . 116
6.5.1 Bandit-feedback Constrained Online Mirror Descent . . 117
6.5.2 BCOMD-NETOP . . . 118
6.5.3 Performance Guarantees . . . 119
6.5.4 Windowed Estimator . . . 122
6.6 Simulation Results & Analysis . . . 122
6.6.1 Simulation Settings and Benchmarks . . . 123
Settings . . . 123
Benchmarks . . . 123

6.6.2 Windowed Estimator Parameter Tuning and Performance Analysis . . . 125
6.6.3 Convergence Analysis . . . 127
6.6.4 Control Parameters Evolution Analysis . . . 128
6.6.5 Network Performance Analysis . . . 129
Impact of Satellite Network . . . 129
Analysis on Network Energy Consumption . . . 130
Analysis of UE Satisfaction . . . 131
Analysis on Network Sum Throughput . . . 133
6.7 Conclusion & Perspectives . . . 134

7 Conclusion & Perspectives **135**
BLASTER Convexity Analysis . . . 137
Interference Analysis . . . 137
Uplink Analysis . . . 138
Integrated HAPS-Satellite Layout Analysis . . . 138
UAV CIO Optimisation . . . 138
Decentralised Optimisation Beyond BCOMD . . . 139

8 Appendices **141**
Appendix A - Proof of Proposition 1 . . . 143
Appendix B - Proof of Theorem 1 . . . 145

Bibliography **161**

1 Introduction

1.1 Context

In recent years, the rapid evolution of cellular communications has driven an unprecedented increase in the demand for high-speed, ubiquitous data connectivity. This rising demand has introduced increasingly stringent requirements for both widespread coverage and high-capacity network performance. To address these challenges, mobile operators have significantly expanded terrestrial macro base stations (MBSs) deployment. However, this approach has inherent limitations, as coverage cannot be guaranteed in remote or logistically challenging locations [1].

NTNs have emerged as a promising solution to bridge these connectivity gaps, enabling expanded service to underserved regions and enhancing the global communication infrastructure. NTNs utilise airborne vehicles such as unmanned aerial vehicles (UAVs), high-altitude platform station (HAPS), or satellites, which serve as MBSs or relay nodes to enable connectivity for UEs across the network. Their primary advantage lies in their ability to deliver wide-area coverage, especially in regions where terrestrial MBSs deployment is either prohibitively expensive or logistically unfeasible. As such, through collaboration with mobile operators, the objective is to create an integrated TN-NTN capable of delivering seamless, high-capacity communication services [2], while also ensuring efficient support for UEs in the future [3], [4]. While enhancing coverage is a key driver behind the integration of NTNs, this additional network layer also introduces new opportunities to improve overall network performance. By offloading traffic from congested TNs, refining resource utilisation, or supporting backhaul links, NTNs can contribute to enhanced Quality of Service (QoS). These capabilities position NTNs not only as a solution for coverage extension, but also as a valuable complement to the incumbent TN.

Nevertheless, another major challenge facing mobile networks is sustainability—particularly in terms of energy efficiency (EE). Indeed, the extensive deployment of TNs has significantly increased overall network energy consumption, a growing concern given current environmental and economic conditions. Recent studies have shown that the telecommunications sector is responsible for approximately 3 % of global energy consumption [5]. For operators, this translates into a substantial operational burden: indeed, Fig. 1.1 illustrates that energy-related costs account for 23 % of operational expenditure (OPEX), as well as for 90 % of network costs. Selling, General

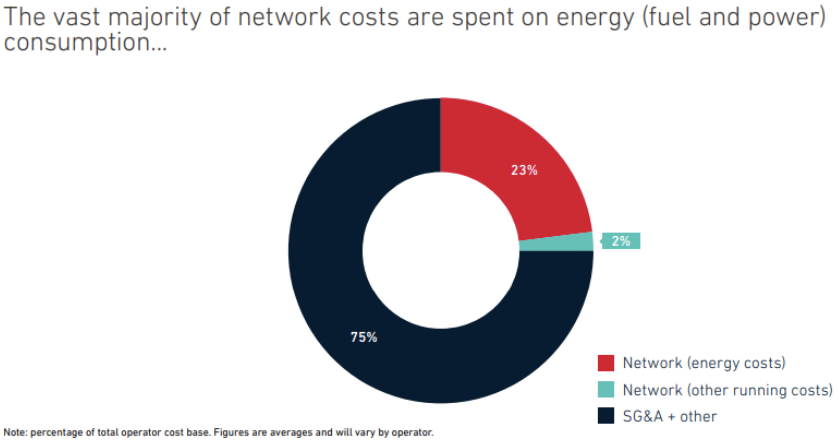

Fig. 1.1: Breakdown of Network Operational Costs [6].

and Administrative (SG&A) expenses make up for the remaining 75 %. Furthermore, Fig. 1.2 demonstrates that the radio access network (RAN) is the primary contributor to this energy usage, consuming 76 % of the total, compared to 19 % for the core network and data centers, and only 5 % for other network components. Consequently, a principal aim in the development and management of mobile networks is minimising energy consumption, while adhering to QoS standards [8].

Among the various NTN technologies, satellites currently offer the most promising solution, as other platforms may face significant economic and regulatory constraints [9], [10]. Although satellite deployment carries a notable carbon footprint [11] and incurs considerable costs, recent advances in small-satellite launch and maintenance technologies have made them increasingly cost-effective for commercial use, based on the growing adoption of real-world projects such as Starlink or Kuiper [12].

Given the decreasing cost of satellite launches, NTNs are becoming a feasible

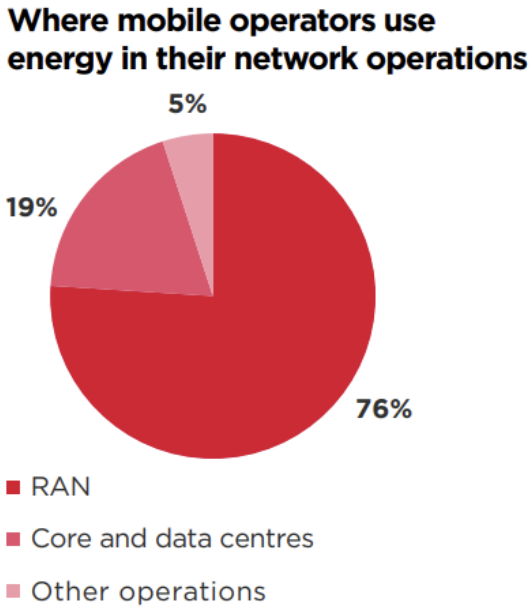

Fig. 1.2: Energy Consumption Distribution across Network Components [7].

solution not only for enhancing network coverage in underserved regions, but also for potentially reducing the overall energy consumption of mobile networks.

1.2 Motivations and Contributions

As shown in Fig. 1.3, network traffic typically follows a diurnal pattern, with minimal activity during the early morning hours (idle period), gradually increasing to peak during daytime and evening hours when user activity is at its highest, before declining again late at night. This fluctuation in traffic load naturally influences the priorities of the network operator throughout the day. During high-traffic periods, the primary objective is to maintain QoS by ensuring that the demands of all active UEs are met. This often requires effective load balancing strategies across multiple MBSs to prevent congestion and ensure fair resource allocation. In contrast, during low-traffic periods—particularly overnight or in the early morning—the network operator can shift focus toward EE. With fewer active UEs, it becomes feasible to shut down underused MBSs, thereby reducing energy consumption and mitigating the operational costs previously highlighted.

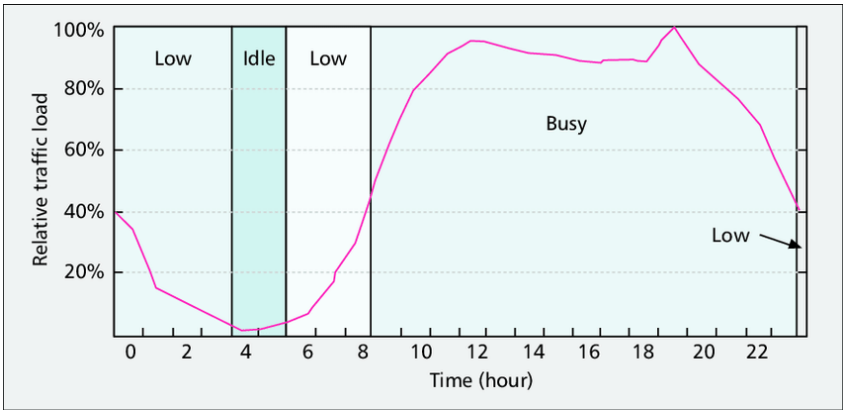

Fig. 1.3: Daily Network Traffic Load Pattern [13].

Therefore, our study aimed to develop a framework designed for integrated TN-NTN. This framework was gradually enhanced to tackle the several challenges discussed in the previous paragraph, moving from simpler to more complex modelling approaches to effectively address these challenges. It was designed to harness the advantages of NTN technology to assist the TN and mobile operators in achieving their objectives, while ensuring adaptability to varying network traffic conditions. Specifically, we showed that the non-terrestrial tier can help reduce the network energy consumption in low traffic, taking up an important role to allow the terrestrial tier to offload a portion of its UEs, enabling the shutdown of additional MBSs. Conversely, in high-traffic conditions, we demonstrated that the non-terrestrial tier assumed a supporting role, primarily serving as an umbrella to the TN to enhance coverage and facilitate the load distribution.

To that end, in our first contribution, upon recognising the limitations of traditional max reference signal received power (RSRP) association mechanisms, we developed a utility-based framework that optimised UE association through a pricing strategy. This framework also controlled the transmission power of terrestrial MBSs, as well as the allocation of bandwidth between terrestrial and non-terrestrial tiers during high traffic conditions. It effectively distributed the load, thereby improving the network sum log-throughput (SLT) and demonstrated the advantages of low-earth orbit (LEO) satellites by significantly reducing coverage gaps. Additionally, by examining scenarios where both tiers share available bandwidth, we highlighted the compromise between minimising coverage gaps and maximising network SLT.

Building on this foundation, we coined BLASTER, our second contribution. BLASTER is an innovative radio resource management (RRM) algorithm for integrated TN-NTN, designed to dynamically adjust the role of the satellites throughout the day. Similarly to the first contribution, BLASTER controlled the UE association and the split of the bandwidth of both terrestrial and non-terrestrial tiers. On top of that, it managed the shutdown of terrestrial MBS. Essentially, by optimising an astutely chosen utility function using the block coordinate gradient ascent (BCGA) algorithm, we struck the optimal balance between reducing energy consumption and enhancing network SLT depending on the traffic load. This algorithm effectively showcased the dynamic capabilities that the satellites can play over an entire day, demonstrating substantial energy savings and enhanced throughput, while maintaining service continuity.

Our third and last contribution stemmed from acknowledging the need for scalable and distributed solutions. We developed a comprehensive online learning framework leveraging the bandit-feedback constrained online mirror descent (BCOMD) algorithm. This framework facilitated the dynamic optimisation of key network parameters—namely UE association, bandwidth allocation, and terrestrial MBS shutdown decisions—and enabled fully distributed control over these processes, removing the need for a centralised entity as required in earlier versions of the framework.
Shifting to a stochastic traffic model, in which each UE had a variable data-rate demand to satisfy, we demonstrated once again the ability of the satellite tier to adjust to fluctuating traffic conditions. Indeed, we showed that we could reduce energy consumption in low-traffic, and improve the traffic load distribution in high traffic, while ensuring that we satisfied the specific data-rate requirements of each UEs.

1.3 Thesis Outline

The remaining chapters of this thesis are organised as follows:

Chapter 2 presents a general background on NTNs, introducing key technologies such as UAVs, HAPSs and satellites. We also compare the inherent advantages and shortcomings of each technology, and explain our motivation

to focus on LEO satellites in our study. Furthermore, it presents a comprehensive review of the previous contributions that have been made relating to the large-scale optimisation of integrated TN-NTN, covering areas such as load balancing, resource allocation, interference management. Finally, we give an overview of standardisation efforts, highlighting the progressive integration of NTN by the 3rd Generation Partnership Project (3GPP).

Chapter 3 describes the system model used throughout the thesis, including a detailed channel model for both terrestrial and non-terrestrial links. We also present how we model the signal-to-interference-plus-noise ratio (SINR), the data-rate as well as the energy consumption for a MBS.

Chapter 4 introduces our first contribution, an utility-based optimisation framework tailored for high traffic conditions in integrated TN-NTNs. This framework addresses the limitations of conventional RSRP-based association by introducing a pricing-based mechanism to control UE association as well as the transmit power of terrestrial MBSs. In addition, it optimises the allocation of the available bandwidth between the terrestrial and non-terrestrial tiers. The framework demonstrates its effectiveness in distributing network load more evenly, reducing coverage gaps, and improving the SLT, particularly by leveraging the presence of LEO satellites. Simulation results highlight the potential of joint utility-based association and bandwidth splitting in managing load during peak traffic periods, while quantifying the trade-offs between throughput maximisation and coverage guarantees.
The contents of this chapter have been published in the following venues:

- **2023 IEEE International Conference on Communications Workshops (ICC Workshops)**: *H. Alam, A. De Domenico, D. López-Pérez and F. Kaltenberger, "Throughput and Coverage Trade-Off in Integrated Terrestrial and Non-Terrestrial Networks: An Optimization Framework," 2023, pp. 1553-1558, Rome, Italy*

Chapter 5 builds upon the first contribution and presents BLASTER, a traffic-aware optimisation algorithm designed to adapt network operations throughout the day. Unlike the earlier framework, BLASTER introduces an additional layer of control by enabling dynamic shutdown of underutilised terrestrial MBSs during low-traffic hours to reduce network energy consumption. It jointly optimises UE association, bandwidth allocation, and MBS activation

using BCGA to maximise a utility function that balances SLT and energy consumption. BLASTER underlines the capability of LEO satellites to flexibly support the TN in different traffic regimes, and demonstrates significant improvements in both network throughput and energy savings compared to heuristic and baseline schemes.
The contents presented in this thesis have been published or submitted in the following venues:

- Published in **2024 IEEE 35th International Symposium on Personal, Indoor and Mobile Radio Communications (PIMRC)**: *H. Alam, A. De Domenico, F. Kaltenberger and D. López-Pérez, "On the Role of Non-Terrestrial Networks for Boosting Terrestrial Network Performance in Dynamic Traffic Scenarios," 2024, pp. 1-7, Valencia, Spain*.

- Published in **Elsevier Academic Press 2026**: *M. Schellmann, M.A Jamshed, G. Karetsos, H. Alam, A. De Domenico, F.R. Davoli, S. Adhatarao, Y. Chen and A. Kaushik, "**Non-Terrestrial Networks**, Chapter 12: NTN standardization in 5G NR and the path beyond," 2026, pp. 285-312, ISBN: 9780443265266.*

- Submitted to **IEEE Transactions on Vehicular Technology**: *H. Alam, A. De Domenico, D. López-Pérez and F. Kaltenberger, "Optimizing Integrated Terrestrial and Non-Terrestrial Networks Performance with Traffic-Aware Resource Management*".

Chapter 6 addresses the need for a scalable and decentralised solution by introducing an online learning framework based on the BCOMD algorithm. This framework enables fully distributed control over UE association, bandwidth allocation, and terrestrial MBS shutdown decisions, removing the need for a centralised entity as required in earlier frameworks. It emulates the behaviour of BLASTER in a distributed setting and dynamically adapts to traffic variations while respecting minimal data-rate constraints. Through extensive simulations, we demonstrated that BCOMD-based control can achieve performance levels comparable to comparable oracle benchmarks, thus validating the effectiveness of online and decentralised optimisation in integrated TN-NTN. The contents presented in this thesis have been published or are to be submitted in the following venues:

- Published in **2025 IEEE International Workshop on Signal Processing and Artificial Intelligence for Wireless Communications (SPAWC)**: *H. Alam, A. De Domenico, T. Si Salem and F. Kaltenberger, "A Multi-Armed Bandit Framework for Online Optimization in Green Integrated Terrestrial and Non-Terrestrial Networks," 2025, pp. 1-5, Surrey, UK*.
- To be Submitted to **IEEE Transactions on Wireless Communications**: *H. Alam, A. De Domenico, T. Si Salem and F. Kaltenberger, "BCOMD-NETOP: an Online Optimisation Framework for Green Integrated Terrestrial and Non-Terrestrial Networks*".

Chapter 7 concludes the thesis by summarising the key contributions and findings, while outlining several future research directions to build upon the work established in this thesis.

2

Integrated TN-NTNs: Technologies, Challenges, and State-of-the-Art

Before exploring the optimisation of integrated TN-NTN systems, it is essential to first establish a clear understanding of what constitutes an NTN. To this end, we begin by examining the architectural vision put forward by the research community for integrated TN-NTN systems, along with a detailed overview of the different enabling non-terrestrial technologies, including UAVs, HAPSs, and satellites—each with its respective strengths and limitations. We then review the progressive standardisation efforts carried out by the 3GPP across multiple releases, outlining the key milestones that have gradually enabled the seamless integration of NTNs into the 5G new radio (NR) framework. Finally, we present a comprehensive survey of the state-of-the-art research on large-scale optimisation techniques for integrated TN-NTN systems—covering aspects such as load balancing, resource allocation, interference management, and mobility support—and clearly position our contributions within this broader context.

2.1 Perspectives on Integrated TN-NTN Architectures

The integration of TNs with NTNs is a key enabler of future communication systems, aiming to provide seamless, ubiquitous, and high-capacity connectivity. This hybrid three-dimensional (3D) network architecture extends

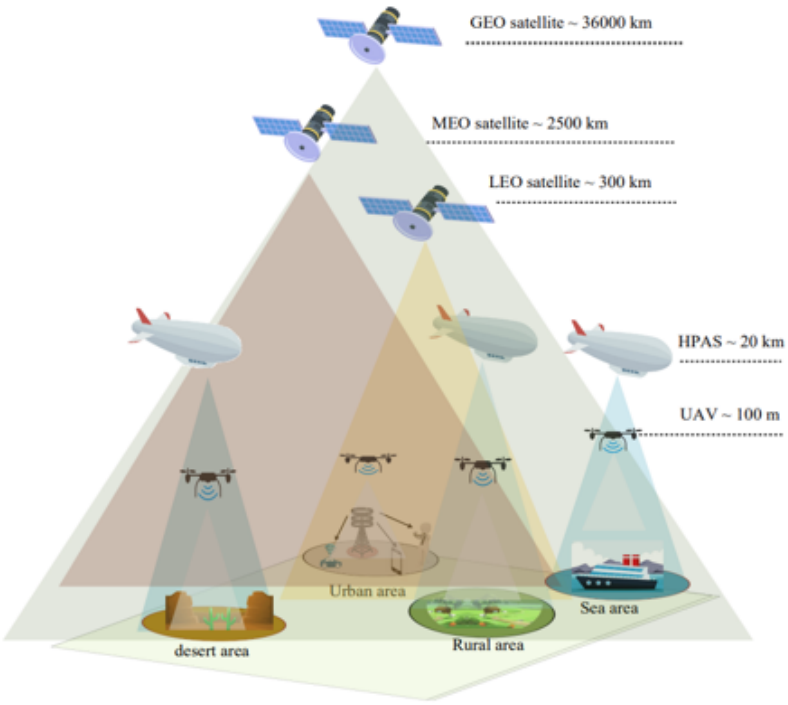

Fig. 2.1: Different NTN technologies available [14].

beyond conventional terrestrial MBSs to include a diverse set of airborne and spaceborne platforms such as UAVs, HAPSs, and satellites, as depicted in Fig. 2.1.

A typical integrated TN-NTN architecture consists of multiple hierarchical layers. Terrestrial MBSs—operating across sub-6 GHz and millimeter-wave (mmWave) bands—serve UEs with different densities and orientations, including uptilted cells for aerial users. The non-terrestrial tier complements the terrestrial tier nicely by operating at various altitudes and dynamically extending network coverage beyond traditional ground infrastructure. These non-terrestrial platforms establish wide-area connectivity through service links with UEs and feeder links to the core network, ensuring seamless integration with terrestrial components, as illustrated in Fig. 2.2.
Their mobility and altitude enable adaptive coverage, making them particularly effective in remote, underserved, or high-mobility environments [2]. Additionally, this non-terrestrial tier enhances network resilience by providing redundant communication paths and improving service continuity in case of TN failures or congestion.

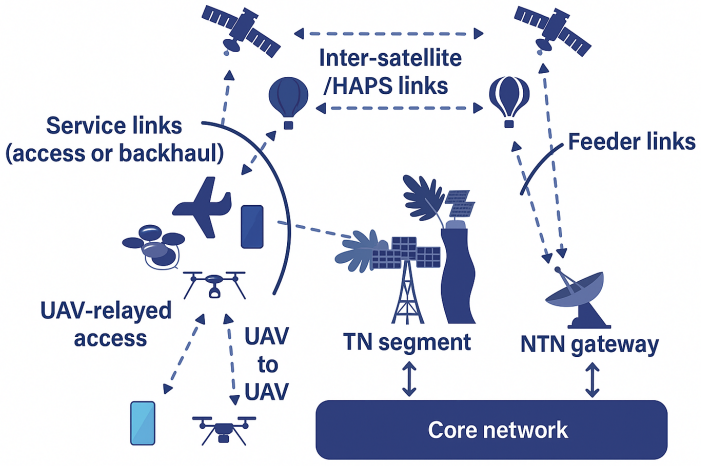

Fig. 2.2: Integrated TN-NTN architecture (Inspired from [3]).

2.2 Emerging Technologies for NTN

Now that we have presented the global architecture of an integrated TN-NTN, we will go through the different technologies that will play a major role in NTNs for the foreseeable future, and we will outline their respective strengths and limitations.

2.2.1 UAVs

UAVs, commonly known as drones, are low-altitude aerial platforms typically operating at altitudes between 0 and 4 km [15]. They are characterised by their mobility, and ability to hover or move in three-dimensional space. In the context of wireless communications, UAVs can serve as flying base stations (BSs), relays, or access points, providing on-demand connectivity and coverage, especially in dense urban [16] or hard-to-reach areas [17]. 6G networks are envisioned to natively support autonomous vehicles and drone-based communication systems, an emerging field broadly referred to as UAV communication systems (UAVCOM). As shown in Fig. 2.1, UAVs form the lowest altitude layer in the integrated TN-NTN architecture, operating at a range between 0 and 4 km [15].

Key Advantages

UAVs play a crucial role in enhancing wireless networks by providing high-speed backhaul connectivity [18]. Their ability to operate at flexible altitudes and adapt dynamically makes them ideal for on-demand network expansion in remote or congested areas [19]. Integrated with cell-free massive multiple-input multiple-output (MIMO) systems, UAVs can also improve spectral efficiency and enable low-latency communication [20]. Furthermore, their synergy with HAPSs and satellites facilitates continuous information broadcasting and enhanced data processing, surpassing the capabilities of standalone deployments [19].

Artificial intelligence (AI) and machine learning (ML) can further optimise UAV performance by dynamically adjusting flight paths, reconfiguring network topology, and improving communication reliability [20]. Additionally, UAVs can operate for extended periods by leveraging wireless power transfer and renewable energy sources such as solar power. Their versatility extends to emergency services and disaster management, enabling rapid response, real-time situational awareness, and communication restoration [21]. They also have the ability to improve security and surveillance, supporting law enforcement, border monitoring, and infrastructure protection. Furthermore, UAVs contribute to mobile edge computing, improving computational efficiency and reducing latency [22], [23]. These capabilities position UAVs as a major driver of future network deployment, offering adaptive, resilient, and high-performance connectivity across diverse applications.

Although the strengths of UAVs cannot be understated, some technical hurdles remain before we can extract the maximum potential from this technology.

Related challenges

One critical challenge that the UAVs face is energy consumption, as they require substantial power to support their mobility and maintain long-duration flights [19]. Efficient power management strategies and the integration of wireless power transfer or renewable energy sources are essential to prolong UAV operation.

In addition, accurate channel modelling and fast channel estimation are necessary to improve UAV communication efficiency, particularly in high-mobility scenarios. Furthermore, interference management is a significant issue, particularly in line-of-sight (LoS) dominated scenarios where UAVs operate at high altitudes [24]. Interference mitigation strategies, such as adaptive beamforming and spectrum-sharing techniques, are essential to maintaining communication reliability. More advanced techniques—such as uptilted antenna configurations [25], [26], massive MIMO systems [27], or cell-free network architectures [28]—offer improved performance but may be more expensive in the short term, as they require substantial network upgrades. Addressing these challenges will be key to fully unlocking the potential of UAVs.

2.2.2 HAPS

HAPS are quasi-stationary aerial platforms, such as airships or balloons, that operate in the stratosphere at altitudes ranging from 15 to 25 km above sea level. HAPS provide wide-area coverage while maintaining relative stability. These platforms effectively act as airborne repeaters, enabling broadcast and multicast wireless broadband services while extending wireless connectivity and coverage to underserved areas [29], [30]. Building upon the advantages and limitations of UAVs, HAPS emerge as a promising alternative for long-endurance aerial communication [31].

Key Advantages

HAPS-based networks are also being extensively studied since they offer several advantages, mainly operational simplicity, ease of implementation due to minimal infrastructure requirements, cost-effective deployment and launch, efficient spectrum utilisation and extensive geographical coverage [29]. In terms of flight duration and coverage, HAPS outperform UAV systems [30].

Compared to satellites, HAPS exhibit significantly lower propagation delays due to their relative proximity to the Earth. Their ability to be deployed on

demand allows them to provide rapid and continuous wireless connectivity across different regions, making them particularly useful for delay-sensitive Internet of Things (IoT) applications in future networks. Additionally, HAPS can function as an intermediate communication layer between satellites and terrestrial receivers, enhancing communication services at a regional level [15]. Indeed, the HAPS communication layer can be leveraged to perform local signal processing, supplement terrestrial and satellite communication systems, support multimedia broadcasting and multicasting, and improve link budget efficiency. Furthermore, HAPS can accommodate high-density terrestrial cells during peak demand periods and facilitate high-throughput backhaul links.

However, HAPSs still have several limitations that need to be dealt with before this technology is adopted.

Related challenges

A primary concern for HAPS is their high susceptibility to adverse weather conditions, including high-speed winds, rain and snow attenuation, temperature fluctuations, and fog. To ensure their stability and functionality in varying atmospheric conditions, designing robust platform and adaptive control mechanisms is essential.

Another significant challenge is interference, which can degrade link-level performance and hinder communication efficiency in HAPS-based networks. Effective interference mitigation strategies are crucial to maintaining reliable connectivity. Additionally, seamless integration with existing terrestrial and satellite networks is required to support high-speed backhaul and fronthaul links, demanding further research in this area.

Moreover, the development of accurate channel models for HAPS is necessary to predict signal propagation and optimise network performance [32]. Efficient signal processing techniques, resource allocation strategies, scheduling algorithms, modulation and coding schemes, and handover mechanisms must also be refined to enhance system reliability and efficiency [30]. Also,

large-scale MIMO systems and mmWave frequencies present promising opportunities for HAPS-based communication, making them important topics for future research and development.

Lastly, recent techno-economic studies [9], [10] have highlighted the technological, regulatory and economic constraints the HAPS suffer from, leaving some room for improvement in that regard.

2.2.3 Satellites

Satellites are spaceborne communication nodes that operate at various altitudes, typically partitioned in two categories: geostationary orbit (GSO) satellites and non-GSO satellites.
GSO satellites, commonly known as geostationary orbit (GEO) satellites, orbit on the equatorial plane of the Earth, at an altitude of approximately $35\,800$ km. Conversely, non-GSO satellites are composed of medium-earth orbit (MEO) and LEO satellites, which operate at altitudes ranging from $2\,000$ to $35\,000$ km for MEO and 200 km to $2\,000$ km for LEO, respectively. Note that non-GSO must be operated within a constellation to ensure continuous service coverage.
Satellite communication is expected to play a pivotal role in future 6G networks, enabling broadband connectivity, high-capacity airborne platforms, seamless global coverage, and high-speed backbone links. A key objective of 6G is the seamless integration of satellite platforms with TNs to enhance connectivity and system efficiency. In this framework, airborne communication systems and terrestrial MBSs will rely on satellite links to provide backhaul support and expand coverage across wide geographical areas [33].

Key Advantages

Due to their larger altitude of orbit, GEO satellites offer extensive geographical coverage. Also, since they maintain a fixed position relatively to the Earth, they are constantly visible to terrestrial terminals. In contrast, LEO and MEO satellites provide a higher signal-to-noise ratio (SNR) and lower transmission latency, owing to their closer proximity to the Earth. Notably, LEO satellite

systems have gained significant interest for broadband applications in recent years. Since LEO satellites operate at much lower altitudes compared to MEO and GEO satellites, they can minimise path loss, latency, and enhance signal reception, thereby enabling higher data rates [34], [35]. This proximity to Earth also leads to reduced energy needs for launching and lower power usage for transmitting signals to and from the satellite [36].

LEO satellite networks are particularly valuable for rural and remote areas, where they can provide expanded coverage and increased capacity. Additionally, LEO satellites can be integrated with HAPS and UAV-based communication systems to further enhance connectivity. The intelligent interconnection between satellite and UAV networks is expected to play a crucial role in future 6G networks, ensuring seamless and wide-area coverage [37], [38].

Nevertheless, satellites still face several challenges that must be addressed to ensure their seamless integration and widespread adoption.

Related challenges

Although the GEO satellite has proven to be useful in some scenarios, its significant orbit altitude causes a substantial signal propagation delay as well as notable attenuation. Due to their non-stationarity, key issues for LEO and MEO satellites include Doppler variation and Doppler shift, which can impact synchronisation, signal detection, as well as a higher bit error rate (BER) [34]. These challenges can affect communication reliability, signal processing, and network efficiency, necessitating advanced mitigation strategies.

As detailed previously, multiple satellite stations must be deployed to provide seamless global coverage, which introduces synchronisation complexities as satellites remain in constant motion [34], [35]. Addressing these issues requires the development of accurate air-to-ground channel models, trajectory optimisation techniques, and efficient resource allocation mechanisms for satellite communications [39].
Another critical issue is interference management between terrestrial and satellite platforms, which can degrade link-level performance. Moreover,

efficient spectrum utilisation and resource management remain key concerns for optimising satellite network operations.

Despite these challenges, LEO satellites stand out as a particularly promising solution. Their relative proximity to the Earth ensures stronger signal strength, lower latency, and the ability to cover large areas — with a beam diameter of approximately 50 km [40]. Moreover, recent studies have highlighted the cost-effectiveness of LEO satellites compared to other technologies.

In light of these advantages, we focus our research on LEO satellite systems. The following subsections present key architectural features of LEO satellites, including payload types and beam coverage strategies, which are essential to understanding their role in next-generation networks.

Payload Type

In the context of NTNs, the payload type defines the technological and functional characteristics of the payload integrated into the satellite. This payload facilitates the transmission, reception, and, in some cases, processing of communication signals within the NTN framework. NTN payloads are generally categorised into two main types: transparent (also known as "bent-pipe") and regenerative, whose differences are portrayed in Fig. 2.3.

Transparent A transparent payload functions as an analog radio frequency (RF) repeater. Unlike regenerative payloads, it lacks onboard signal processing capabilities. Instead, it receives the uplink (UL) RF signal, shifts its frequency, filters, amplifies, and retransmits it via the downlink (DL). This design is cost-effective and easier to implement, as it offloads complex processing tasks to ground-based systems. However, its functionality is restricted to signal relay, without the ability to enhance or manage the transmitted data.

Regenerative A regenerative payload integrates onboard processing capabilities into the satellite, extending its functionality beyond basic RF operations such as filtering, frequency conversion, and amplification. It can perform advanced tasks including demodulation, decoding, switching, routing, encoding, and modulation. Essentially, this type of payload

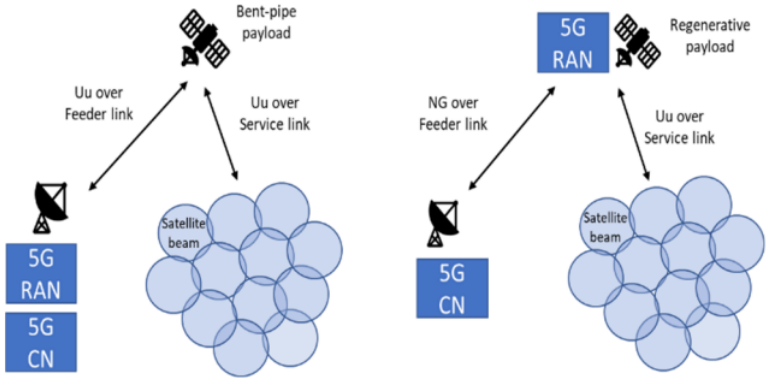

Fig. 2.3: Bent-pipe and regenerative architectures [41].

functions similarly to a BS, allowing it to manage signals autonomously. By reducing reliance on ground infrastructure, regenerative payloads enhance operational efficiency, optimise bandwidth usage, and enable more intelligent data routing.

Beam Coverage Type

There are two types of beam coverage patterns that have been proposed for the LEO satellites: Earth-moving or Earth-fixed beams, as depicted in Fig. 2.4.

For Earth-moving beams, the beam moves in synergy with the satellite which means that the coverage area is in constant motion. This induces some complexities to maintain uninterrupted connectivity as this necessitates frequent cell transitions or handovers for stationary devices.

Conversely, in the case of Earth-fixed beams, the satellites use beam-pointing mechanisms (mechanical or electronic steering feature) to compensate for their mobility and cover a given fixed region regardless of the satellite orbit position.

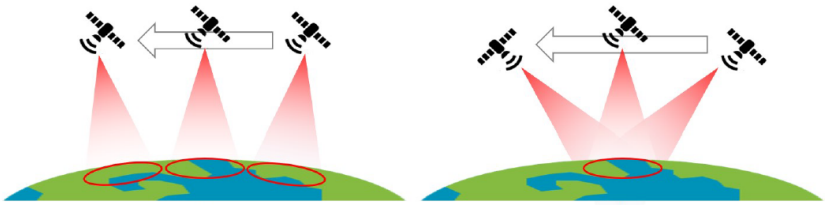

Fig. 2.4: Earth-moving (left) and Earth-fixed (right) moving beams [42].

2.3 3GPP NR Standardisation Outline

The standardisation of NTNs by the 3GPP has evolved progressively across the last Releases, each providing specific enhancements to enable seamless satellite integration into future cellular networks. In the following section, we outline the key developments that have underpinned the technical feasibility of NTNs.

2.3.1 Release 14 - Preliminary Phase

Initial considerations for the integration of NTNs began as early as Release 14. The motivation behind these early efforts stemmed from several practical and strategic factors. One of the primary drivers was the need to extend coverage to remote or underserved regions lacking reliable terrestrial cellular infrastructure. In addition, certain services—particularly multicast and broadcast transmissions—could be delivered more efficiently via satellite links. NTNs were also envisioned as a resilient fallback option in disaster scenarios, where terrestrial infrastructure may be compromised or completely unavailable. Beyond these operational benefits, the standardisation of a unified radio interface for both terrestrial and non-terrestrial components promised cost efficiencies by enabling seamless interoperability and reducing system complexity. These foundational motivations set the stage for subsequent technical developments in later 3GPP releases.

2.3.2 Release 15 (2016 - 2018)

Release 15 marked the first effort to standardise the normative requirements for 5G NR, with an initial focus exclusively on TNs. Stage 1 of TS 22.261 [43] outlined a requirement for 5G to support multiple access technologies, emphasising the need for seamless mobility across supported access networks. However, due to time constraints, satellite support was not included in the standardisation efforts for Release 15. To address this limitation, TSG RAN initiated a study item (SI) titled "Study on NR to Support NTN". This study focused on several key areas, including the identification of NTN use cases for enhanced mobile broadband (eMBB) and massive machine type communication (mMTC) services, the adaptation of the 3GPP channel model from Release 14 to accommodate the unique characteristics of NTNs, and the detailed examination of deployment scenarios. The study also analysed the necessary modifications required to enable satellite and HAPS operations within the NR framework. The outcomes of this investigation were transcribed in TR 38.811 [44].

In the context of eMBB, NTN use cases primarily focused on delivering broadband connectivity to cells or relay nodes in underserved regions, often in combination with the TN. These use cases also included establishing broadband links between the core network and remote or isolated cells. Furthermore, this study showed that NTNs enabled broadband connectivity between the core network and cells located on moving platforms, supporting continuous service in dynamic environments. For mMTC, NTN has been designed to enable global connectivity for IoT devices by facilitating direct communication between these devices and the NTN. Finally, Release 15 coined the terms of the two primary architectures for NTNs: regenerative and transparent satellites, as described in Sect. 2.2.3.

2.3.3 Release 16 (2018-2020)

In Release 16, two different working groups from the 3GPP initiated a SI related to NTNs.

The SA1-led SI titled "Study on using satellite access in 5G" examined 12

specific use cases for integrating satellite access into NR, with findings documented in TR 22.822 [45]. The study evaluated the conditions, service impacts, interactions with existing features, and potential Stage 1 requirements. These included aspects such as TN-NTN roaming, satellite-based broadcast/multicast, IoT connectivity, temporary satellite use, routing optimisation, transborder continuity, global overlays, indirect satellite access, fixed and mobile backhaul, 5G-to-premises connectivity, and offshore service center links.
The RAN3-led SI focused on developing solutions to enable NR support for NTN, addressing service continuity and multi-connectivity scenarios between TN and NTN, or between two NTN systems in parallel. This work, documented in TR 38.821 [40], built upon the key impacts identified in Release 15 by analysing their implications for RAN protocols and architecture and exploring initial solution proposals. The study emphasised satellite access through transparent GEO and LEO networks, treating HAPS as a special NTN case due to its relatively low Doppler and variation rates. Usage scenarios covered both pedestrian UEs and those in high-mobility environments such as high-speed trains and aircraft. Reference scenarios included GEO and LEO satellites with steerable and moving beams (see Fig. 2.4), using either transparent or regenerative payloads. RAN3 recommended that normative work prioritise GEO satellites with transparent payloads and LEO satellites with either transparent or regenerative payloads. The outcomes of this and related SIs provided concrete recommendations to guide subsequent normative standardisation efforts.

2.3.4 Release 17 (2020 - 2022)

Release 17 marked the first 3GPP release to introduce normative support for NTN, encompassing both 5G NR and long term evolution (LTE)-based technologies such as Narrowband-IoT and enhanced MTC. The first work items (WIs) for NR NTN were approved by the end of 2019, building on prior study results from Release 16. In WI "5GSAT", working group SA1 formalised Stage 1 requirements for satellite integration, later incorporated into TS 22.261 [43]. Parallel efforts in SA2 focused on architectural integration, producing key specifications including TS 23.501, TS 23.502 and

TS 23.503 [46]–[48], which outlined the system architecture, operational procedures, and policy control framework for NTN-enabled 5G.
The RAN-led WIs aimed to adapt core aspects of NR to account for satellite-specific characteristics such as large round-trip delays and the transparent satellite architecture. To address the UL synchronisation challenges posed by large satellite-induced delays, the 3GPP introduced a Global Navigation Satellite Systems (GNSS)-based timing advance (TA) compensation, where UEs would use their GNSS position along with broadcast ephemeris and common TA parameters to pre-compensate transmission timing. While effective for many NTN use cases, this method introduces practical limitations for devices without GNSS support.
Furthermore, to mitigate hybrid automatic repeat request (HARQ) stalling over long-delay links (especially with GEO satellites), HARQ feedback can be disabled in favour of radio link control (RLC)-level automatic repeat request (ARQ), or the number of HARQ processes can be increased to 32. For mobility, the network provides satellite ephemeris of serving and neighbouring cells within the handover command. New Conditional Handover (CHO) mechanisms were introduced in RRC_CONNECTED mode, including time-based and location-based triggers, enabling the UE to execute handover based on satellite transitions or proximity thresholds. Moreover, multiple SSB measurement timing configurations (SMTCs) per carrier were supported to handle significant propagation delay variations across neighboring satellites—critical for reliable reception of synchronisation signal blocks (SSBs).
For RF and co-existence, the requirements were captured in TR 38.863 [49] and standardised in TS 38.101-5 [50] and TS 38.108 [51]. These specifications ensure NTN compatibility in FR1, while accounting for adjacent and overlapping band coexistence. For instance, NTN bands n255 (L-band) and n256 (S-band) overlap or border terrestrial NR bands (e.g., n1, n34, n65), necessitating regional deployment constraints or interference mitigation to meet coexistence requirements.

2.3.5 Release 18 (2022 - 2024)

Release 18 introduced several enhancements to improve the practical deployment of NR NTN systems. UL coverage was optimised to support commercial

smartphones with limited antenna gain (-5.5 dBi) and polarisation loss, improving initial access performance. The frequency support was also expanded: in addition to the S-band, LS-band n254 was added, and Ka-band operation in FR2 was standardised for both GSO and non-GSO scenarios, covering DL frequencies from 17.3-20.2 GHz and UL from 27.5-30.0 GHz. The maximum supported bandwidth for NR NTN in FR1 was extended to 30 MHz and formalised in `TS 38.101-5 (Rel.18)` [52] and `TS 38.108 (Rel.18)` [53].
To address core network (CN) selection in large NTN cells spanning multiple national borders, Release 18 introduced network-verified UE location using round trip time (RTT)-based positioning. This mechanism allows the CN to verify UE-reported positions and assign the appropriate CN, ensuring compliance with regulatory requirements. It assumes a single satellite in view to simplify architecture and ensure location fidelity.
Mobility management was also refined in Release 18: For TN-NTN cell reselection, NTNs could broadcast TN coverage information, enabling UEs in `RRC_IDLE` or `RRC_INACTIVE` states to avoid unnecessary TN measurements and conserve energy. For NTN-NTN scenarios, random access channel (RACH)-less handover was introduced, supporting beam switching within the same satellite or across different feeder links and gateways, provided timing alignment conditions are met.
Finally, Release 18 addressed support for discontinuous satellite coverage, particularly relevant during early constellation deployments. NTN coverage information can be delivered to UEs to improve power-saving strategies and prevent unnecessary access attempts when no NTN signal is available.

2.3.6 Release 19 (Ongoing)

Looking ahead, Release 19 aims to continue to advance NTN support with a focus on improving DL coverage and system performance under satellite hardware constraints. Given the limited number of simultaneously active beams a satellite can support (e.g., 16–108 beams), enhancements such as beam hopping and adaptive beam sizing are being introduced to dynamically allocate power and coverage across wide satellite footprints. These techniques aim to increase the overall coverage ratio and address performance-limiting "bottleneck" channels, which suffer from poor link budgets due to constrained

transmit power.

On the uplink, orthogonal cover codes (OCC) are introduced to improve spectral efficiency. By assigning different OCC sequences to UEs sharing the same time-frequency resources, UL multiplexing becomes feasible even under the high-repetition schemes typically required for NTN link robustness, thus helping offset associated capacity losses. Enhancements for broadcast services are also being considered. Indeed, since NTN beams can cover areas significantly larger than traditional terrestrial cells, new mechanisms are being developed to notify UEs of the specific service area within a large beam, improving the relevance and efficiency of broadcast delivery.

Architecturally, regenerative payloads with onboard 5G functions are being standardised for the first time. Unlike transparent payloads used in previous releases, these satellites may implement the full gNB stack, reducing end-to-end latency and enabling localised scheduling. While Release 19 focuses on full gNB functionality onboard, future work may explore functional splits between central and distributed units (CU/DU). This shift will improve UL and DL performance, particularly for control and data channels, and extend NTN functionality to higher-frequency bands and critical services like emergency communications. As Release 19 evolves, it is expected to unify air, space, and ground into a resilient 3D network fabric, paving the way for the NTN to play a pivotal role in the forthcoming 6G era. A timeline of the technology advancements is provided in Fig. 2.5.

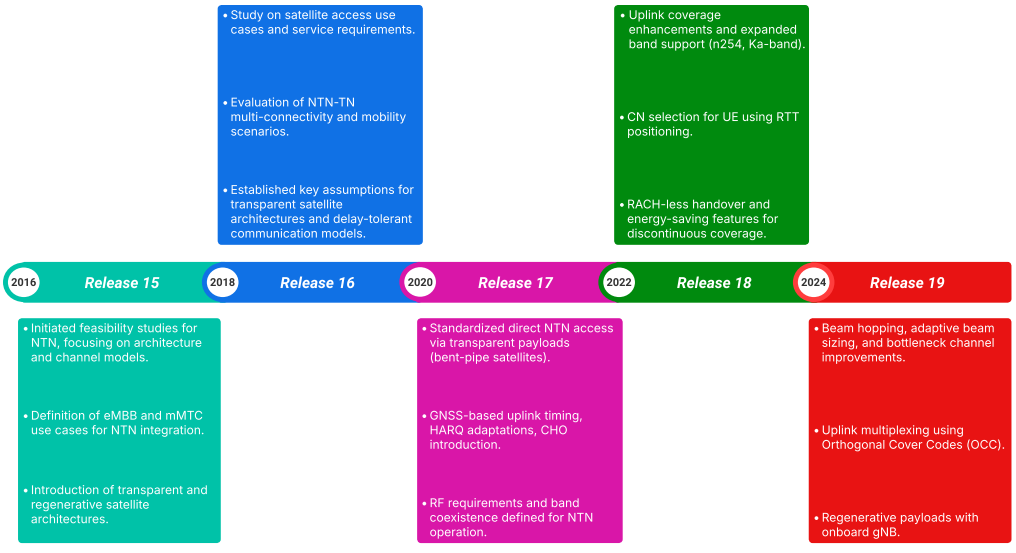

Fig. 2.5: Timeline of 3GPP Standardisation Advancements.

Although the full integration of NTNs into TNs has yet to be realised, ongoing standardisation efforts by the 3GPP signals a strong momentum in that direction. As we have seen in this section, the capabilities and interoperability of NTNs are being significantly enhanced with each new release, culminating with the introduction of regenerative satellites. These developments lay the technical foundation for NTNs to play a far more active role in supporting TNs, particularly as we move toward the 6G era. In parallel with these standardisation advances, a growing body of research has focused on optimising the performance of integrated TN-NTN systems, under the assumption that full integration will be achieved in the upcoming years. The next section presents a detailed review of this work, highlighting key strategies in load balancing, resource allocation, interference mitigation, and mobility management.

2.4 Integrated TN-NTN Large-Scale Optimisation: State-of-the-art

This section provides a comprehensive examination of several techniques that have been explored for the large-scale optimisation of integrated TN-NTNs. By critically analysing solution related to this field, this chapter lays the foundation for understanding how we can leverage NTNs in the upcoming years to evolve and accommodate the ever-increasing needs and requirements of the users in a multi-dimensional network.

2.4.1 Load Balancing in Integrated TN-NTN

In integrated TN-NTNs, load balancing is not limited in associating UEs with the MBS providing the best signal quality, as done in traditional TNs. Instead, there is the requirement to dynamically coordinate UE distribution among the different tiers of the network, while the inherent mobility of NTNs, its variability in link quality, and resource constraints necessitate efficient, adaptive and fairness-aware load distribution mechanisms.
To that end, Kwon et al. [54] and Li & Shang [55] both focus on enhancing

connectivity in integrated networks. Indeed, Kwon et al. propose a novel access-backhaul coordination strategy based on gNB cooperation in TN-NTNs. Their system enables multiple gNBs to jointly manage UE access and backhaul routing, leveraging inter-node communication to reduce bottlenecks and handover failures. This cooperative approach significantly improves end-to-end service continuity and alleviates localised congestion without requiring changes in satellite architecture. In Li & Shang, the authors investigate how multi-connectivity can mitigate handover instability and throughput degradation in heterogeneous networks. They propose a dual-connectivity framework that allows UE to maintain simultaneous links with terrestrial and satellite infrastructures. Simulation results confirm improved robustness and reduced service disruption, particularly in border areas where signal strength fluctuates frequently.

Sadovaya et al. [56] present a dynamic traffic offloading mechanism which is based on real-time link conditions. The authors integrate this with a hybrid connectivity model that supports seamless transitions between terrestrial and satellite paths, resulting in substantial improvements in packet delivery reliability and connection persistence. Khoramnejad & Hossain [57] introduce a predictive traffic engineering method using generative diffusion models. The approach enables proactive load redistribution by forecasting traffic demand patterns and carrier availability. Through optimised joint use of satellite and terrestrial carriers, the model achieves better resource utilisation and QoS, especially during traffic surges. Cao et al. [58] propose a learning-based strategy for access scheduling. Using a deep reinforcement learning (RL) framework, the system selects optimal UE associations and access points by accounting for UE priority, channel conditions, and fairness constraints. This technique outperforms traditional rule-based schedulers in throughput and delay trade-offs, particularly in environments with fluctuating link quality and intermittent satellite coverage.

Sun et al. [59] present a centralised task assignment mechanism that uses queue and beam-awareness to balance load across heterogeneous tiers. By incorporating both link capacity and service latency into its scheduling logic, the framework ensures equitable task allocation while maintaining system responsiveness. Lee et al. [60] and Shamsabadi et al. [61] try to achieve network fairness through different ways. Lee et al. address spatially uneven UE demand in satellite coverage zones. The authors formulate a scheduling

scheme that adapts resource allocation based on UE angular positions and orbital dynamics. Their fairness-driven optimisation avoids the common issue of beam-edge starvation and achieves more uniform throughput across all UEs. Shamsabadi et al. examine how different optimisation goals—such as max-throughput, proportional fairness, and max-min fairness—affect UE association decisions. Their findings show that careful selection of the objective function can significantly influence not only fairness but also overall system spectral efficiency, depending on UE density and traffic load.
Finally, Di et al. [62] focus on relieving terrestrial congestion through adaptive satellite integration. The authors propose a density-aware traffic steering mechanism that assigns users to satellites with lower load and acceptable latency. Their results indicate significant improvements in system stability and resource utilisation when compared to static offloading models.

2.4.2 Resource Allocation in Integrated TN-NTN

Resource allocation in TN-NTNs presents challenges that extend well beyond classical terrestrial models. The coordination of time-varying resources across LEO satellites and/or HAPSs with the terrestrial MBSs demands optimisation strategies that account for intermittent connectivity, tier-specific constraints and heterogeneous QoS requirements.
A prominent thread in recent literature focuses on the use of deep learning and RL to enable adaptive and predictive resource allocation. Several works in this domain target the stochastic and time-varying behavior of TN-NTNs using neural predictive models and online decision-making algorithms. Huang et al. [63] explore power and block allocation under the rate-splitting multiple access (RSMA) protocol, using real-time channel feedback to guide learning-based control policies. Similarly, Minani et al. [64] integrate long short-term memory (LSTM)-based channel forecasting with deep RL scheduling to improve UL fairness and delay bounds across satellite-connected UEs. Furthering this direction, Zhang et al. [65] introduce DetSTIN, a framework which combines deep RL with a genetic optimiser to prioritise service types and guarantee delay-aware scheduling across TN and NTN domains.

Several contributions tackle UE association, beam scheduling, and spectral efficiency in integrated TN-NTN through algorithmic and data-driven ap-

proaches. Namely, Peng et al. [66] propose an analog-digital hybrid model that leverages spatial sparsity to improve link quality and avoid beam collisions. Complementing this, Zhang et al. [67] formulate a convex-concave optimisation problem to minimise UE outage under joint beam steering and power allocation constraints. Deng et al. [68] take a group-based approach by clustering UEs with similar channel characteristics, applying joint precoding and allocation to enhance intra-beam spectral efficiency. In the domain of adaptive UE-to-beam mapping, Mashiko et al. [69] offer a model for adjusting beam assignments based on UE load and mobility, further improving link utilisation under dynamic topologies.

Effective resource allocation across satellite, HAPS, and ground domains demands intelligent cross-tier coordination. Therefore, several studies have proposed mechanisms to dynamically manage backhaul routing, gateway selection, and UE association across layers. Jia et al. [70] cast the backhaul assignment problem as a matching game, enabling stable, utility-maximising associations between aerial access nodes and satellites. In Dahrouj et al. [71], a neural network scheduler adaptively assigns UEs to either TN, HAPS or LEO tier based on predicted load patterns and mobility states. Similarly, Fu et al. [72] integrate spectrum and computational scheduling under predictive control to enable global fairness, while [73] further enhance these ideas by modelling multi-operator environments and using fairness-aware admission control for inter-domain resource governance.
Emerging use cases also necessitate coexistence with primary services and dynamic spectrum reuse. Liu et al. [74] examine how non-orthogonal multiple access (NOMA) enables spectrum reuse in cognitive satellite systems. The authors propose joint subcarrier and power allocation for opportunistic access by terrestrial UE to satellite spectrum, while safeguarding primary NTN services.

2.4.3 Interference Management in Integrated TN-NTN

It is imperative to examine another equally critical aspect: interference management. Indeed, as integrated TN-NTNs become more adopted and dense-with coexisting terrestrial, aerial, and satellite nodes—interference becomes a fundamental barrier to reliable performance. Unlike legacy cellular

networks, integrated TN-NTNs must address not only intra-tier interference (e.g., between LEO satellites) but also cross-tier and cross-technology interference, which are often exacerbated by spatial overlaps, beam cross-links, and the use of shared spectrum bands.
To address these multifaceted challenges, recent literature proposes a diverse range of strategies, including spectrum coexistence modelling, stochastic geometry analysis, RRM, and access protocol innovations.

A number of studies focus on quantifying and modelling coexistence scenarios between terrestrial and satellite systems sharing the same frequency bands. Ayoubi et al. [75] examine interference leakage from 5G systems to satellite receivers in shared spectrum. The paper uses stochastic geometry and Monte Carlo simulations to establish coexistence thresholds and inform policy decisions. Similarly, Niloy et al. [76] provide a detail model of how terrestrial 5G deployments interfere with non-geostationary satellite services. The authors then recommend constraints on terrestrial MBS power levels and guard zones to preserve satellite link integrity. Kim et al. [77] analyse scenarios where multiple LEO satellites operate in close orbital proximity using overlapping channels. The authors find that even slight misalignment in beam pointing or orbital spacing can cause severe degradation unless precise beam scheduling and coordination mechanisms are enforced. The study realised by Niloy et al. [78] further advances this line of work by proposing adaptive interference constraints that change based on environmental and temporal context. This dynamic approach allows coexistence policies to scale with traffic patterns, improving spectrum utilisation efficiency without sacrificing service protection.

Beyond spectrum-level modelling, several contributions examine how astute RRM can proactively mitigate interference in integrated TN-NTNs. In fact, Shamsabadi et al. [79] introduce a context-aware RRM framework for HAPS and terrestrial integration. It dynamically adjusts power and time-frequency resource blocks using environmental feedback, thereby reducing interference between aerial and ground MBSs. A broader architectural perspective is presented in Rahman et al. [80]. This work proposes a joint optimisation framework that allocates traffic between TN and NTN segments while simultaneously tuning transmission parameters to minimise inter-tier interference. By integrating load distribution and interference-

aware scheduling, the system reduces cross-tier congestion and improves overall throughput. Shamsabadi et al. [81] explore the unique challenges of deploying TN-NTNs in dense urban environments. The paper highlights how beam overlaps and reflection-induced interference become more significant in cities and offers design considerations for minimising these effects through spatial isolation and altitude planning.

Some studies focus on fundamental waveform or access-layer innovations to reduce interference in integrated TN-NTNs. In Zhu et al . [82], the authors demonstrate how NOMA can enable better spectral reuse while also reducing mutual interference by exploiting power-domain multiplexing and UE clustering techniques. Torrens et al. [83] shift the focus to mmWave technology and THz-based NTN systems, where narrow beamwidths can offer interference mitigation but are susceptible to alignment loss. The study quantifies interference dynamics in cross-links and offers design recommendations for beam scheduling under high mobility.

Finally, spatial scheduling and beam pattern management are increasingly relevant for minimising interference in dense LEO constellations. Lei et al. [84] present an optimisation framework which selects beam patterns and schedules UEs based on demand density and spatial alignment. By doing so, it minimises co-beam interference and improves link fairness. Kim et al. [85] model the coexistence of satellite and TNs using stochastic geometry. It characterises interference fields and proposes spatial coordination policies, such as exclusion zones and directional filters, that help balance throughput and reliability under shared access conditions. Lastly, Zhang et al. [86] introduce cross-layer cooperation to address co-tier and cross-tier interference explicitly, improving both energy efficiency and spectral fairness via joint scheduling and interference-aware power distribution.

2.4.4 Mobility and Cell Switching in Integrated TN-NTN

Another pivotal area in the realisation of integrated TN-NTN systems is the efficient handling of mobility and cell switching. The heterogeneity in altitude, mobility profiles, and coverage footprints across terrestrial and

non-terrestrial tiers introduces unique challenges in maintaining continuous, efficient connectivity.

A foundational approach is explored in Li et al. [87], where a dual-objective optimisation model addresses energy-aware mobility management by balancing the load between satellite and terrestrial nodes through adaptive cell switching and radio access selection. The framework shows significant gains in both throughput and energy efficiency under dynamic network conditions. Meanwhile, the work done by Benzaghta et al. [4] demonstrates the importance of intelligent offloading of UAV traffic to satellite links. This reduces both the outage experienced by UAVs and UL interference to ground UEs, effectively leveraging mobility-induced diversity for improved performance. The role of learning-based schemes in dynamic mobility environments is exemplified in Benzaghta et al. [88]. The authors propose a data-driven Bayesian optimisation framework to learn optimal handover decisions with minimal signalling overhead. It proves especially effective in high-mobility contexts, adapting to spatio-temporal variations in satellite coverage.

Finally, the comprehensive system proposed in Huang et al. [89] introduces a hybrid deep RL-based algorithm that jointly manages task offloading, UAV trajectory, and cloud selection. The integration of task dependency, partial offloading, and satellite dynamics into mobility decisions reflects the growing complexity and importance of mobility-aware orchestration in TN-NTN systems.

2.4.5 Summary and Open Challenges

The integration of TN-NTNs has been extensively studied in recent years, with various works addressing the architectural, technological, and algorithmic aspects required to enable seamless global connectivity. These efforts have largely focused on the design of layered infrastructures incorporating UAVs, HAPS, and satellites, as well as the development of resource allocation and user association strategies to coordinate access across heterogeneous platforms. Collectively, this body of work has laid the foundation for the future of 6G networks. Despite these advances, several key limitations remain. One major shortcoming in the current literature is the fact that NTNs seem

to be considered merely as a coverage enhancement, failing to exploit the full potential of this technology. Indeed, as seen in Sect. 2.4.4, there is a scant amount of work examining the role that the NTNs can play in reducing the network energy consumption. Moreover, there is limited research on the ability of NTNs to enable load balancing of the TN as shown in Sect. 2.4.1. Another important gap lies in the treatment of the spectrum allocation between the terrestrial and non-terrestrial tiers. In fact, previous studies overlook the potential of dynamic bandwidth sharing both tiers, as revealed in Sect. 2.4.2. This is a critical limitation, as the ability to control how bandwidth is split between the terrestrial and non-terrestrial tiers can directly affect how the role of the NTN evolves over time. For example, satellites can be leveraged to offload traffic during peak demand periods or take a more prominent role when terrestrial MBSs are shut down to conserve energy. Therefore, managing the inter-tier bandwidth split is not just a resource allocation task—it is a central mechanism through which the network can adjust its operating mode in response to the daily traffic fluctuation depicted in Fig. 1.3.

In light of these limitations, this thesis proposes a comprehensive optimisation framework that addresses the shortcomings of existing research and unlocks the full potential of integrated TN-NTN systems. The proposed framework explicitly models and controls the bandwidth sharing between the terrestrial and non-terrestrial tiers, enabling the dynamic reallocation of spectral resources based on real-time traffic demands. It adapts continuously to the temporal variations in user demand and network load, allowing the system to prioritise either load balancing or energy efficiency depending on current conditions. This flexibility reveals the polyvalent nature of the NTNs, which can act as a high-capacity load balancer during busy hours, or as a resilient fallback layer when terrestrial infrastructure is temporarily deactivated.
Through these contributions, the thesis not only fills critical gaps in the existing literature but also demonstrates how integrated TN-NTN systems can be made more adaptive and efficient—paving the way toward truly autonomous and resilient 6G networks.

3 System Model

In this chapter, we will detail the system model that we will adopt for the remainder of the manuscript, covering different subjects related to the system model and providing a comprehensive view. As the system model naturally evolved and became more complex with time, we will present the most complete version of it and specify the exact system model relevant to each of our contributions to ensure clarity.

3.1 System Parameters and Notation

Our study focuses on the DL of a cellular network which consists of M terrestrial MBSs and N MBSs installed on a constellation of LEO regenerative satellites, making a total of L MBSs. They provide service to K UEs located in the area of study, where the MBSs are deployed in an hexagonal grid layout [90]. The area of study was exclusively a rural scenario in our initial work in Chapter 4. Afterwards, in Chapters 5 and 6, we shifted to a hybrid layout, with an area composed of both rural and urban zones, as depicted in Fig. 3.1. Deployment configurations for UEs and MBSs differ between rural and urban scenarios, with urban zones generally featuring a higher density to accommodate greater demand and infrastructure capacity. We refer to the overall network bandwidth as W, which is distributed by the mobile network operator across the ground and space-based networks. We suppose that the network operates within the S band, around 2 GHz, with ground and satellite MBSs using orthogonal, but dynamically adjustable, portions of this band.

Throughout this manuscript, we will use $\mathcal{T}$ and $\mathcal{S}$ to represent the set of terrestrial and satellite MBSs respectively. Moreover, $\mathcal{B} = \mathcal{T} \cup \mathcal{S} = \{1, \cdots, j, \cdots, L\}$ is the complete set of MBSs, and $\mathcal{U} = \{1, \cdots, i, \cdots, K\}$ defines the set of UEs. We will also designate the Hadamard product with $\odot$.

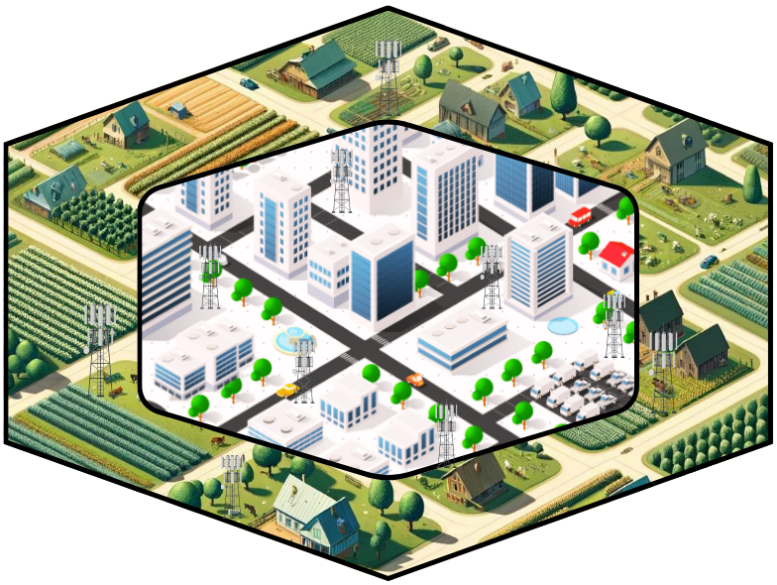

Fig. 3.1: Representation of the area of study.

3.2 Channel modelling

We now detail the channel model considered for satellite and terrestrial links, who were constructed based on the 3GPP recommendations provided in [44], [91].

3.2.1 Terrestrial Link

We adopt the height and distance notation defined in Fig. 3.2 for the remainder of this section when presenting the channel model, including path loss and LoS probability.

Line-of-sight Probability

It should be noted that the LoS condition greatly impacts the channel quality and should not be overlooked when aiming to build a realistic scenario. For UEs being served by ground MBSs, the LoS probability is calculated based on the model detailed in [91, Table 7.4.2-1].

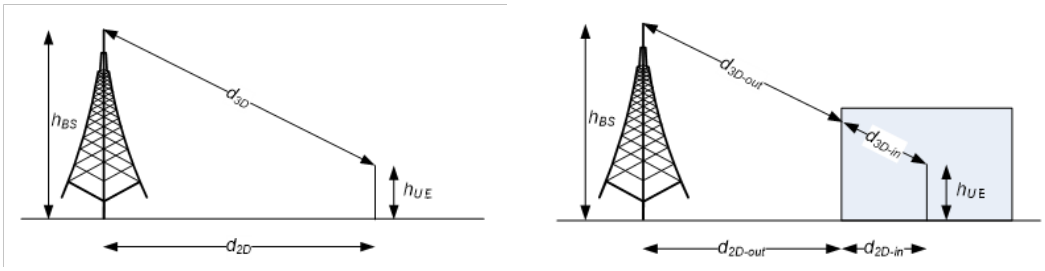

(a) Definition of $d_{2\mathrm{D}}$ and $d_{3\mathrm{D}}$ for outdoor UEs.

(b) Definition of $d_{2\mathrm{D-out}}$, $d_{2\mathrm{D-in}}$, $d_{3\mathrm{D-out}}$, and $d_{3\mathrm{D-in}}$ for indoor UEs.

Fig. 3.2: Distance and height parameter definitions for outdoor and indoor UEs [91].

For the rural scenario, the LoS probability is computed as:

$$\mathbb{P}_{\mathrm{LoS}} = \begin{cases} 1, & \text{if} \quad d_{2\mathrm{D-out}} \leq 10\,\mathrm{m} \\ \exp\left(-\frac{d_{2\mathrm{D-out}}-10}{1000}\right), & \text{else.} \end{cases} \tag{3.1}$$

For the urban scenario, the LoS probability can be derived as:

$$\mathbb{P}_{\mathrm{LoS}} = \begin{cases} 1, & \text{if} \quad d_{2\mathrm{D\text{-}out}} \leq 18\,\mathrm{m} \\ \left[\frac{18}{d_{2\mathrm{D\text{-}out}}} + \exp\left(-\frac{d_{2\mathrm{D\text{-}out}}}{63}\right)\left(1 - \frac{18}{d_{2\mathrm{D\text{-}out}}}\right)\right] \cdot \\ \left(1 + \frac{5}{4}\,\mathrm{C}'(h_{\mathrm{UE}})\left(\frac{d_{2\mathrm{D\text{-}out}}}{100}\right)^3 \exp\left(-\frac{d_{2\mathrm{D\text{-}out}}}{150}\right)\right), & \text{else.} \end{cases} \tag{3.2}$$

where $\mathrm{C}'(h_{\mathrm{UE}}) = \begin{cases} 0, & \text{if} \quad h_{\mathrm{UE}} \leq 13\,\mathrm{m} \\ \left(\frac{h_{\mathrm{UE}}-13}{10}\right)^{1.5}, & \text{else} \quad 13\,\mathrm{m} < h_{\mathrm{UE}} \leq 23\,\mathrm{m}. \end{cases}$

Large-scale channel gain

The large-scale channel gain between a ground-based MBS j and a UE i is calculated as follows:

$$\beta_{ij} = \lfloor G_{\mathrm{Tx}} + G_{\mathrm{UE}} + \mathrm{PL}_{ij}^{b} + \mathrm{SF}_{ij} + \mathrm{PL}_{ij}^{\mathrm{tw}} + \mathrm{PL}_{ij}^{\mathrm{in}} + \mathcal{N}\left(0, \sigma_p^2\right) \rceil, \tag{3.3}$$

where all components are expressed in dB, and the operator $\lfloor \cdot \rceil$ is used to convert dB values to linear. G_{Tx} and G_{UE} represent the MBS and the UE

antenna gains, respectively, PL_{ij}^{b} is the basic outdoor path loss detailed in [91, Table 7.4.1-1], and SF_{ij} is the shadow fading, which follows a normal distribution, in the dB domain, of mean 0 and variance σ_{SF}^2.
The last three components are related to the outdoor-to-indoor (O2I) building penetration loss and are developed in [91]. Indeed, $\mathrm{PL}_{ij}^{\mathrm{tw}}$ represents the loss in signal strength as it penetrates the external wall of the building, $\mathrm{PL}_{ij}^{\mathrm{in}}$ is the inside loss, which depends on the location of the UE inside the building and $\mathcal{N}\left(0, \sigma_p^2\right)$ denotes the random component of the penetration loss, with standard deviation σ_p. In order to calculate the basic path loss component PL^{b}, we need to introduce the *breakpoint* distances d_{PB} and d'_{PB}:

$$d_{\mathrm{BP}} = \frac{4h_{\mathrm{BS}}h_{\mathrm{UE}}f_c}{c} \qquad d'_{\mathrm{BP}} = \frac{2\pi h_{\mathrm{BS}}h_{\mathrm{UE}}f_c}{c}. \tag{3.4}$$

The breakpoint distances d_{BP} and d'_{BP} represent the critical distance beyond which the path loss model changes its formulation. It is computed as a function of the effective antenna heights at the MBS h_{BS} and the UE h_{UE}, the carrier frequency f_c in hertz, and the speed of light in free space $c = 3.0 \times 10^8$ m/s. This distance is essential in distinguishing between the near-field and far-field propagation behaviour.
Then, the basic path loss component PL^{b} (in LoS) in the *rural* scenario is computed as:

$$\mathrm{PL}_{\text{RMa-LoS}} = \begin{cases} \mathrm{PL}_1, & \text{if} \quad 10\,\mathrm{m} \leq d_{2D} \leq d_{\mathrm{BP}} \\ \mathrm{PL}_2, & \text{else} \quad d_{\mathrm{BP}} < d_{2D} \leq 10\,\mathrm{km} \end{cases} \tag{3.5}$$

where:

$$\begin{aligned} \mathrm{PL}_1 = {} & 20\log_{10}\left(40\pi d_{3\mathrm{D}} f_c/3\right) + \min\left(0.03h^{1.72},\, 10\right)\log_{10}(d_{3\mathrm{D}}) \\ & - \min\left(0.044h^{1.72},\, 14.77\right) + 0.002\log_{10}(h)d_{3\mathrm{D}}, \end{aligned}$$

and

$$\mathrm{PL}_2 = \mathrm{PL}_1(d_{\mathrm{BP}}) + 40\log_{10}(d_{3\mathrm{D}}/d_{\mathrm{BP}}).$$

For the non-LoS case, we compute the path loss as:

$$\mathrm{PL}_{\text{RMa-NLOS}} = \max\left(\mathrm{PL}_{\text{RMa-LOS}}, \mathrm{PL}'_{\text{RMa-NLOS}}\right), \tag{3.6}$$

for $10\text{ m} \leq d_{\text{2D}} \leq 5$ km, and where:

$$\begin{aligned}\text{PL}'_{\text{RMa-NLOS}} =& 161.04 - 7.1\log_{10}(W_s) + 7.5\log_{10}(h) \\ &- \left(24.37 - 3.7\left(\frac{h}{h_{\text{BS}}}\right)^2\right)\log_{10}(h_{\text{BS}}) \\ &+ (43.42 - 3.11\log_{10}(h_{\text{BS}}))\,(\log_{10}(d_{\text{3D}}) - 3) \\ &+ 20\log_{10}(f_c) - \left(3.2\left(\log_{10}(1.175h_{\text{UE}})\right)^2 - 4.97\right).\end{aligned} \tag{3.7, 3.8}$$

The urban scenario path loss formula for both LoS and non-LoS is as follows:

$$\text{PL}_{\text{UMa-LoS}} = \begin{cases}\text{PL}_1, & 10\,\text{m} \leq d_{\text{2D}} \leq d'_{\text{BP}} \\ \text{PL}_2, & d'_{\text{BP}} < d_{\text{2D}} \leq 5\,\text{km}\end{cases} \tag{3.9}$$

where:

$$\text{PL}_1 = 28.0 + 22\log_{10}(d_{\text{3D}}) + 20\log_{10}(f_c), \tag{3.10}$$

and

$$\text{PL}_2 = 28.0 + 40\log_{10}(d_{3D}) + 20\log_{10}(f_c) - 9\log_{10}\left((d'_{\text{BP}})^2 + (h_{\text{BS}} - h_{\text{UE}})^2\right). \tag{3.11}$$

The parameters used in the path loss model follow standardised units. All distances, including d_{2D} and d_{3D}, are expressed in meters (m), while the carrier frequency f_c is given in gigahertz (GHz). In the rural scenario, the MBS height is set to $h_{\text{BS}} = 35\,\text{m}$ and the UE height to $h_{\text{UE}} = 1.5\,\text{m}$, whereas for the urban scenario, we consider $h_{\text{BS}} = 25\,\text{m}$, and h_{UE} ranges from $1.5\,\text{m}$ to $22.5\,\text{m}$.

The average street width is taken as $W_s = 20\,\text{m}$, and the average building height as $h = 5\,\text{m}$.

Note that in the rural scenario, these parameters are required to fall within the following applicability ranges to ensure model validity: $10\,\text{m} \leq h_{\text{BS}} \leq 150\,\text{m}$, $1\,\text{m} \leq h_{\text{UE}} \leq 10\,\text{m}$, $5\,\text{m} \leq h \leq 50\,\text{m}$, and $5\,\text{m} \leq W_s \leq 50\,\text{m}$.

3.2.2 Satellite Link

Elevation angle

The elevation angle is a key parameter related to the LEO satellite position, as it greatly affects the channel quality for terrestrial UEs by influencing both the LoS probability and the path loss, as we will see in the subsequent sections. The elevation angle is the angle between the horizontal plane (the plane parallel to the surface of the Earth at the UE location) and the line of sight to the satellite, denoted as α in Fig. 3.3.

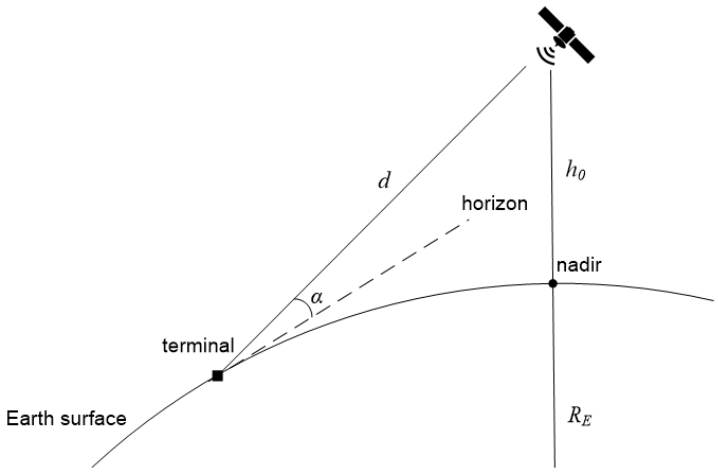

Fig. 3.3: Representation of satellite elevation angle [44].

In the scope of our work, given the cartesian coordinates of a satellite s (x_s, y_s, z_s) and a UE u (x_u, y_u, z_u), we can compute the elevation angle θ_u as:

$$\theta_u = \arcsin\left(\frac{z_s - z_u}{\sqrt{(x_s - x_u)^2 + (y_s - y_u)^2 + (z_s - z_u)^2}}\right). \tag{3.12}$$

Note that the mobility of the satellite was only considered in Chapters 5 and 6, while in Chapter 4 we made the assumption that the elevation angle was constant.

To embrace the mobility of the LEO satellites, we assessed network performance at three distinct positions (P1, P2, P3), as illustrated in Fig. 3.4:

P1) We make the first performance assessment when the satellite is located at the nadir point of the beam adjacent to our area of study, which is located at a horizontal distance of 50 kms (as well as a total distance of approximately 603 kms) from the center of the area of study, with an elevation angle (for a UE located at the center of the central beam) approximately equal to $84°$.

P2) The second assessment is made when the satellite is at the nadir point, exactly above the center of our area of study.

P3) Similarly to the first measurement, we make the assessment when the satellite is 50 kms away from the center of the area of study, at the nadir point of the next contiguous beam.

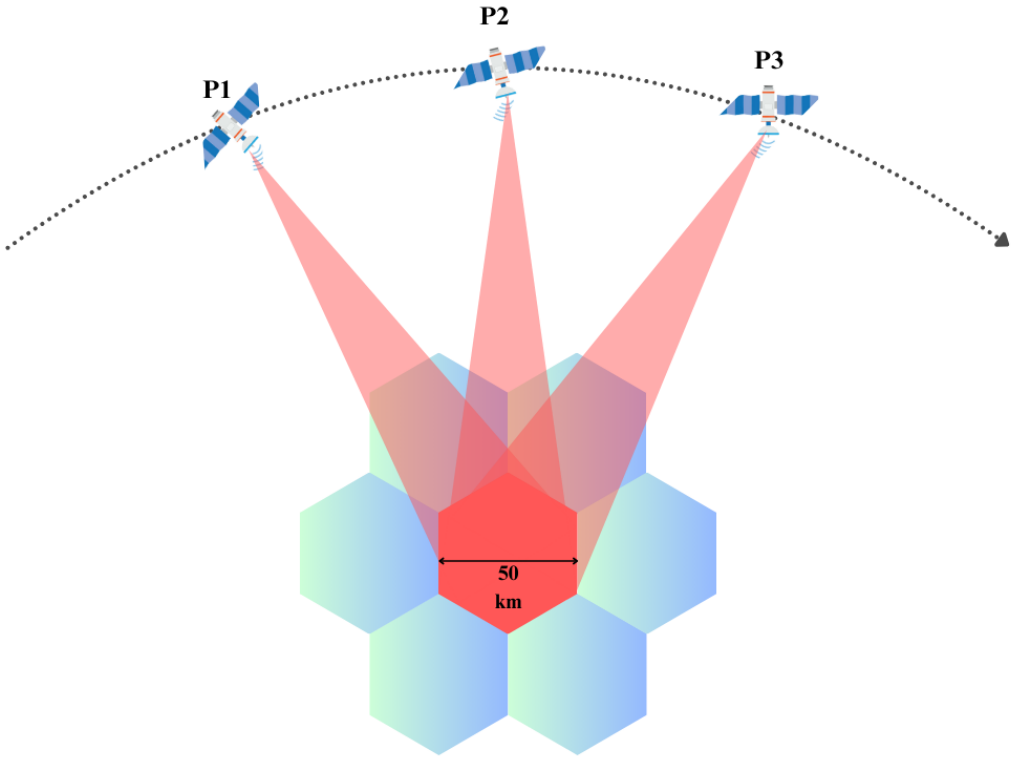

Fig. 3.4: Representation of the satellite positions considered for the area of study (in red).

Averaging the values obtained from these three assessments, we can get an overview of the satellite channel quality.

Line-of-sight Probability

The probability of LoS for UEs served by satellite MBS is determined using the model outlined in [44, Table 6.6.1-1] and reproduced in Table 3.1. Based

Tab. 3.1: Line-of-Sight Probability.

Elevation angle	Urban Scenario	Rural Scenario
10°	24.6%	78.2%
20°	38.6%	86.9%
30°	49.3%	91.9%
40°	61.3%	92.9%
50°	72.6%	93.5%
60°	80.5%	94.0%
70°	91.9%	94.9%
80°	96.8%	95.2%
90°	99.2%	99.8%

on these values, we can see that the elevation angle has a large influence on the LoS probability.

Large-scale channel gain

Similarly, if a satellite MBS j is serving a UE i, we can compute the large-scale channel gain (detailed in [44]) as:

$$\beta_{ij} = \left\lfloor G_{\mathrm{Tx}} + G_{\mathrm{UE}} + \mathrm{PL}_{ij}^{b} + \mathrm{SF}_{ij} + \mathrm{CL} + \mathrm{PL}_{ij}^{s} + \mathrm{PL}_{ij}^{e} \right\rfloor . \tag{3.13}$$

In Equation (3.13), CL accounts for clutter loss, which is the attenuation arising from obstacles such as buildings and vegetation surrounding the UE. The clutter loss and shadow fading components are provided in Table 3.2 for urban and rural scenarios respectively.
PL_{ij}^{b} represents the free-space path loss:

$$\mathrm{PL}^{b} = 32.45 + 20\log_{10}(f_c) + 20\log_{10}(d), \tag{3.14}$$

where the distance d is in meters and f_c is in GHz.
PL_{ij}^{s} captures the scintillation loss, reflecting the quick changes in signal

amplitude and phase due to ionospheric disturbances. Finally, PL_{ij}^{e} refers to the building entry loss, an attenuation that occurs for all UEs located indoors.

Tab. 3.2: Shadow fading and clutter loss for urban and rural scenarios (S-band) [44, Section 6.6.2].

Elevation Angle	Urban scenario			Rural scenario		
	LoS	NLoS		LoS	NLoS	
	σ_{SF} (dB)	σ_{SF} (dB)	CL (dB)	σ_{SF} (dB)	σ_{SF} (dB)	CL (dB)
10°	4	6	34.3	1.79	8.93	19.52
20°	4	6	30.9	1.14	9.08	18.17
30°	4	6	29.0	1.14	8.78	18.42
40°	4	6	27.7	0.92	10.25	18.28
50°	4	6	26.8	1.42	10.56	18.63
60°	4	6	26.2	1.56	10.74	17.68
70°	4	6	25.8	0.85	10.17	16.50
80°	4	6	25.5	0.72	11.52	16.30
90°	4	6	25.5	0.72	11.52	16.30

3.3 Signal-to-interference-plus-noise ratio

Considering that each UE is either associated to a terrestrial or satellite MBS, and there is no interference between the two tiers, as they are allocated different bandwidths orthogonally, we can calculate the large-scale SINR for each UE i and MBS j as:

$$\gamma_{ij} = \frac{\beta_{ij} p_j}{\sum\limits_{j' \in \mathcal{I}_j} \beta_{ij'} p_{j'} + \sigma^2}. \tag{3.15}$$

In (3.15), p_j denotes the transmit power allocated per resource element (RE) at MBS j, $\mathcal{I}_j$ indicates the set of MBSs interfering with the serving MBS j and σ^2 represents the noise power per RE.

Note that the numerator in Equation (3.15) is actually the perceived RSRP for UE i.

3.4 Data-rate

In the early stages of our work (Chapter 4 and Chapter 5, we assumed a full-buffer traffic model, where each UE continuously required data and utilised all available resources. Under this assumption, the total resources of a given BS were evenly shared among its associated UEs, leading to a simplified resource distribution model that ensured fairness but did not account for individual variations in user demand. However, for the work in Chapter 6, we considered a more realistic scenario where each UE had a specific data-rate demand, modelled as a random variable following an exponential distribution of parameter λ_{U}. This approach better reflects diverse UE requirements and introduces variability in resource allocation.

3.4.1 Full-buffer scenario

As detailed above, assuming that MBS j equally shares its total available bandwidth W_j between the k_j UEs it is serving, we are able to compute the mean throughput for UE i connected to MBS j as follows:

$$R_{ij} = \frac{W_j}{k_j} \log_2(1 + \gamma_{ij}). \tag{3.16}$$

Essentially, we multiply the bandwidth available to the UE by the spectral efficiency based on the Shannon capacity formula.

3.4.2 User-Specific scenario

In this scenario which was used exclusively in Chapter 6, we considered a physical resource block (PRB) allocation method which took into account the demanded data-rate for each UE. Thereby, the mean throughput for UE i served by MBS j is calculated as:

$$R_{ij} = B_{ij} \log_2(1 + \gamma_{ij}), \tag{3.17}$$

where B_{ij} denotes the number of PRBs assigned to UE i by the serving MBS j.

3.5 Physical Resource Block Allocation

As stated in Section 3.4, we did not take PRB allocation into account in the system model of our research in Chapters 4 and 5. However, in Chapter 6, we incorporated PRB allocation by considering the demanded data-rate, ensuring a more realistic and practical assessment of resource distribution.

With that in mind, supposing that UE i has a minimum data-rate demand of ρ_i bits/second, the number of PRBs assigned to the UE by the associated MBS j is computed as:

$$B_{ij} = \left\lceil \frac{\rho_i}{\Delta \log_2 (1 + \gamma_{ij})} \right\rceil . \tag{3.18}$$

In Equation (3.18), the denominator is the product between the spectral efficiency and Δ, which represents the total bandwidth of a single PRB in 5G NR. Finally, $\lceil \cdot \rceil$ denotes the ceiling function which rounds up the input number to the nearest integer.

Then, by denoting N_j^{PRB} the total number of PRBs available at MBS j, we can compute its load as follows:

$$\nu_j = \frac{1}{N_j^{\mathrm{PRB}}} \sum_{i \in \mathcal{U}} B_{ij}. \tag{3.19}$$

3.6 Energy Consumption model

While [92] provided one of the most widely used models for 4G MBS energy consumption, it is not well suited for 5G MBSs integrating massive MIMO technology. Consequently, we chose the more recent model proposed in [93] which accounts for massive MIMO and carrier shutdown, and thus fits better to our system design. Note that, in the context of our work, shutdown and

sleep mode are considered equivalent, as both refer to states in which a MBS significantly reduces or halts its operations to conserve energy. More generally, it only takes 3 seconds to shutdown or wake up a MBS, while the shutdown duration may range from tens of seconds to minutes or even hours [94].

The energy consumption of a MBS can be modelled as the sum of multiple components. We denote as the baseline energy consumption, the energy used by the components that are kept active in a shutdown MBS. Then, we denote as the static component, the energy consumption that occurs regardless of the level of the MBS traffic load. The static energy consumption represents the minimum power required to keep essential systems operational and maintain standby readiness. Finally, the dynamic component refers to the load-dependent energy consumption that fluctuates depending on the MBS traffic load. Typically, the dynamic component increases whenever a MBS increases its transmit power or uses additional transmission resources, e.g., more PRBs For a MBS j, this model can be formulated as:

$$Q_j(p_j) = P_0 + p_j + \psi_j ||p_j||_0, \tag{3.20}$$

where P_0 represents the baseline energy consumption, ψ_j represents the static component and p_j accounts for the dynamic consumption of the MBS. Also, $|| \cdot ||_0$ is a binary-valued function equal to 1 if the transmit power p_j is greater than 0.

Regarding the LEO satellite, the total energy consumption can be expressed as the sum of the inherent energy consumption of the LEO satellite, which accounts for altitude adjustments, GPS navigation, and routing operations, plus the energy consumption of the MBS installed on it, as detailed in (3.20). We suppose that the satellites in the constellation are solar-powered and well-dimensioned. Thus, they can handle both the power requirements needed for an operational satellite and manage the telecom equipment added as payload, based on the growing adoption of real-world projects such as Starlink or Kuiper.

4

Integrated TN-NTN in High Traffic: a Load Balancing Option

4.1 Introduction

As outlined in Chapter 1, future integrated TN-NTN architectures should be able to adapt to varying traffic conditions dynamically. In particular, this adaptability implies an emphasis on load balancing during periods of high traffic, ensuring efficient utilisation of network resources. However, there is a scarce amount of research done on the subject, especially with LEO satellites. The remainder of this chapter is organised as follows. Firstly, we detail our contribution to this field and provide a quick overview of the related works on load balancing methods used in integrated TN-NTN systems and legacy systems. Then, we formally define the problem by describing the variables that we will optimise, the utility function and the performance metrics of interest. Following this, we introduce the framework we developed to optimise this utility function and enable the derivation of optimal resource allocation strategies in a high-traffic scenario. Subsequently, we present and analyse the results of our simulations, demonstrating the effectiveness of the proposed solution. Finally, we conclude the chapter with a summary of key insights.

4.2 Contribution

In this chapter, we propose a new resource management framework to optimise the UE performance by properly controlling the spectrum allocation, the

UE association as well as the transmit power of terrestrial and non-terrestrial MBSs. Our study reveals that, in rural scenarios, NTNs, combined with the proposed radio resource management framework, reduce the number of UEs that are out of coverage in the TN, highlighting the important role of NTNs in providing ubiquitous connectivity, and greatly improve the overall capacity of the network.

This contribution was published in **2023 IEEE International Conference on Communications Workshops (ICC Workshops)**: *H. Alam, A. De Domenico, D. López-Pérez and F. Kaltenberger, "Throughput and Coverage Trade-Off in Integrated Terrestrial and Non-Terrestrial Networks: An Optimization Framework," 2023, pp. 1553-1558, Rome, Italy*.

4.3 Related Works

Load Balancing in TNs is a topic that has also been well studied over the past few years, but in the integrated TN-NTN scenario, the contributions are limited. Typical methods used for load balancing involve the optimisation of a utility function through a pricing-based association strategy [95], [96]. In this line, the authors in [4] have examined an integrated TN-NTN set up in an urban setting, and have shown that diverting some of the traffic to LEO satellites improves the overall signal quality and decreases outages accordingly. The authors of [81] and [56] have exploited the qualities of HAPSs to improve the QoS of ground UEs. [81] has proposed a fairness optimisation approach for integrated TN-NTNs, using MIMO beamforming to improve spectral efficiency and manage interference, demonstrating superior performance over standalone TNs. In contrast, [56] has explored multi-connectivity offloading strategies using UAVs and HAPS in NTNs to reduce task computation latency for time-sensitive applications.
In [62] and [86], the authors have investigated the uplink performance of an integrated TN-NTN, leveraging LEO satellites to provide backhaul support to terrestrial MBSs. Both studies aimed to maximise the total uplink data rate, while adhering to backhaul capacity limits. To do this, [86] has taken into account minimum rate requirements, and has adjusted the bandwidth

division between fronthaul and backhaul links, while [62] has enhanced UE association and power management using matching algorithms.

4.4 Problem Formulation

Since we want to ensure a proportionally fair resource allocation, our goal is to optimise the SLT across all UEs in the network, similarly to [95]. To achieve this goal, we want to find the optimal bandwidth split between the non-terrestrial and terrestrial tiers of the network. Taking this into account, we introduce ε as the share of the bandwidth allocated to the LEO satellites. Thus, the bandwidth W_j of the MBS j can be computed as $W\varepsilon$ if it is a satellite MBS or as $W(1-\varepsilon)$ if it is a terrestrial MBS. Let us also define a binary variable x_{ij} which is equal to 1 if UE i is associated to the MBS j, and 0 otherwise. Our aim is then to optimise the UE-MBS association, the transmit power allocation at each MBS as well as the bandwidth allocation to each tier to maximise the SLT of the network. This can be written as follows:

$$\max_{\mathrm{X},p,k,\varepsilon} \quad \sum_{i\in\mathcal{U}}\sum_{j\in\mathcal{S}} x_{ij}\log\left(\varepsilon R_{ij}\right) + \sum_{j\in\mathcal{T}} x_{ij}\log\left((1-\varepsilon)R_{ij}\right) \tag{4.1a}$$

$$\text{s.t.} \quad x_{ij}\in\{0,1\},\ i\in\mathcal{U}, j\in\mathcal{B}, \tag{4.1b}$$

$$\sum_j x_{ij} = 1,\ \forall i\in\mathcal{U}, \tag{4.1c}$$

$$\sum_i x_{ij} = k_j,\ \forall j\in\mathcal{B}, \tag{4.1d}$$

$$\sum_j k_j = K, \tag{4.1e}$$

$$p_j \le p_{j_{\max}},\ \forall j\in\mathcal{B}, \tag{4.1f}$$

$$\sum_j x_{ij}p_j\beta_{ij} \ge \mathrm{RSRP}_{\min},\ \forall i\in\mathcal{U}, \tag{4.1g}$$

$$\varepsilon\in[0,1]\,, \tag{4.1h}$$

where $\mathrm{p} = [p_1,\ldots,p_L]^T$ is the vector representing the transmit power at each MBS, $\mathrm{k} = [k_1,\ldots,k_L]^T$ is the vector which shows the number of UEs associated to each MBS, and $\mathrm{X} = [x_{ij}]_{i\in\mathcal{U},j\in\mathcal{B}}$ is the binary association matrix. The artificial inclusion of vector k will later allow us to determine whether a MBS is overloaded or not. Constraint (4.1c) ensures that each UE is

associated with a unique MBS, while constraint (4.1e) indicates that all UEs in the network must be served. Furthermore, the maximum transmit power allocated per RE in each MBS j is restricted by $p_{j_{\max}}$ in constraint (4.1f). Finally, constraint (4.1g) ensures the coverage of the entire network by imposing that the minimum RSRP for each UE is greater than a set threshold $\mathrm{RSRP}_{\min}$.

4.5 Utility Optimisation

In this section, we study the solution to our optimisation problem (4.1a). Due to the nature of X, this is a mixed discrete optimisation problem, hence complex to solve. To simplify the problem, we will first optimise the UE-MBS association and the bandwidth allocation considering fixed transmit power, similarly to [96]. Then, we will optimise the transmit power level considering the first two parameters fixed.

4.5.1 Utility optimisation under fixed transmit power

Since the transmit power is fixed, we consider (4.1a) without constraint (4.1f). We can solve this problem using the Lagrange multipliers, as it has been proposed in [95], [96]. We introduce $\lambda = [\lambda_1, \ldots, \lambda_K]^T$, $\mu = [\mu_1, \ldots, \mu_L]^T$, α, and ρ as the dual variables for constraints (4.1g),(4.1d),(4.1e) and (4.1h), respectively.
The Lagrangian function is then:

$$\mathcal{L}(X, k, \varepsilon, \lambda, \mu, \alpha, \rho) = \rho(1-\varepsilon) - \alpha\left(\sum_{j\in\mathcal{B}} k_j - K\right) + \sum_{j\in\mathcal{B}} \mu_j \left(k_j - \sum_i x_{ij}\right)$$
$$+ \sum_i \left(\sum_{j\in\mathcal{S}} x_{ij}\log(\varepsilon R_{ij}) + \sum_{j\in\mathcal{T}} x_{ij}\log((1-\varepsilon)R_{ij})\right) + \sum_i \lambda_i \left(\sum_{j\in\mathcal{B}} x_{ij}p_j\beta_{ij} - \mathrm{RSRP}_{\min}\right). \tag{4.2}$$

After this, we are able to compute the derivative of the Lagrangian with respect to all the variables that we want to optimise, i.e. x_{ij}, k_j and ε, as

$$\frac{\partial \mathcal{L}}{\partial x_{ij}} = \begin{cases} \log\left(\varepsilon R_{ij}\right) + \lambda_i p_j \beta_{ij} - \mu_j, & \text{if } j \in \mathcal{S}, \\ \log\left((1-\varepsilon) R_{ij}\right) + \lambda_i p_j \beta_{ij} - \mu_j, & \text{otherwise.} \end{cases} \tag{4.3}$$

The choice of the MBS association is made by finding which one maximises the derivative. Therefore, we can derive the following expression:

$$x_{ij}^* = \begin{cases} 1, & \text{if } j = \arg\max_{j'} \frac{\partial \mathcal{L}}{\partial x_{ij'}}, \\ 0, & \text{otherwise.} \end{cases} \tag{4.4}$$

This association criterion is actually quite intuitive. Indeed, as we will see later, the dual variable μ_j represents the cost of association to MBS j. Each UE is thus associated to the MBS which maximises the difference between the data rate and the cost of association.

For the vector k, we derive its optimal value by computing the partial derivative of the Lagrangian, and finding its root:

$$k_j^* = e^{\mu_j - \alpha - 1}. \tag{4.5}$$

Finally, we isolate all the terms of the Lagrangian function related to ε, and compute the corresponding partial derivative, which yields:

$$\begin{aligned} \frac{\partial \mathcal{L}}{\partial \varepsilon} &= \frac{\partial}{\partial \varepsilon} \left(\sum_i \left(\sum_{j \in \mathcal{S}} x_{ij} \log(\varepsilon) + \sum_{j \in \mathcal{T}} x_{ij} \log(1-\varepsilon) \right) - \varepsilon \rho \right) \\ &= \frac{1}{\varepsilon} \left(\sum_i \sum_{j \in \mathcal{S}} x_{ij} \right) - \frac{1}{1-\varepsilon} \left(\sum_i \sum_{j \in \mathcal{T}} x_{ij} \right) - \rho \\ &= \frac{1}{\varepsilon} K_{\mathcal{S}} - \frac{1}{1-\varepsilon} \left(K - K_{\mathcal{S}} \right) - \rho, \end{aligned} \tag{4.6}$$

where $K_{\mathcal{S}}$ represents the number of UEs associated to a satellite in the network. Equating (4.6) to 0, we obtain:

$$\rho\varepsilon^2 - (K+\rho)\,\varepsilon + K_{\mathcal{S}} = 0, \tag{4.7}$$

which allows us to find the following optimal value:

$$\varepsilon^* = \frac{K+\rho-\sqrt{(K+\rho)^2 - 4\rho K_{\mathcal{S}}}}{2\rho}. \tag{4.8}$$

From Eq. (4.8), we can observe that the proportion of bandwidth allocated to the non-terrestrial tier is directly proportional to the number of UEs associated with an LEO satellite. In fact, if we gradually increase the value of $K_{\mathcal{S}}$ from 0 to K, the value of ε^* slowly shifts from 0 to 1.
We thereby introduce the Lagrangian dual function, which can be written as:

$$\mathcal{D}\left(\lambda,\mu,\alpha,\rho\right) = \max_{X,k,\varepsilon} \mathcal{L}\left(X,k,\varepsilon,\lambda,\mu,\alpha,\rho\right). \tag{4.9}$$

Accordingly, the Lagrangian problem (4.1a) can then be rewritten as:

$$\min_{\mu,\lambda,\alpha,\rho} \mathcal{D}\left(\lambda,\mu,\alpha,\rho\right). \tag{4.10}$$

By injecting the expressions obtained in (4.4), (4.5), and (4.8), we get:

$$\begin{aligned}
\mathcal{D}\left(\lambda,\mu,\alpha,\rho\right) &= \mathcal{L}\left(X^*,k^*,\varepsilon^*,\lambda,\mu,\alpha,\rho\right) \\
&= \sum_i \left(\sum_{j\in\mathcal{S}} x_{ij}^* \log\left(\varepsilon^* R_{ij}\right) + \sum_{j\in\mathcal{T}} x_{ij}^* \log\left((1-\varepsilon^*) R_{ij}\right) \right) + \rho\left(1-\varepsilon^*\right) \\
&+ \sum_i \lambda_i \left(\sum_j x_{ij}^* p_j \beta_{ij} - \mathrm{RSRP}_{\min} \right) + \sum_j \mu_j \left(k_j^* - \sum_i x_{ij}^* \right) \\
&- \alpha \left(\sum_j k_j^* - K \right).
\end{aligned} \tag{4.11}$$

In order to minimise this function, we use the subgradient method to update the Lagrange multipliers, as already suggested in [95], [96], as follows:

$$\mu_j\left(t+1\right)=\mu_j\left(t\right)-\delta_1(t)\left(k_j^*-\sum_i x_{ij}^*\right), \tag{4.12}$$

$$\lambda_i\left(t+1\right)=\lambda_i\left(t\right)-\delta_2(t)\left(\sum_j x_{ij}^* p_j \beta_{ij}-\mathrm{RSRP}_{\min}\right), \tag{4.13}$$

$$\alpha\left(t+1\right)=\alpha\left(t\right)-\delta_3(t)\left(K-\sum_j k_j^*\right), \tag{4.14}$$

$$\rho\left(t+1\right)=\rho\left(t\right)+\delta_4(t)\varepsilon^*, \tag{4.15}$$

where $\delta_1(t)$, $\delta_2(t)$, $\delta_3(t)$, and $\delta_4(t)$ represent the step-sizes used for each dual variable. Since the dual problem is always convex, the usage of the subgradient method with decreasing step sizes guarantees convergence to the optimal solution of this problem [97].
Eq. 4.12 explains how the proposed framework balances the load among the MBSs. Indeed, as stated previously, μ_j is the cost of association to MBS j. This price will only rise if the right component in the equation is negative, meaning that the number of UEs associated to the MBS is excessively large. This way, a MBS with fewer UEs has a lower cost and is more attractive, whereas MBSs with higher loads become less favourable.

4.5.2 Transmit power optimisation under fixed association

Once the UE-MBS association and bandwidth allocation problem has been solved, we fix X and ε to further optimise the transmit power at each MBS and maximise the network SLT. For ease of reading, we will denote by $f\left(p\right)$ the SLT of the network (4.1a) to indicate that it is a function of the transmit power vector p. The transmit power optimisation problem can then be expressed as:

$$\max_{p} \quad f(p) \tag{4.16a}$$

$$\text{s.t.} \quad \sum_{j} x_{ij} p_j \beta_{ij} \geq \mathrm{RSRP}_{\min},\ \forall i \in \mathcal{U}, \tag{4.16b}$$

$$p_j \leq p_{j_{\max}},\ \forall j \in \mathcal{B}. \tag{4.16c}$$

Since the objective function is concave w.r.t. p, we can try to approximate the zero of the gradient using the Newton-Raphson iterative method to maximise the utility function, as demonstrated in [96]. As suggested in [98], the computational complexity of inverting the Hessian matrix can be reduced by using only its diagonal entries, rather than the full matrix. To this end, the first and second order derivatives are computed as follows:

$$\frac{\partial f(p)}{\partial p_j} = \sum_i \frac{\gamma_{ij}}{r_{ij}\left(1+\gamma_{ij}\right)} \frac{x_{ij}}{p_j} - \sum_i \sum_{j' \neq j} \frac{\beta_{ij}\gamma_{ij'}^2}{\beta_{ij'} r_{ij'}\left(1+\gamma_{ij'}\right)} \frac{x_{ij'}}{p_{j'}}, \tag{4.17}$$

and

$$\begin{aligned} \frac{\partial^2 f(p)}{\partial p_j^2} = &\sum_i \sum_{j' \neq j} \frac{\beta_{ij}^2 \gamma_{ij'}^3 \left(2 r_{ij'} + \gamma_{ij'}\left(r_{ij'} - 1\right)\right)}{\beta_{ij'}^2 r_{ij'}^2 \left(1+\gamma_{ij'}\right)^2} \frac{x_{ij'}}{p_{j'}^2} \\ &- \sum_i \left(\frac{1}{r_{ij}^2} + \frac{1}{r_{ij}}\right) \frac{\gamma_{ij}^2}{\left(1+\gamma_{ij}\right)^2} \frac{x_{ij}}{p_j^2}, \end{aligned} \tag{4.18}$$

where

$$r_{ij} = \log\left(1+\gamma_{ij}\right). \tag{4.19}$$

The Newton step is then:

$$\Delta p_j = \frac{\partial f(p)}{\partial p_j} \Bigg/ \left| \frac{\partial^2 f(p)}{\partial p_j^2} \right|. \tag{4.20}$$

Once we update the transmit power vector using (4.20), it is necessary to project the value in a region where constraints (4.16b) and (4.16c) are respected. Naturally, the upper bound of our feasible region is the maximum transmit power for each MBS. For the lower bound, we utilise the minimal coverage constraint, i.e. we know that for a MBS j, all UEs associated to

it should be receiving a signal power greater than $\mathrm{RSRP}_{\min}$. This can be translated as:

$$\forall i \in \mathcal{U}_j, \quad p_j \quad \geq \quad \frac{\mathrm{RSRP}_{\min}}{\beta_{ij}}, \tag{4.21}$$

with $\mathcal{U}_j$ being the set of UEs associated to MBS j. We are therefore able to establish the lower bound of the feasibility region for each MBS j as:

$$\tau_j = \max_{i \in \mathcal{U}_j} \left(\frac{\mathrm{RSRP}_{\min}}{\beta_{ij}} \right). \tag{4.22}$$

Finally, the transmit power update done at the end of step t is written as such:

$$p_j^{(t+1)} = \left[p_j^{(t)} + \delta_5(t) \Delta p_j \right]_{\tau_j}^{p_{j\max}}, \tag{4.23}$$

with $\delta_5(t)$ being a step-size factor.

4.6 Simulation Results & Analysis

In this section, we assess the effectiveness of our proposed optimisation framework for UE association, bandwidth allocation, and transmit power control in an integrated TN-NTN. As previously mentioned in Chapter 3, we analyse a rural scenario where the terrestrial MBSs are deployed in an hexagonal grid layout [90].
It is important to note that, in this particular contribution, we do not account for satellite mobility as discussed in Sect. 3.2.2. Instead, we assume a constant elevation angle throughout the analysis. Also, we do not factor in the UE antenna gain G_{UE} nor building entry losses when computing the channel models outlined in 3.3 and 3.13.

As for the UE deployment, we consider an inhomogeneous deployment. Indeed, we first randomly select 30% of the terrestrial MBSs, and for these MBSs, we deploy the UEs in a "hot-spot" manner, to possibly create overload in the related cells and allow our framework to demonstrate its effectiveness.

Parameter	Value
Total Bandwidth W	40 MHz
Carrier frequency f_c	2 GHz
Subcarrier Spacing	15 kHz
UE density	2 UE/km^2
Inter-Site Distance	1732 m
Number of Macro BSs	1067
Terrestrial Max Tx Power per RE $p_{\max}$ [99]	17.7 dBm
Satellite Max Tx Power per RE $p_{\max}$ [40]	15.8 dBm
Antenna gain (Terrestrial) G_{Tx} [100]	14 dBi
Antenna gain (Satellite) G_{Tx} [40]	30 dBi
Shadowing Loss (Terrestrial) SF [91]	$4-8$ dB
Shadowing Loss (Satellite) SF [44]	$0-12$ dB
Line-of-Sight Probability (Satellite / Terrestrial)	Provided in [44] / [91]
White Noise Power Density [100]	-174 dBm/Hz
Coverage threshold $\mathrm{RSRP}_{\min}$	-120 dBm

Tab. 4.1: Simulation parameters.

Half of the UEs are deployed among those hot-spots, and the other half are uniformly spread across the entire area. The most important simulation parameters, set according to [40], [44], [91], [99]–[101], are listed in Table 4.1.

Benchmarks

To compare and assess the performance of both developed algorithms, we introduce the two following benchmarks: The `3GPP-TN` configuration includes only a TN operating on a bandwidth of 10 MHz. In contrast, the `3GPP-NTN` configuration includes a satellite network overlaying the terrestrial one. In this case, the bandwidth is divided according to the 3GPP suggestions in [40], with 30 MHz assigned to the satellite tier and 10 MHz to the terrestrial one. In both configurations, the UEs associate to the MBSs based on the max-RSRP rule, with no DL transmit power optimisation.

4.6.1 Framework convergence analysis

In this section, we analyse the convergence of the proposed optimisation framework. Specifically, Figure 4.1 shows the iterative evolution of 1) the network SLT, along with 2) the optimal bandwidth split (ε) and 3) the actual fraction of UEs associated to the satellite in the network, i.e. $\frac{k_0}{\sum_j k_j}$.

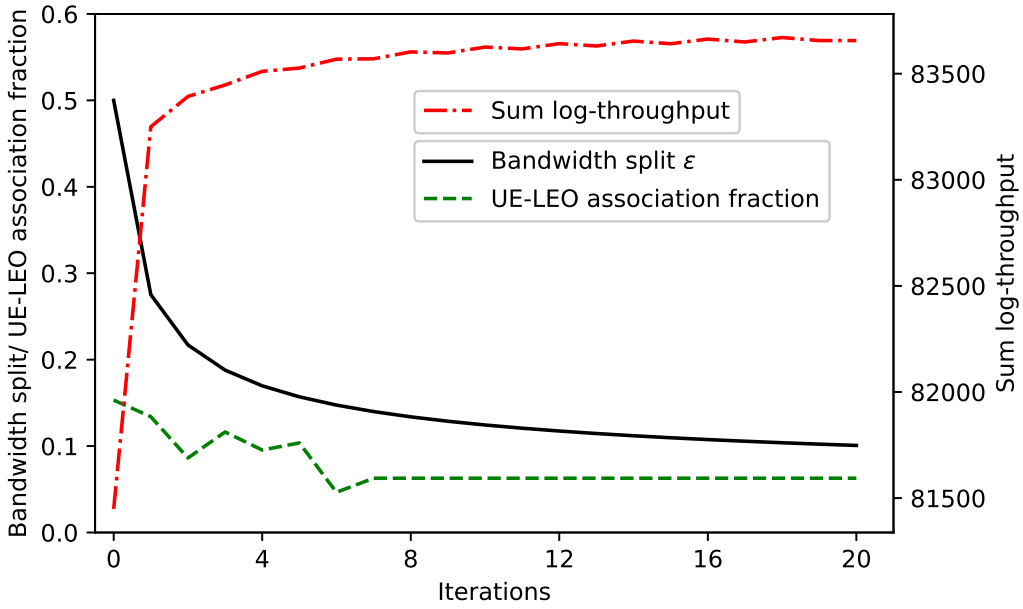

Fig. 4.1: Evolution of the bandwidth allocation proportion and the utility function of our framework.

When initialising the algorithm presented in Sec. 4.5, the bandwidth split, ε is set to 0.5, and the fraction of UEs associated to the LEO satellite is 0.15. Note that the initial UE-MBS association follows the max-RSRP rule. During the iterative process, we can see that the SLT continuously improves, while the ratio of UEs associated to the LEO satellite and the fraction of bandwidth allocated to it decreases. Eventually, the algorithm converges after 20 iterations, with an improved SLT and 11% of the bandwidth being allocated to the LEO satellite and approximately 6% of the UEs associated to it. Note that this bandwidth split is different than the one recommended in 3GPP specifications [40]. Considering that all MBSs were initially transmitting at their maximum power, we observe an 82% decrease of the average transmit power. This is explained by the fact that our framework reduces the transmit

power of the MBSs that have no UEs and thus no coverage constraint (4.1g) to uphold.

In the following, we denote by ε_{opt} the optimal bandwidth split derived by the proposed framework.

4.6.2 Network coverage analysis

In this section, we study the benefits of integrating a NTN to a TN in terms of coverage, i.e. the capability to provide wireless services. Figure 4.2 shows the cumulative distribution function (CDF) of the RSRP perceived at each UE from the serving MBS in the following four scenarios:

1. The `3GPP-TN` setting.
2. A scenario where all the bandwidth is allocated to the terrestrial network ($\varepsilon = 0$) and the UE association and power control is done through our framework.
3. The `3GPP-NTN` setting.
4. The scenario where bandwidth split, association, and power are allocated through the proposed framework (ε_{opt}).

In the first two scenarios, we observe a similar performance in terms of coverage since all the UEs are served by MBSs, which leads to 7% of the UEs to be out of coverage since their respective RSRPs are below the threshold $p_{\min}$. In contrast, when integrating the NTN in the last two scenarios, the proportion of UEs out of coverage drastically drops down to around 0.4 %. Indeed, the satellite can reach UEs located at the cell edge and provide them with a signal of much better quality than that provided by the strongest MBSs.

4.6.3 UE rate analysis

In this section, we compare the data rate performance achieved by our framework with the one of the `3GPP-TN` and `3GPP-NTN` settings. Also, we

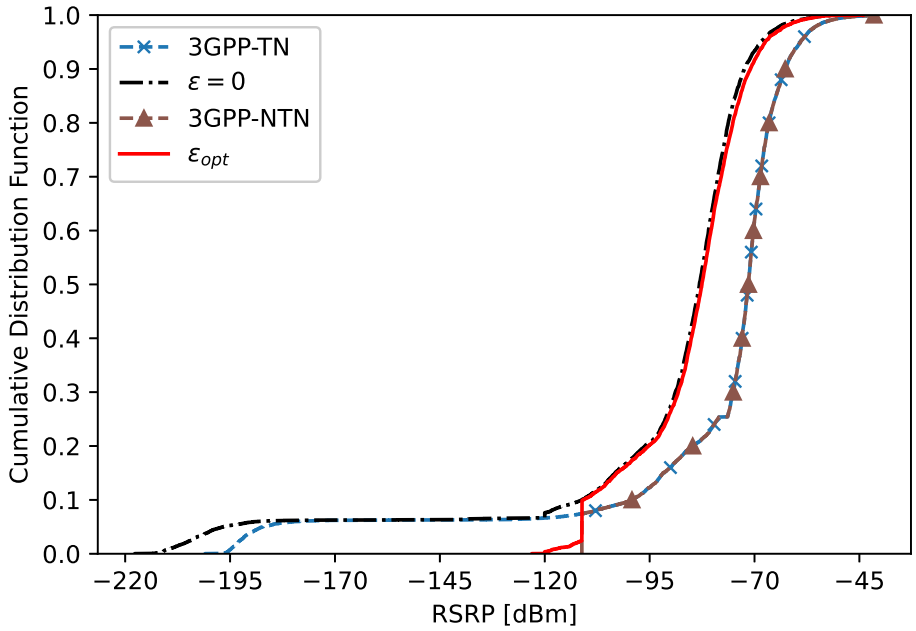

Fig. 4.2: CDFs of the UE RSRP, with (ε_{opt}, `3GPP-NTN`) and without ($\varepsilon = 0$, `3GPP-TN`) an active satellite.

consider the case where only the user association and the power control are optimised and the bandwidth split is fixed, i.e., $\varepsilon \in \{0, 0.25, 0.5, 0.75\}$. Figure 4.3 shows the CDFs of the data rate achieved when considering the various deployment and resource allocation scenarios.

Also, Table 4.2 presents the 5-th percentile, the mean, the median, and the 95-th percentile of the different data rate distributions resulting from the most relevant of the compared solutions.

	$\varepsilon = 0$	ε_{opt}	$\varepsilon = 0.75$	`3GPP-NTN`	`3GPP`
5-th Percentile (kbps)	0	81	614	558	0
Mean (Mbps)	44.4	38.3	12.0	11.7	11.1
Median (Mbps)	28.3	27.1	7.7	7.3	7.1
95-th Percentile (Mbps)	136.6	112.7	37.0	36.4	34.1

Tab. 4.2: Data-rate analysis.

We first notice that higher data rates, in average, are achieved when we allocate a large split of the bandwidth to the terrestrial network. This is because of the large spectrum reuse in the area under investigation.

However, it is important to note that the tail of the rate distribution greatly suffers if we prioritise the terrestrial network when controlling the spectrum split. With the `3GPP-TN` setting and when all the bandwidth is allocated to macro BSs ($\varepsilon = 0$), around 7% of the UEs are out of coverage, as we observed in the previous section, and their rate is null. When the NTN bandwidth is increased, the coverage holes of the network are reduced, and the rate experienced by the cell edge UEs increases. This can be observed in the zoom of Fig. 4.3. Overall, we can highlight the underlying trade-off

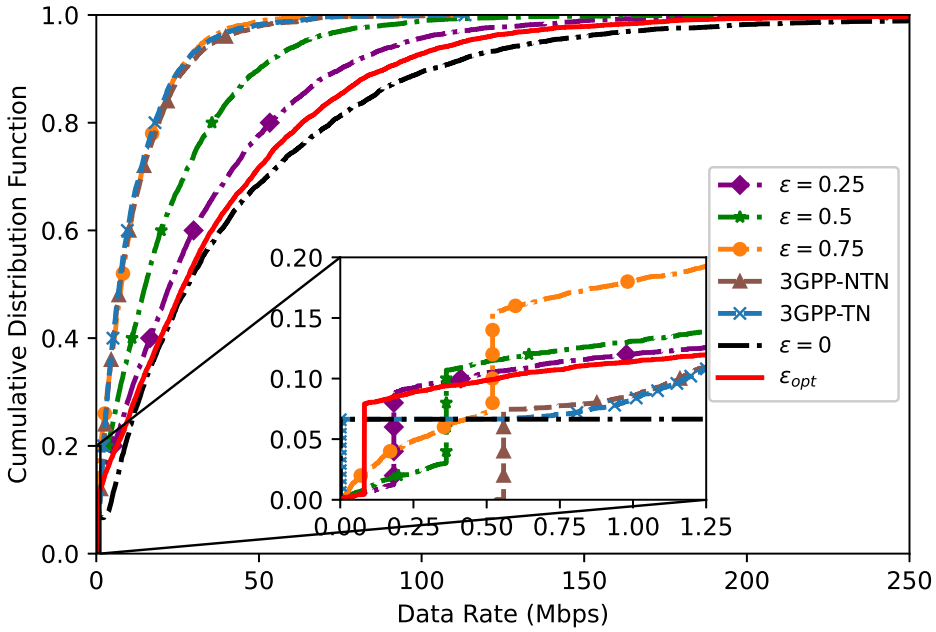

Fig. 4.3: CDFs of UE data rates for various bandwidth allocation settings.

between cell-edge (5-th percentile UEs) and cell-center (mean/median and 95-th percentile UEs) throughput. If the operator gives a small share of the bandwidth to the satellite, it may achieve large cell-center UE data rates at the expense of coverage holes and degraded performance at the cell edge. In contrast, if the operator decides to allocate a large share of the bandwidth to the satellite, the cell edge performance greatly improves, at the expense of the cell-center UE data rate. For example, a UE which would be out of

coverage when $\varepsilon = 0$ or in the 3GPP-TN scenario experiences a data rate of roughly 81 kbps if, using the proposed framework, we optimally set ε to 0.11. With our proposal, the mean UE rate decreases by 14% with respect to the setting of $\varepsilon = 0$ but results in a gain of more than 200 $\%$ with respect to the 3GPP-TN and the 3GPP-NTN settings. Therefore, our framework is able to find the best solution to this trade-off by improving the coverage condition of the UEs that suffer from large path losses whilst providing large data rates to cell-center UEs.

4.7 Conclusion & Perspectives

In this chapter, we have proposed a framework to control the UE association, transmission power, and bandwidth allocation between terrestrial and satellite tiers. Our proposal is able to distribute the load, while mitigating the number of coverage holes and maximising the SLT in the network. Specifically, we demonstrated that incorporating a LEO satellite atop the TN in rural areas significantly reduces the proportion of out-of-coverage UEs. Additionally, by examining the scenario where both tiers share the bandwidth, we highlighted the trade-off between minimising coverage holes and maximising network SLT, and struck the optimal balance point. Finally, our results indicate that the UE-MBS association resulting from our framework greatly improves the performance of the network in terms of mean and 95-th percentile of throughput compared to the max-RSRP rule.
However, this work exclusively addressed the high-traffic scenario, where the demand is at its peak. In the next chapter, we will study the versatility of an integrated TN-NTN and how it can enhance overall network performance given any traffic load.

5

BLASTER: A Tool for Traffic-Aware Network Optimisation

5.1 Introduction

After developing a framework which can efficiently improve the network performance in high traffic in the previous chapter, we aim to extend our work to varying traffic loads, evaluating the adaptability and effectiveness of integrated TN-NTNs in dynamic network environments. Specifically, with varying traffic loads come distinct demands that need to be addressed: in high-traffic conditions, the focus shifts to efficiently balancing the load across the network, while in low-traffic scenarios, the priority shifts towards reducing the energy consumption of the network.

The rest of this chapter is structured as follows: First, we present a brief review of the related works on MBS activation methods applied in integrated TN-NTN systems as well as incumbent TNs. Then, we formulate the optimisation problem in mathematical terms, with a clear presentation of the relevant parameters and the utility function to be optimised. Subsequently, we present the solutions we developed for this problem and assess their performance by comparing them to the benchmarks defined previously. Finally, we conclude the chapter by providing a summary highlighting the main findings of the chapter.

5.2 Contribution

This chapter presents a novel radio resource management algorithm, BLASTER (Bandwidth SpLit, User ASsociation, and PowEr ContRol), which integrates bandwidth allocation, UE association, power control, and MBS activation within an integrated TN-NTN. This algorithm aims to optimise network resource allocation fairness and energy consumption dynamically, demonstrating new opportunities in deploying satellite networks in legacy cellular systems. Also, by exploiting the special properties of the formulated optimisation problem, we design a practical heuristic with an intuitive behaviour to solve the problem with limited complexity, achieving results that highlight the trade-off between enhancing network SLT and reducing energy consumption.

The contents of this chapter have been published or submitted in the following venues:

- Published in **2024 IEEE 35th International Symposium on Personal, Indoor and Mobile Radio Communications (PIMRC)**: *H. Alam, A. De Domenico, F. Kaltenberger and D. López-Pérez, "On the Role of Non-Terrestrial Networks for Boosting Terrestrial Network Performance in Dynamic Traffic Scenarios," 2024, pp. 1-7, Valencia, Spain*.

- Published in **Elsevier Academic Press 2026**: *M. Schellmann, M.A Jamshed, G. Karetsos, H. Alam, A. De Domenico, F.R. Davoli, S. Adhatarao, Y. Chen and A. Kaushik, "**Non-Terrestrial Networks**, Chapter 12: NTN standardization in 5G NR and the path beyond," 2026, pp. 285-312, ISBN: 9780443265266.*

- Submitted to **IEEE Transactions on Vehicular Technology**: *H. Alam, A. De Domenico, D. López-Pérez and F. Kaltenberger, "Optimizing Integrated Terrestrial and Non-Terrestrial Networks Performance with Traffic-Aware Resource Management*".

5.3 Related Works

MBSs activation is a well-studied topic in TNs, although research in integrated TN-NTNs remains limited but is slowly gaining momentum. The authors of [102] have introduced an energy-efficient algorithm that strategically shuts down MBSs one at a time, ensuring they do not overburden neighbouring MBSs. To preserve the QoS, [103] has examined the effects of traffic offloading in heterogeneous networks (HetNets) on energy use, and proposed a centralised Q-learning method to strike a balance between energy saving and QoS satisfaction. In addition, the authors of [104] have devised an algorithm that enables UEs to associate with multiple MBSs across different frequency bands, simultaneously optimising the transmit power of the MBSs to facilitate their shutdown during periods of low traffic. The authors of [105] have also tackled traffic uncertainties in ultra-dense networks by optimising both MBS activation and UE association strategies, employing chance constraint programming based on statistical traffic data to effectively balance traffic loads and reduce interference.

Recent studies such as [106]–[108] have explored the integration of HAPS to enhance network efficiency in a more dynamic and sustainable manner. Indeed, [106] has investigated how HAPSs can complement traditional network densification to manage dynamic traffic in urban areas, demonstrating better energy efficiency and sustainability by using HAPSs to handle peak demand periods. In [107], the authors have tackled the traffic load estimation issue in HAPS-assisted networks, proposing Q-learning algorithms to optimise cell-switching strategies, improving energy efficiency and making advanced cell-switching methods feasible for vertical heterogeneous networks. The authors of [108] have investigated the challenges of MBSs activation in an integrated TN-NTN using HAPS, focusing on offloading traffic from deactivated terrestrial MBSs to the HAPS, mainly using a sorting algorithm, which prioritises switching off MBSs with relatively lower traffic loads. Although the studies in [106]–[108] have provided valuable insights and promising results, they have not explored the optimisation of spectrum sharing and allocation strategies, thereby limiting resource utilisation efficiency in integrated TN-NTNs. To the best of our knowledge, only the authors of [107] and [108] have considered NTNs as a solution for meeting coverage and capacity demands while deactivating MBSs.

5.4 Problem Formulation

Our objective is to develop a framework, which simultaneously increases UE performance and reduces network energy consumption by adjusting the resource distribution between satellite and terrestrial MBSs in response to the hourly fluctuations in network traffic. Specifically, our goal is to achieve proportional fair resource allocation by optimizing the network SLT, while limiting the TN energy consumption: in fact, the nature of the logarithmic cost function discourages each MBS to allocate disproportionate resources to a single UE. Let us denote as ε the fraction of the bandwidth allocated to the LEO satellites at a given hour of the day; then, the bandwidth allocated for an MBS j can be written as:

$$W_j = \begin{cases} \varepsilon W & \text{if } j \in \mathcal{S}, \\ (1-\varepsilon)\, W & \text{else.} \end{cases} \tag{5.1}$$

Also, we define x_{ij}, a binary variable, which equals 1 if UE i is associated to MBS j. Accordingly, the perceived throughput for UE i can then be reformulated as:

$$R_i = \sum_{j \in \mathcal{B}} x_{ij} R_{ij.} \tag{5.2}$$

To achieve our goal —strike the optimal balance between maximizing the network SLT while minimizing the total TN energy consumption—, we optimise the split of the bandwidth between the terrestrial and non-terrestrial tier, the UE association, the MBS transmit power as well as the activation of each MBS. This problem can be summed up as the following:

$$\max_{X, \varepsilon, p} \quad \sum_{i \in \mathcal{U}} \log(R_i) - \lambda \sum_{j \in \mathcal{T}} Q_j(p_j) \tag{5.3a}$$

$$\text{s.t.} \quad x_{ij} \in \{0,1\},\ i \in \mathcal{U}, j \in \mathcal{B}, \tag{5.3b}$$

$$\tilde{\beta} \cdot p \geq \mathrm{RSRP}_{\min} \cdot \mathbb{1}_K, \tag{5.3c}$$

$$p_j \leq p_{j_{\max}},\ \forall j \in \mathcal{B}, \tag{5.3d}$$

$$\varepsilon \in [0,1]\,. \tag{5.3e}$$

Here, $X = [x_{ij}] \in \mathbb{R}^{K \times L}$ represents the UE-MBS association matrix, $p = [p_1, \ldots, p_L]^T \in \mathbb{R}^L$ is the transmit power vector, and $\mathbb{1}_K = [1, \ldots, 1]^T \in \mathbb{R}^K$.

Also, $\tilde{\beta} = X \odot \beta$ is a matrix of dimension $K \times L$, resulting from an element-wise multiplication of matrices X and β. λ is a regularisation parameter that allows us to control the trade-off between UE performance (higher SLT) and network energy consumption[1]. Constraint (5.3b) states that x_{ij} is a binary variable. Constraint (5.3c) is the coverage constraint: it ensures that the perceived RSRP for each UE is greater than the set threshold $RSRP_{\min}$. Also, (5.3d) guarantees that the transmit power per RE for each MBS j does not exceed $p_{j_{\max}}$. The indicator variable x_{ij} enforces a unique association, making the problem combinatorial. As highlighted in [95], UE association and resource allocation are interdependent. Also, the transmit power of each MBS further complicates optimisation by affecting signal strength and coverage. Consequently, predicting the behaviour of the utility function becomes challenging because of these interdependencies.

Moreover, given the fact that the energy consumption model detailed in (3.20) is not a continuous function, the problem may prove hard to optimise. Hence, we approximate it using a L_1-L_2 penalty function. The choice and nature of this function push for a sparse solution, as shown in [109]. A sparse solution is ideal as it entails shutting down several MBSs, thus effectively reducing the network energy consumption. We can then reformulate our initial problem as:

$$\max_{X,\varepsilon,p} \quad \sum_{i\in\mathcal{U}} \log(R_i) - \lambda \left(||p||_1 + \sum_{j=1}^{L} \psi_j w_j ||p||_2 \right) \tag{5.4a}$$

$$\text{s.t.} \quad \text{(5.3b)} - \text{(5.3e)}, \tag{5.4b}$$

where $||\cdot||_1$ and $||\cdot||_2$ represent the L_1 and L_2 norm respectively. w_j denotes the power weighting of MBS j. These weights vary inversely with the transmit power of each MBS, thus prompting the shutdown of those with lower transmit power.

[1] We discuss how to set λ based on the expected UE traffic in Sec. 5.6.1.

5.5 Designed Solutions

In this section, we first present BLASTER, the framework proposed to address the optimisation problem outlined in (5.4a)-(5.4b). Then, we design a low-complexity heuristic based on the special characteristics of the problem, and provide a comparison for BLASTER w.r.t. performance state-of-the-art benchmarks. Finally, we provide an analysis of the complexity of both solutions.

5.5.1 BLASTER

We adopt the BCGA algorithm to solve problem (5.4a)-(5.4b). BCGA is a technique used to maximise a function by iteratively updating its different parameters. Similar to the framework presented in Chapter 4, we begin by optimising the UE-MBS association and bandwidth split while considering the transmit power fixed. Then, we optimise the transmit power at each MBS whilst keeping the two previous parameters unchanged. The full overview is provided in Algorithm 1.

Utility optimisation under fixed transmit power

Let f represent the utility function we aim to maximise in (5.4a). By relaxing constraint (5.3b) such that $x_{ij} \in [0, 1]$, we get a convex optimisation problem with respect to X. To tackle this problem, the iterative gradient projection method serves as an ideal solution [110], given its suitability for constrained optimisation. The gradient projection method involves calculating the gradient of the objective function and then projecting this gradient onto the viable region delineated by the problem constraints. Adopting the gradient projection method, we can determine the gradient update at iteration s as follows:

$$\tilde{X}(s) = X(s) + \alpha \nabla_X f\left(X, p, \varepsilon\right), \tag{5.5}$$

Algorithm 1 BLASTER Framework

Data: K UEs and L MBs.

Initialisation:
s = 0
X: Association done through max-RSRP
p: Transmit power set to maximum
$\varepsilon = 0.5$; `// Equal bandwidth split`

Compute: $f\left(X, \varepsilon, p\right)$; `// Initial point`

$w = [1, \ldots, 1] \in \mathbb{R}^L$
Initialise $\alpha \in \mathbb{R}^{K \times L}$
Initialise $\mu \in \mathbb{R}^K$
Initialise $\eta \in \mathbb{R}^L$
Initialise $\delta \in \mathbb{R}$
while *Utility function f has not converged* **do**
  `// UE Association and bandwidth split`
  Compute: $\tilde{X}(s) = X(s) + \alpha \nabla_X f\left(X, p, \varepsilon\right)$ (5.5)
    Solve (5.13a) using gradient projection to obtain μ^*
    Compute: $X(s+1) = \max\{\tilde{X}(s) - \beta \odot p^{\mathrm{PAD}} \odot \mu^{*\mathrm{PAD}}, 0\}$(5.14)
    $\varepsilon^* = \frac{K_S}{K}$ (5.18)
    `// Power control step`
  Compute: $\tilde{p}(s) = p(s) + \eta \nabla_p f\left(X, p, \varepsilon\right)$ (5.20)
    Compute: $t = \lambda \cdot \eta \cdot w^T \psi$ (5.22)
    Compute: $\hat{p}(s) = \max\left\{1 - \frac{t}{||\tilde{p}(s)||_2}, 0\right\}\tilde{p}(s)$ (5.23)
    Compute: τ based on (4.22)
    Compute: $p(s+1) = \left[\hat{p}(s)\right]_{\tau}^{p_{\max}}$ (5.26)
    $w = \left[\frac{1}{p_1 + \delta}, \ldots, \frac{1}{p_L + \delta}\right]$
    `//` δ `small constant to avoid numerical instability`
  Compute: $f\left(X(s), \varepsilon, p(s)\right)$
   $s = s + 1$
end
return *X,ε,p*

where $\alpha \in \mathbb{R}^{K\times L}$ is a convenient step-size and ∇ denotes the gradient operator. The projection into the feasible region can be achieved solving the following problem:

$$\min_{X(s)} \quad \frac{1}{2}||X(s) - \tilde{X}(s)||_F^2 \tag{5.6a}$$

$$\text{s.t.} \quad \tilde{\beta} \cdot p \geq \text{RSRP}_{\min} \cdot \mathbb{1}_K, \tag{5.6b}$$

where $||\cdot||_F$ represents the Frobenius norm. To lighten the reading, for the remainder of this section, we omit the iteration indices. We employ the Lagrange multipliers method to address the projection problem (5.6a)-(5.6b). With this in mind, we compute the Lagrangian function associated with the problem (5.6a) - (5.6b):

$$\begin{aligned}\mathcal{L}(X,\mu) &= \frac{1}{2}||X - \tilde{X}||_F^2 + \left(\tilde{\beta}\cdot p - RSRP_{\min}\cdot \mathbb{1}_K\right)^T \mu \\ &= \frac{1}{2}||X||_F^2 - \text{Tr}\left(X^T\tilde{X}\right) + \frac{1}{2}||\tilde{X}||_F^2 + \left(\tilde{\beta}\cdot p\right)^T \mu - \left(RSRP_{\min}\cdot \mathbb{1}_K\right)^T \mu,\end{aligned} \tag{5.7}$$

where $\mu \in \mathbb{R}^K$ is the Lagrange multiplier associated with constraint (5.3c). Calculating the gradient of (5.7) with respect to X, we obtain:

$$\nabla_X \mathcal{L}(X,\mu) = X - \tilde{X} + \beta \odot \underbrace{\left(\mathbb{1}_K \cdot p^T\right)}_{:=p^{\text{PAD}}} \odot \underbrace{\left(\mu \cdot \mathbb{1}_L^T\right)}_{:=\mu^{\text{PAD}}}. \tag{5.8}$$

Fixing the dual variable, we are able to determine the minimal point for the gradient, which is obtained for:

$$X^\star = \max\{\tilde{X} - \beta \odot p^{\text{PAD}} \odot \mu^{\text{PAD}}, 0\}. \tag{5.9}$$

Subsequently, we can introduce the Lagrangian dual function, formulated as:

$$\mathcal{D}(\mu) = \max_X \mathcal{L}(X,\mu). \tag{5.10}$$

Proposition 1. *We can rewrite $\mathcal{D}(\mu)$ as:*

$$\mathcal{D}(\mu) = \frac{1}{2}||X^\star||_F^2 - \mathrm{Tr}\left(X^\star\left[\tilde{X} - \beta \odot p^{\mathrm{PAD}} \odot \mu^{\mathrm{PAD}}\right]^T\right) - \left(RSRP_{\min} \cdot \mathbb{1}_K\right)^T \mu. \tag{5.11}$$

Proof. Please refer to Appendix A. □

Also, we notice that for any matrix A:

$$\frac{1}{2}\left|\left|\max\{A, 0\}\right|\right|_F^2 - \mathrm{Tr}\left(\max\{A, 0\}A^T\right) = -\frac{1}{2}\left|\left|\max\{A, 0\}\right|\right|_F^2 \tag{5.12}$$

Then, combining Proposition 1 with (5.12), we are able to rewrite the dual problem associated to the projection step problem (5.6a) - (5.6b) as the following:

$$\min_{\mu} \quad \frac{1}{2}||X^\star||_F^2 \; + \; \left(RSRP_{\min} \cdot \mathbb{1}_K\right)^T \mu \tag{5.13a}$$

$$\text{s.t.} \quad \mu \leq 0. \tag{5.13b}$$

To solve problem (5.13a)-(5.13b) detailed above, we can utilise the gradient projection problem, as the constraint is a simple projection into the non-positive orthant. Once we find the solution μ^*, we can recover the optimal solution to problem (5.6a)-(5.6b) by:

$$X(s+1) \triangleq X^\star = \max\{\tilde{X}(s) - \beta \odot p^{\mathrm{PAD}} \odot \mu^{*\mathrm{PAD}}, 0\}. \tag{5.14}$$

We repeat those iterations until convergence to obtain the optimal association setting X^*.

Once this is done, we have to optimally split the bandwidth between both terrestrial and non-terrestrial tiers. To this aim, we rewrite the mean UE throughput, defined in (3.16), as follows:

$$R_{ij} = \begin{cases} \varepsilon r_{ij} & \text{if } j \in \mathcal{S}, \\ (1-\varepsilon)\, r_{ij} & \text{otherwise}, \end{cases} \tag{5.15}$$

where

$$r_{ij} = \frac{W}{k_j} \log_2\left(1 + \gamma_{ij}\right).$$

Note that, since in (5.15) both the MBS transmit power and the noise power scale linearly with the bandwidth, γ_{ij} is unaffected by the bandwidth split between satellite and TN.

Proposition 2. *The optimal bandwidth allocation for the non-terrestrial tier linearly increases with the fraction of UEs associated to a satellite MBS in the network, provided that all UEs have the same requirements, i.e.:*

$$\varepsilon^* = \frac{K_{\mathcal{S}}}{K} \tag{5.16}$$

where $K_{\mathcal{S}}$ denotes the number of UEs associated to a satellite within the network.

Proof. First, we compute the gradient of our utility function f with respect to ε:

$$\begin{aligned}
\nabla_{\varepsilon} f\left(X, p, \varepsilon\right) &= \frac{\partial}{\partial \varepsilon}\left(\sum_{i=1}^{K} \log\left(R_i\right)\right) = \sum_{i=1}^{K} \frac{\partial}{\partial \varepsilon} \log\left(R_i\right) \\
&= \sum_{i=1}^{K} \frac{\frac{\partial}{\partial \varepsilon}\left(R_i\right)}{R_i} = \sum_{i=1}^{K} \frac{\frac{\partial}{\partial \varepsilon}\left[\sum\limits_{j \in \mathcal{S}} \varepsilon x_{ij} r_{ij} + \sum\limits_{j \in \mathcal{T}} \left(1-\varepsilon\right) x_{ij} r_{ij}\right]}{R_i} \\
&= \sum_{i=1}^{K} \frac{\sum\limits_{j \in \mathcal{S}} \frac{\partial}{\partial \varepsilon}\left[\varepsilon x_{ij} r_{ij}\right] + \sum\limits_{j \in \mathcal{T}} \frac{\partial}{\partial \varepsilon}\left[\left(1-\varepsilon\right) x_{ij} r_{ij}\right]}{R_i} = \sum_{i=1}^{K} \left[\frac{\sum\limits_{j \in \mathcal{S}} x_{ij} r_{ij} - \sum\limits_{j \in \mathcal{T}} x_{ij} r_{ij}}{R_i}\right].
\end{aligned} \tag{5.17}$$

Let us denote as $\mathcal{U}_{\mathcal{S}}$ and $\mathcal{U}_{\mathcal{T}}$ the sets of UEs served by the satellites and terrestrial MBSs respectively, such that $\mathcal{U} = \mathcal{U}_{\mathcal{S}} \cup \mathcal{U}_{\mathcal{T}}$.
Then, by setting (5.17) to 0, we can strike the optimal splitting point for the bandwidth as follows:

$$\begin{aligned}
\nabla_{\varepsilon} f\left(X, p, \varepsilon\right) = 0 \Leftrightarrow \sum_{i \in \mathcal{U}_{\mathcal{S}}} \frac{1}{\varepsilon} + \sum_{i \in \mathcal{U}_{\mathcal{T}}} \frac{-1}{1-\varepsilon} = 0 \Leftrightarrow \frac{K_{\mathcal{S}}}{\varepsilon} - \frac{K - K_{\mathcal{S}}}{1-\varepsilon} = 0 \\
\Leftrightarrow \varepsilon^* = \frac{K_{\mathcal{S}}}{K}.
\end{aligned} \tag{5.18}$$

□

Transmit power optimisation under fixed association

Once we have solved the UE association and bandwidth allocation problem, we consider those two parameters as constant and focus on adjusting the transmit power at each terrestrial MBS to maximise the utility function introduced in (5.4a). The problem of optimizing the transmit power can thus be articulated as:

$$\max_{p} \quad \sum_{i \in \mathcal{U}} \log(R_i) - \lambda \left(||p||_1 + \sum_{j=1}^{L} \psi_j w_j ||p||_2 \right) \tag{5.19a}$$

$$\text{s.t.} \quad \text{(5.3c)} - \text{(5.3d)} \tag{5.19b}$$

Owing to the discontinuous nature of the L_1 norm, we need to employ the iterative proximal gradient method [111] for the resolution of (5.19a)-(5.19b). To do that, we first compute the gradient update at iteration s as follows:

$$\tilde{p}(s) = p(s) + \eta \nabla_p f\left(X, p, \varepsilon\right) \tag{5.20}$$

where $\eta \in \mathbb{R}^L$ is a pertinent step-size. Then, as outlined in [111], the proximal gradient method updates p by addressing the problem described below:

$$\min_{p} \quad \frac{1}{2} ||\tilde{p}(s) - p(s)||_2^2 + t||p(s)||_2 \tag{5.21a}$$

with

$$t = \lambda \cdot \eta \cdot w^T \psi. \tag{5.22}$$

A closed-form solution to this problem, known as block-soft thresholding [111, Sec. 6.5.1] is expressed as:

$$\hat{p}(s) = \max\Big\{1 - \frac{t}{||\tilde{p}(s)||_2}, 0\Big\}\tilde{p}(s). \tag{5.23}$$

After updating the transmit power vector, it is necessary to project it into a feasible region to ensure compliance with constraints (5.3c) and (5.3d). The maximum transmit power per RE naturally sets the upper limit of our feasible region. To determine the lower boundary, we apply the minimal coverage constraint. Indeed, as indicated by (5.3c), each UE connected to

a MBS j must receive a signal power that exceeds the minimum required RSRP value, $\mathrm{RSRP}_{\min}$. This can be rewritten as:

$$\forall i \in \mathcal{U}_j, \quad p_j \quad \geq \quad \frac{\mathrm{RSRP}_{\min}}{\beta_{ij}}, \tag{5.24}$$

with $\mathcal{U}_j$ representing the set of UEs connected to the MBS j. Consequently, we can define the lower bound of the feasible region for each MBS j as:

$$\tau_j = \max_{i \in \mathcal{U}_j} \left(\frac{\mathrm{RSRP}_{\min}}{\beta_{ij}} \right). \tag{5.25}$$

Finally, the transmit power update at the iteration s can be computed as follows:

$$p(s+1) = \Big[\hat{p}(s) \Big]_{\tau_j}^{p_{\max}}. \tag{5.26}$$

After the algorithm yields $p(s+1)$, we adjust the power weights w_j following the re-weighting algorithm described in [104]. Indeed, we update the vector w as follows:

$$w(s+1) = \left[\frac{1}{p_1 + \delta}, \ldots, \frac{1}{p_L + \delta} \right] \tag{5.27}$$

where δ is a parameter introduced to avoid numerical instability. By updating the vector w based on (5.27), we reduce the impact on the utility function of the MBSs that have a large transmit power to provide continuous coverage to the associated UEs. In contrast, this weighing method effectively pushes MBSs that are not providing traffic to decrease the transmit power further until they shutdown.

5.5.2 Heuristic development

Given that BLASTER is composed of two iterative methods (BCGA and gradient projection method to solve (5.13a)), we have developed a low computational complexity heuristic based on the domain expertise. The designed heuristic has a structure similar to that of BLASTER. Indeed, it first deals with the UE-MBS association phase and allocates the bandwidth resources accordingly. Then, it deactivates part of the MBSs in the network and/or updates their transmit power. The heuristic algorithm iteratively repeats these three steps until the selected utility function, i.e., the network SLT converges. Specifically,

the three steps of the proposed low computational complexity heuristic can be described as the following:

- *UE Association:* To maximise the number of terrestrial MBSs that can be switched off during low-traffic hours (0 AM - 7 AM), it is desirable to maximise the share of the traffic served by the non-terrestrial tier. Hence, the proposed heuristic associates each UE that has an RSRP larger than $\mathrm{RSRP}_{\min}$ to the satellite. For each remaining UEs that is yet to be associated to a MBS, we collect the perceived RSRPs from all the MBSs that are providing an RSRP greater than $\geq \mathrm{RSRP}_{\min}$. Then, we average these RSRP measurements and rank each UE based on the calculated average from worst to best. Then, starting from the UE with the poorest average, we associate it with the MBS providing the largest throughput with the aim of maximizing the SLT.
  In the case of a high-traffic scenario, the satellite merely acts as an umbrella over the ground network to provide service for UEs that have no service, and potentially facilitate the distribution of the load. In this regard, the UE association process is quite similar to the low-traffic scenario as we rank each UE based on their average perceived RSRP and associate to the MBS providing the best throughput[2].

- *Bandwidth split:* The bandwidth is split according to the expression derived in (5.18).

- *MBS shutdown and power control:* In low-traffic scenario, the proposed heuristic shuts down all MBSs serving less UEs than a set threshold T_{UE}, provided that these UEs can be successfully handed over to neighbouring MBSs. We also reduce the MBS transmit power as long as the coverage constraint (5.3c) is satisfied for the connected UEs (feasible region computed in (5.25)). On the other side, for high traffic, we only shut down inactive MBSs and reduce the transmit power similarly to the low-traffic scenario.

The complete heuristic is detailed in Algorithm 2.

[2]Note that the association is done only once for each UE and does not change even if the associated MBS is not providing the best throughput anymore due to the increased number of served UEs.

Algorithm 2 Heuristic

Data: K UEs and L MBs.

Initialisation
  s = 0
  X: Association done through max-RSRP
  p: Transmit power set to maximum
  $\varepsilon = 0.5$; `// Equal bandwidth split`
Compute: SLT `// Initial point`
while *SLT has not converged* **do**
  `// UE Association and bandwidth split`
  if *low-traffic hour:* **then**
    for *all UEs u* **do**
      if *RSRP perceived from satellite* $\geq \mathrm{RSRP}_{\min}$ **then**
        Associate UE u to the satellite
      end
    end
  end
  Rank each UE according to the average perceived RSRP
  for *all UEs u uncovered* **do**
    $\mathcal{C}$: List of MBSs providing an RSRP greater than $\mathrm{RSRP}_{\min}$ for UE u
    Associate u to the MBS $\in \mathcal{C}$ providing the largest throughput.
  end
  $\varepsilon^* = \frac{K_S}{K}$ (5.18) `// Power control step`
  if *low-traffic hour:* **then**
    for *all MBSs b serving less than T_{UE}* **do**
      if *we can handover every UE served by b* **then**
        Offload each UE to a neighboring MBS
        Shutdown MBS b
      end
    end
  end
  `// For remaining active BSs:`
  Compute: τ based on (5.25) `// Reduce Tx Power while ensuring coverage for all UEs:`
  Compute: $p(s+1) = \tau$
  $s = s + 1$
end
Return X,ε,p

5.5.3 Complexity Analysis

Concerning the algorithmic complexity, we can compare both solutions that we have developed:

`BLASTER` complexity

First, let's analyse the complexity of the operations in an iteration of `BLASTER`. For the optimisation of X, the computation of the gradient step (5.5) has a complexity of $\mathcal{O}(K \times L)$. In addition, we solve a gradient projection problem (5.13a) at the end of the UE association phase using an iterative method. Each iteration of the gradient projection method is executed with a complexity of $\mathcal{O}(K \times L)$. We denote as I_μ the number of iterations needed to reach a stopping criterion for the gradient projection method. The stopping criterion is either the convergence of the utility function (SLT) or the completion of a given number of iterations. Then, the overall complexity for the optimisation of X is $\mathcal{O}(K \times L + I_\mu \times K \times L) = \mathcal{O}(I_\mu \times K \times L)$. To obtain the optimal split of the bandwidth as per (5.18), our algorithm computes the fraction of the UEs associated to the satellites, which is an operation of complexity $\mathcal{O}(K)$. Finally, the transmit power vector optimisation has an overall complexity of $\mathcal{O}(K \times L)$. Taking all of this into account, if I_{blaster} represents the number of iterations needed to meet a stopping criterion for `BLASTER` (specified above), the complexity of the framework is $\mathcal{O}(I_{\text{blaster}} \times I_\mu \times K \times L)$.

Heuristic complexity

For modelling the heuristic complexity, we consider separately low and high traffic cases. In the low-traffic scenario, the proposed algorithm associates to a satellite each UE perceiving an RSRP greater than $\mathrm{RSRP}_{\min}$ from a satellite. This results in having to do the ranking and MBS association process detailed above for $K - K_{\mathcal{S}}$ UEs. Therefore, in low traffic, the complexity of the UE association phase is $\mathcal{O}((K - K_{\mathcal{S}}) \times L)$. Also, the complexity of the operations for the transmit power optimisation and BS activation is $\mathcal{O}(K \times L)$. Therefore, the overall complexity for one iteration in a low-traffic scenario is $\mathcal{O}(K \times L)$. For the high-traffic case, the complexity for those

steps is $\mathcal{O}(K \times L)$, explained by the fact that the UE association process is done for each of the UEs. Finally, denoting by I_H the number of iterations needed for the utility function to converge, the overall complexity of the heuristic is $\mathcal{O}(I_H \times K \times L)$.

5.6 Simulation Results & Analysis

In this section, we assess the performance of the proposed solution under different traffic conditions. All the results and analyses presented in the following section have been conducted over a 24-hour observation window, with snapshots of the network taken at the start of each hour, and generated using a custom-built system-level simulator following the 3GPP recommendations for the channel model. We model the traffic variations by changing the number of active UEs in the network. Precisely, the number of UEs deployed in the network scales according to the daily downlink traffic load pattern presented in Chapter 1. The number of UEs decreases during the night, until it reaches its minimum of 400 at 5 AM, and increases in high traffic, reaching up to $10\,000$ at 8 PM. The UEs are deployed uniformly across the entire study area, with a higher density of deployment in the urban area relatively to the rural one. In our simulation setting, we consider that 80 % of the UEs are indoor [91]. Table 5.1 lists the primary simulation parameters used in this study, incorporating several minor additions and modifications to those shown in Table 4.1.

Benchmarks

As in Chapter 4, we introduce two benchmark scenarios to compare with our proposed framework. The `3GPP-TN` configuration comprises solely a TN operating with a bandwidth of 10 MHz. Conversely, the `3GPP-NTN` configuration features a NTN that overlays the TN. In this setup, the total bandwidth is allocated following the guidelines provided by 3GPP in [40], assigning 30 MHz to the satellite tier and 10 MHz to the terrestrial tier. In both scenarios, UEs associate to MBSs based on the max-RSRP criterion, without employing DL transmit power optimisation nor MBS shutdown.

Parameter	Value
Total Bandwidth W	40 MHz
Carrier frequency f_c	2 GHz
Subcarrier Spacing	15 kHz
Urban/Rural Inter-Site Distance	$500/1\,732\ m$
Number of Macro BSs	1 776
Satellite Altitude [40]	600 km
Terrestrial Max Tx Power per RE $p_{\max}$ [99]	17.7 dBm
Satellite Max Tx Power per RE $p_{\max}$ [40]	15.8 dBm
Antenna gain (Terrestrial) $G_{\mathrm{T_X}}$ [100]	14 dBi
Antenna gain (Satellite) $G_{\mathrm{T_X}}$ [40]	30 dBi
Shadowing Loss (Terrestrial) SF [91]	$4\ -\ 8$ dB
Shadowing Loss (Satellite) SF [44]	$0\ -\ 12$ dB
Line-of-Sight Probability (Terrestrial / Satellite)	Refer to [91] / [44]
White Noise Power Density	-174 dBm/Hz
Coverage threshold $\mathrm{RSRP}_{\min}$	-120 dBm
Urban/Rural UEs distribution proportion	40%/60%
UE Antenna gain G_{UE} [44]	0 dBi
Satellite baseline energy consumption E_c	500 J

Tab. 5.1: Simulation parameters.

5.6.1 Optimisation of the regularisation parameter

As specified in Section 5.4, λ is a regularisation parameter, which allows to control the trade-off between maximising network SLT and minimising the TN energy consumption (see (4.1a)). Indeed, a high value of λ leads BLASTER to increase the number of shutdown MBSs, as the priority becomes to reduce the TN energy consumption. Conversely, a low value of λ indicates that the focus is on improving the SLT, by balancing the load and ensuring a proportional fair resource allocation. To achieve this goal, in our study, we set λ inversely proportional to the number of UEs, K, in the network as follows:

$$\lambda = \frac{\lambda_{\max} K_{\min}}{K}, \tag{5.28}$$

where $\lambda_{\max}$ is the value of λ when the UEs number is equal to its lowest, i.e., $K_{\min}$. This approach allows us to simplify the setting of the hyper-parameter

λ, by fixing $\lambda_{\max}$ and using (5.28). Therefore, in the following, we investigate the impact of $\lambda_{\max}$ on the behaviour of BLASTER. In particular, we let $\lambda_{\max}$ take values in $\{10, 1e3, 1e7, 1e10\}$, and study the corresponding distribution of the SLT during high and low traffic as well as that of the total TN energy consumption. In Fig. 5.1, we see a clear trend, with larger values of $\lambda_{\max}$

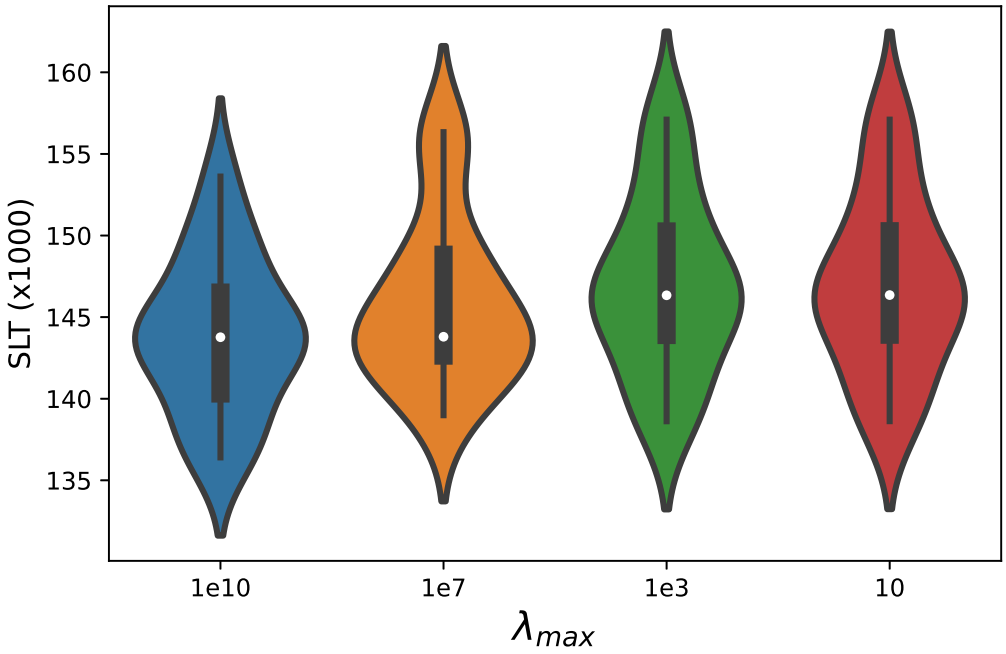

Fig. 5.1: Sum Log Throughput distribution achieved by BLASTER in high traffic for various $\lambda_{\max}$.

leading to a downward shift of the SLT distribution during high traffic. In fact, we observe a gradual increase of the median value of the SLT in high traffic, as $\lambda_{\max}$ decreases. This is in line with our assumption that a small value of λ moves the focus from the TN energy consumption to improving the SLT. Specifically, in Fig. 5.1, we see a $2\,\%$ increase of SLT by varying $\lambda_{\max}$ from the largest value ($\lambda_{\max} = 1e10$) to the smallest one ($\lambda_{\max} = 10$). Note that, during high traffic, the performance in terms of SLT stagnates, once $\lambda_{\max}$ starts crossing extremely high values.

Conversely, in Fig. 5.2, we notice that there is a limited change of the SLT, if the value of $\lambda_{\max}$ varies. In fact, in low traffic scenarios, our framework aims mainly to reduce the TN energy consumption, i.e., maximising the SLT has limited importance.

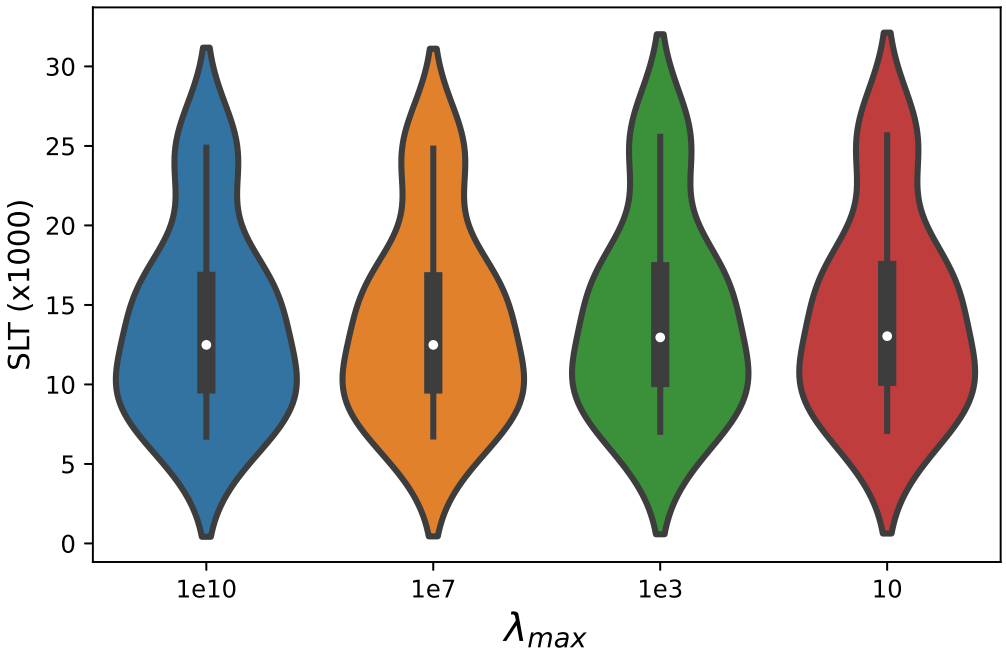

Fig. 5.2: Sum Log Throughput distribution achieved by BLASTER in low traffic for various $\lambda_{\max}$.

To verify this analysis, Fig. 5.3 plots the TN energy consumption for the distinct values of $\lambda_{\max}$, specified previously. We remark that the TN energy consumption increases throughout the day when the value of $\lambda_{\max}$ decreases. Indeed, a small value of $\lambda_{\max}$ hampers the transmit power optimisation in (5.23), as each update becomes negligible, making it hard to effectively drive down the energy consumption of the TN.

Through these results, we are able to grasp the trade-off between reducing energy consumption and balancing the network load efficiently. Indeed, we observe that limiting the value of $\lambda_{\max}$, i.e., $\lambda_{\max} = 10$ and $\lambda_{\max} = 1e3$, we only achieve, during high traffic hours, a minor gain in terms of network SLT of approximately 2% compared to the other cases ($\lambda_{\max} = 1e7$ and $\lambda_{\max} = 1e10$), while the total energy consumption surges by approximately 84%. Considering all of this, we fix $\lambda_{\max} = 1e7$ as this value ensures a balanced performance in both SLT and TN energy consumption.

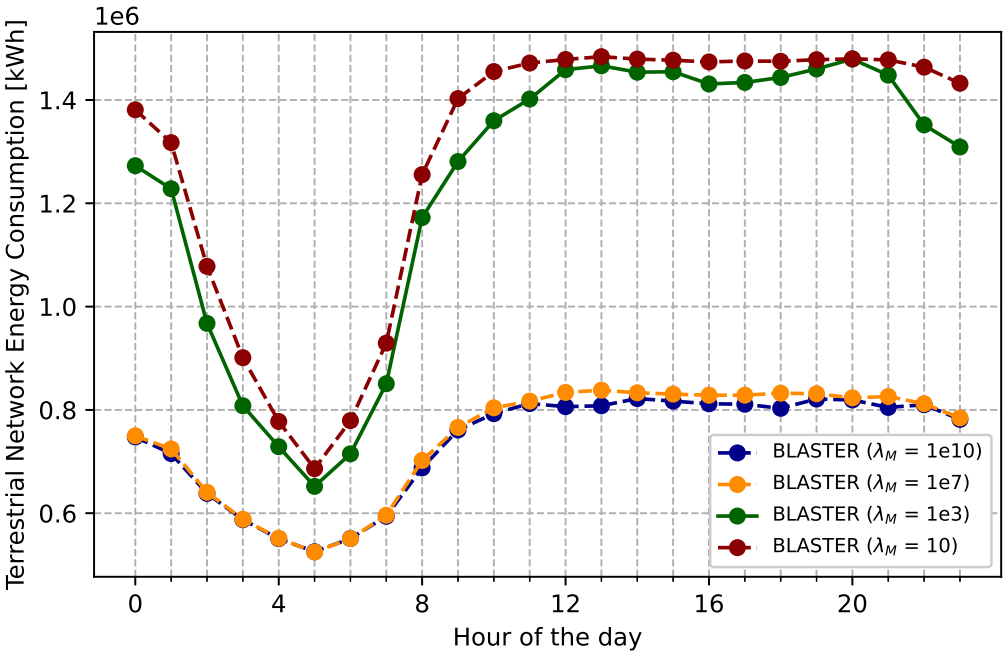

Fig. 5.3: Daily profile of the terrestrial network energy consumption achieved by BLASTER for various $\lambda_{\max}$.

5.6.2 Complexity and Convergence Analysis

In Fig. 5.4, we display the operational complexity of both proposed frameworks BLASTER and HEURISTIC as derived in Section 5.5.3. We notice that the operational complexity of BLASTER is higher than HEURISTIC throughout the day. This is expected, as the latter framework is implemented using less complex operations compared to the former, which resorts to multiple gradient descent methods. In fact, we see an average decrease in operational complexity of approximately 21% in the day, which underlines the simplicity of HEURISTIC compared to BLASTER. Moreover, we notice that the complexity follows a pattern similar to the traffic load for both frameworks, which corroborates with the formulas derived in 5.5.3. Indeed, a lower number of total UEs K naturally leads to a lower complexity, as seen in Fig. 5.4. On the opposite, a surge in traffic results in an increased complexity due to a higher number of operations needed to complete both frameworks.

To illustrate the convergence of BLASTER, we analyse the relative gain between successive iterations. A positive relative gain indicates an increase in

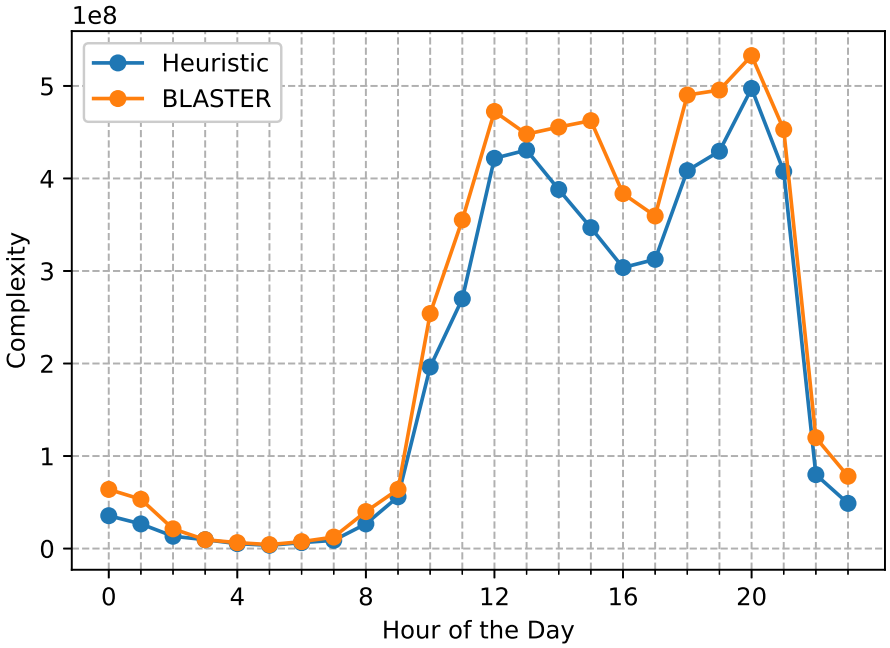

Fig. 5.4: Daily profile of the complexity of BLASTER and HEURISTIC.

the objective function, whereas a negative relative gain implies a decrease. Fig. 5.5 presents the average relative gain per iteration along with the corresponding standard deviation, computed across multiple runs of BLASTER at different hours of the day. Initially, we observe a sharp increase in relative gain, followed by a steady decline towards zero. Notably, the relative gain remains positive for the vast majority of iterations, confirming that the objective function generally improves over time. This behaviour highlights the convergence of BLASTER which on average occurs after approximately 30 iterations.

5.6.3 Impact of the Satellite Network on Traffic Distribution

In this section, we look at the shifting role that the satellites play on the mobile network throughout the day. Fig. 5.6 presents the daily profile of the fraction of UEs associated with the satellite network in the different frameworks under investigation. Also, we plot the hourly number of UEs deployed

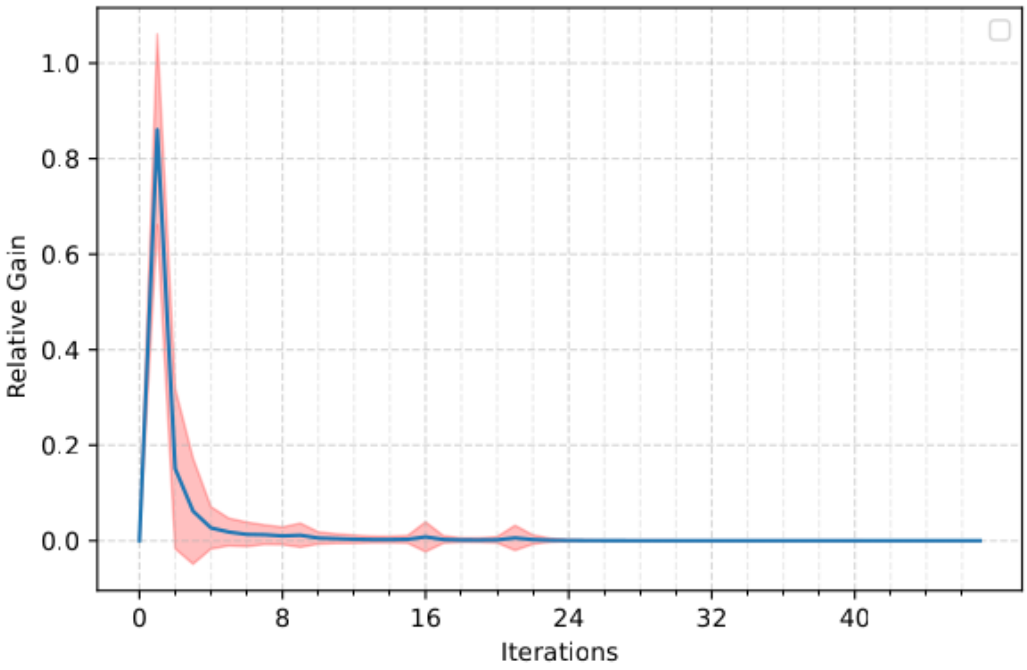

Fig. 5.5: Average relative gain per iteration for BLASTER.

in the network, represented by the black dotted line. As we have previously underlined, the priority for the proposed BLASTER and HEURISTIC frameworks during low traffic is to reduce the TN energy consumption. Hence, the satellite becomes a compelling option for offloading the TN and shutting down lightly loaded MBSs. Fig. 5.6 shows that BLASTER and HEURISTIC achieve a $70\,\%$ and $500\,\%$ increase of the fraction of UEs associated to the satellite network in low-traffic hours as compared to the benchmark 3GPP-NTN. Also, we notice that the proportion of UEs associated to the satellite is far greater for HEURISTIC compared to BLASTER. This is due to the fact that HEURISTIC ensures that every UE that has a signal strength greater than $\mathrm{RSRP}_{\mathrm{min}}$ is associated to the satellite, opposed to the more sophisticated BLASTER, who would still consider the available throughput before associating to the satellite. Conversely, during high traffic hours, we notice that the satellite network takes a less prominent role for both BLASTER and HEURISTIC, essentially acting as an umbrella, providing service to UEs that would otherwise be out of coverage. Accordingly, most of of the total bandwidth is allocated to the terrestrial tier, which can efficiently serve more UEs than the non-terrestrial tier and can significantly improve the spatial reuse.

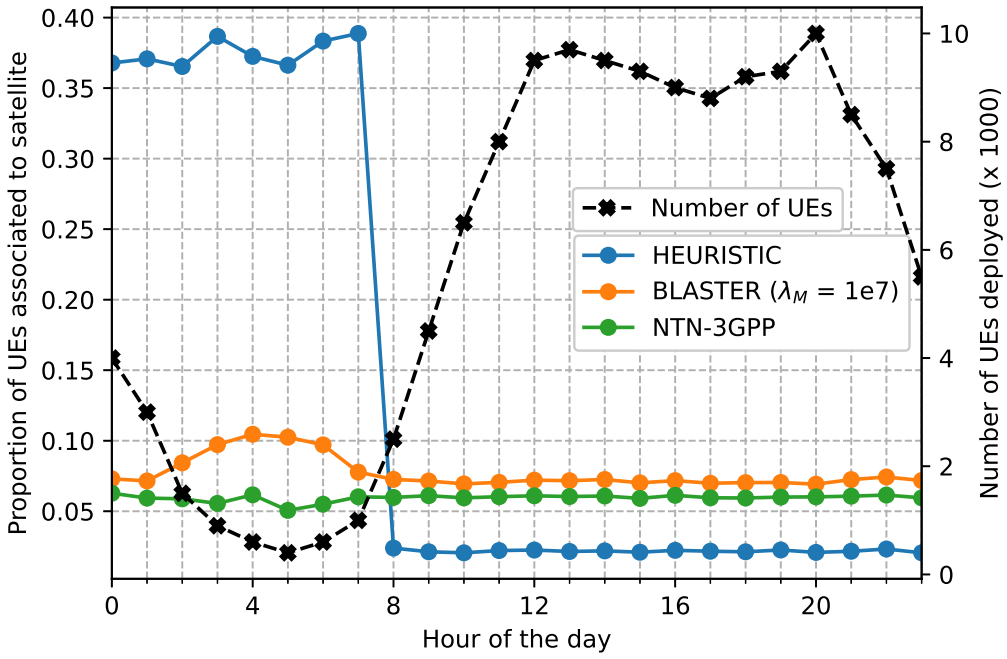

Fig. 5.6: Daily profile of the proportion of UEs associated to the satellite network.

5.6.4 Analysis on the Network Sum Log-Throughput

In this section, we analyse the SLT achieved by the algorithms under investigation throughout the day and, in particular, how they adapt the network resources to the daily variations of the traffic load. Fig. 5.7 shows the daily profile of the SLT achieved by the schemes under investigation, and Fig. 5.8 presents the relative SLT gain for `BLASTER`, `HEURISTIC` and `3GPP-NTN` compared to `3GPP-TN`.

Remember that in `3GPP-TN` there are no satellites available to serve UEs perceiving low RSRP from terrestrial MBSs. In addition, the total bandwidth available for the TN is only 10 MHz, which leads to low UE throughput, especially during busy hours. As expected, we observe an SLT performance improvement with the integration of satellites into the network. Indeed, LEO satellites are able to provide service to cell-edge UEs, which do not perceive a signal strong enough to be served from the terrestrial tier, thereby increasing the network SLT.
In more detail, in Fig. 5.7, we can see that both `BLASTER` and the proposed `HEURISTIC` outperform the `3GPP-NTN` benchmark, with an average SLT in-

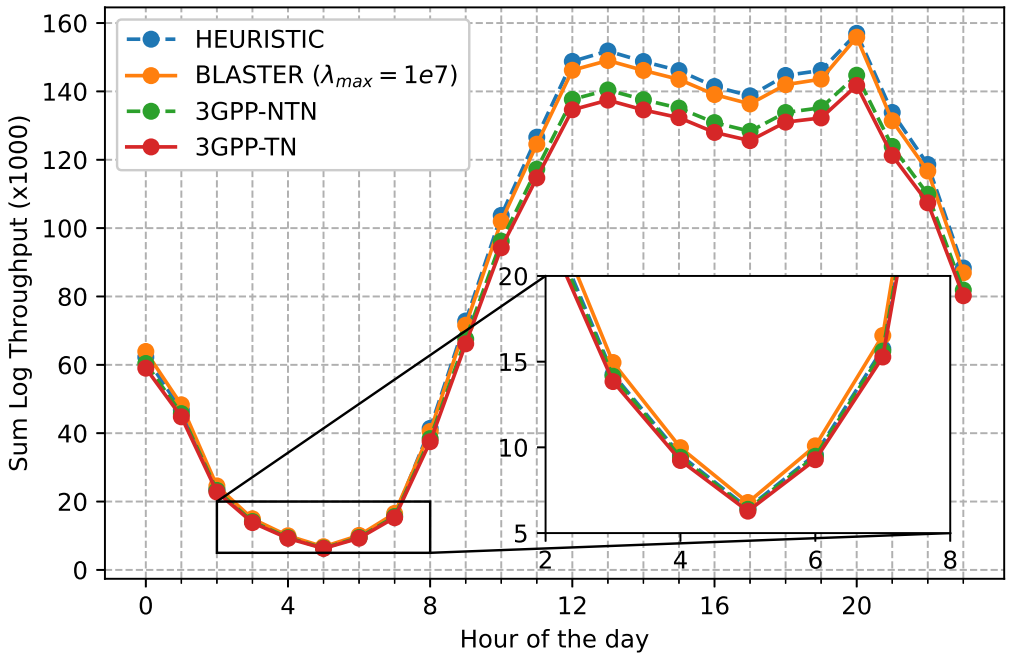

Fig. 5.7: Daily profile of the sum log throughput.

crease of approximately $6\,\%$ across the day, highlighted in Fig. 5.8. Moreover, and although the SLT gain for `3GPP-NTN` in Fig. 5.7 is more visually discernible during high-traffic hours, note that its relative gain with respect to `3GPP-TN`, illustrated in Fig. 5.8 does not change drastically and remains around 2% throughout the day.

In low traffic, Fig. 5.8 underlines that `BLASTER` outperforms `HEURISTIC` in terms of SLT. This is due to the different association methods used for both proposed frameworks. As detailed in Section 5.6.3, the association criterion to the satellite in `HEURISTIC` is more lenient, which results to more UEs sharing the resources of the satellite, leading to a deteriorated throughput for its UEs and a worse SLT performance. Note that the improvement compared to the `3GPP` benchmarks is more apparent during high traffic hours, typically midday to end of evening than low traffic hours. Indeed, as detailed before, the onus of both the `HEURISTIC` and `BLASTER` during low traffic is on reducing energy consumption, which explains the mitigated improvement of the network SLT.

During high traffic, both algorithms strive to balance the traffic load to maximise the SLT, which explains the striking improvement with respect to `3GPP-NTN` and `3GPP-TN`. That gain is due to various reasons. First of all,

the UE-MBS association methods of HEURISTIC and BLASTER are designed to ensure a proportional fair resource allocation, which increases the SLT. In addition, the dynamic split of the network bandwidth based on the time-varying fraction of UEs associated to the satellite network (see Proposition 2) allows the proposed HEURISTIC and BLASTER to astutely distribute the frequency resources, differently than the 3GPP benchmarks [40]. In fact, since the majority of UEs are associated to a terrestrial MBS (see Fig. 5.6), a larger share of the resources are allocated to the terrestrial tier, which leads to a larger provided data-rate than the one achievable following the 3GPP benchmarks. By splitting the bandwidth based on the fraction of UEs associated to the satellites, we observe an enhancement of the mean SLT by at least 8% and 6% for both the proposed frameworks compared to 3GPP-TN and 3GPP-NTN respectively.

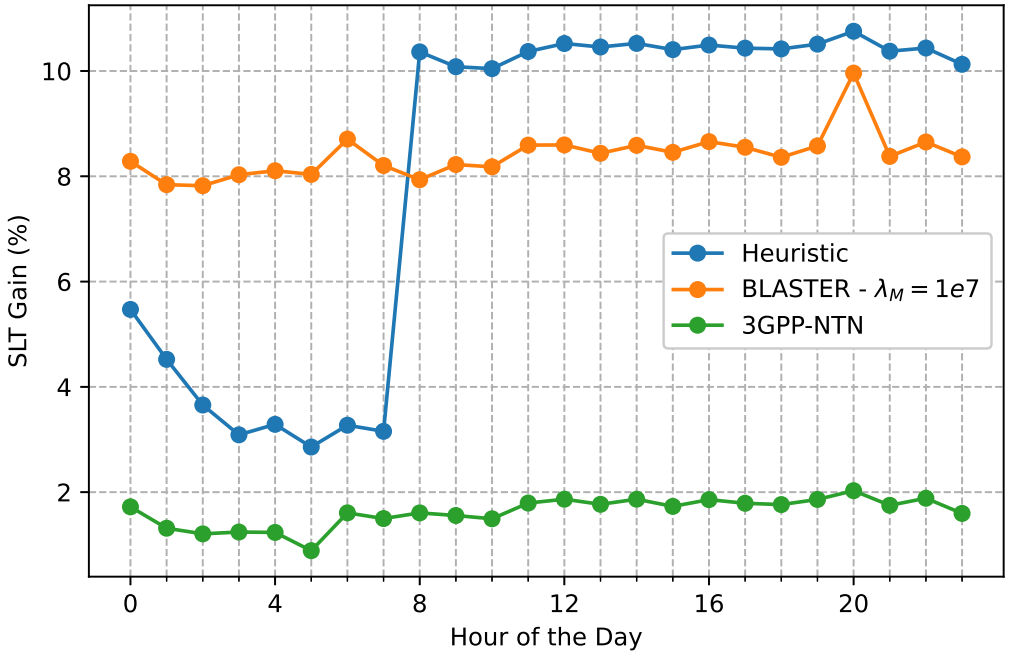

Fig. 5.8: Relative gain of the sum log throughput compared to 3GPP-TN.

5.6.5 Analysis on the Network Energy Consumption

In this section, we study the performance of the proposed BLASTER and HEURISTIC in terms of energy usage. To this end, Fig. 5.9 displays the TN

energy consumption throughout the day for the various algorithms under investigation.

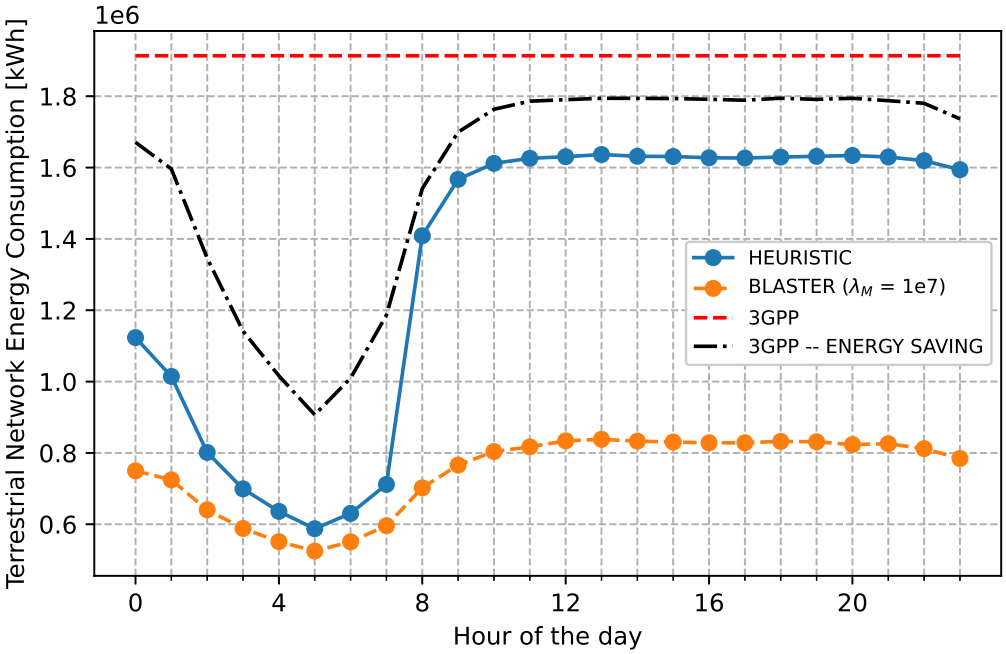

Fig. 5.9: Daily profile of the TN energy consumption.

The red dotted line represents the energy consumption level for both `3GPP-TN` and `3GPP-NTN` settings, for which the TN energy consumption is at maximum level through the entire day, as they do not integrate neither power control nor MBS shutdown. Also, the black dotted line represents the same setting as `3GPP-TN`, but with the added mechanism of shutting down all inactive MBSs when they have no UEs, denoted `3GPP-ENERGY SAVING`. This setting reduces the average daily energy consumption by 17 % compared to `3GPP` benchmarks, due to its ability to shut down MBSs, which leads to a more efficient energy use. As discussed in Section 5.6.3, with `BLASTER` and `HEURISTIC`, the satellite network serves a larger proportion of UEs during low traffic than the standard `3GPP-NTN`, which facilitates the shutdown of terrestrial MBSs. This is apparent in Fig. 5.9, as, in low traffic, the TN energy consumption sees an average decrease of approximately $67\,\%$ and $54\,\%$ for the `BLASTER` and `HEURISTIC` settings with respect to the benchmark `3GPP-NTN` and `3GPP-TN`, respectively. In comparison, for the `3GPP-ENERGY SAVING` configuration, `BLASTER` and `HEURISTIC` experience a decrease of approximately $49\,\%$ and $31\,\%$, respectively. We also notice that, even though, during the

low-traffic hours, the HEURISTIC is characterised by a larger share of UEs associated to the satellite network than the BLASTER, it still leads to a larger TN energy consumption. Interestingly, the transmit power optimisation of BLASTER allows for a greater reduction of the transmit power of the TN MBSs. Indeed, the transmit power vector update step for BLASTER (5.20) - (5.26) is specifically designed to solve the optimisation problem, reducing the terrestrial MBSs transmit power efficiently while the HEURISTIC updates the transmit power for terrestrial MBSs based on a rule of thumb, which suffices to reduce the network energy consumption.

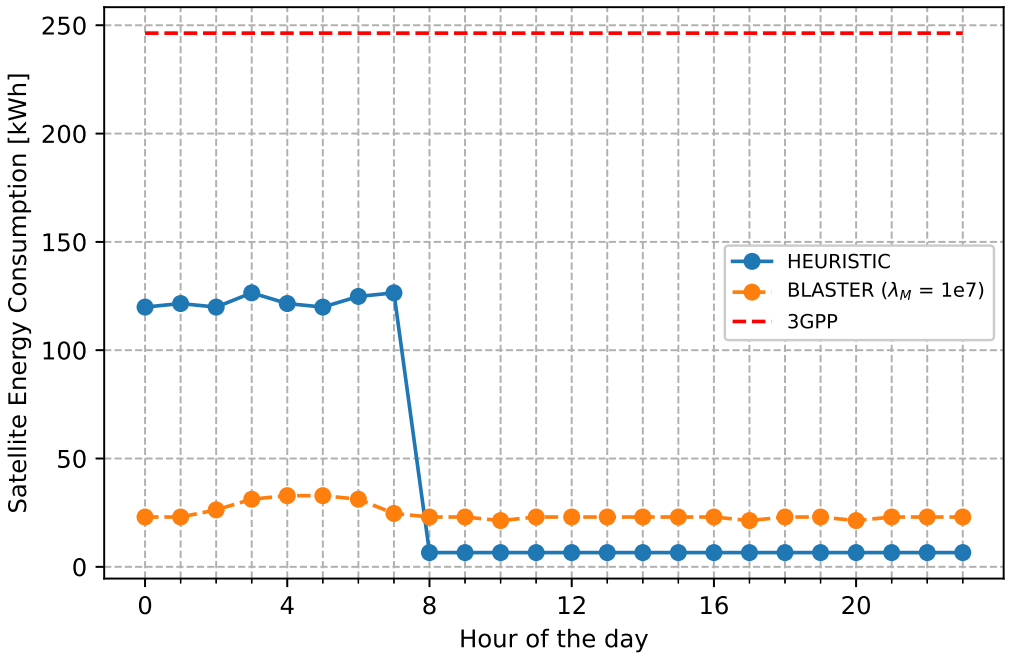

Fig. 5.10: Daily profile of the satellite energy consumption

This also explains the striking difference in the high-traffic scenario, as the average energy consumed by the network is reduced by around $56\,\%$ and $14\,\%$ for BLASTER and HEURISTIC respectively, compared to the TN energy consumption in the 3GPP benchmarks. This result further underlines the flexible nature of both proposed frameworks, adjusting their behaviours to the traffic state and its specific demand. Moreover, Fig. 5.10 depicts the energy consumption of the satellite throughout the day for the settings detailed above. We notice that BLASTER and HEURISTIC considerably reduce the daily average energy consumption of the satellite by up to 80% and 90% respectively. It is important to note that the 3GPP benchmark is configured

such that it utilises the full 30 MHz of bandwidth made available throughout the day, which leads to consistently higher energy consumption. In contrast, BLASTER and HEURISTIC use a smaller portion of the total bandwidth, as highlighted in Fig. 5.6 which results in lower energy usage. Additionally, by comparing Fig. 5.9 and Fig. 5.10, we notice that the energy consumption of a single satellite is negligible compared to the TN (less than 0.1% of the total terrestrial energy use).

5.7 Conclusion & Perspectives

In this chapter, we have presented BLASTER, a framework designed to optimise RRM in an integrated TN-NTN. BLASTER aims to control UE association, splits the bandwidth between terrestrial and non-terrestrial tiers, and manages the MBS activation and MBS transmit power level. A novel method for splitting the bandwidth between terrestrial and non-terrestrial tiers is introduced, based on the fraction of UEs associated to the latter. The proposed algorithm also highlights the critical and dynamic part the satellites play in this integrated TN-NTN, adapting their role to various traffic demands. Indeed, the non-terrestrial tier takes a prominent role in low traffic, ensuring that terrestrial MBSs offload their UEs to the satellite to enable their shutdown. Conversely, the non-terrestrial tier embraces a secondary role in high traffic, mainly acting as an outlet to cell-edge UEs, facilitating load distribution while also giving up a share of its resources to the terrestrial tier. To further enhance the practicality and scalability of our approach, we now turn our attention to revising the deterministic UE association strategy employed thus far. While effective in controlled scenarios, such a rigid association mechanism can be challenging to implement in real-world deployments due to its centralised nature. In the next chapter, we explore a ML-based solution that leverages a distributed framework to enable more adaptive and implementable UE association policies, as well as replicate the behaviour of the integrated TN-NTN from this chapter.

6

A Distributed Approach to Integrated TN-NTN Optimisation Using Online Learning Methods

6.1 Introduction

In the previous chapter, we developed a framework which dynamically adapted UE association and resource allocation based on traffic conditions to enhance the performance of integrated TN-NTN. While this solution showcases promising results, its centralised nature may hinder real-time implementation, especially in large-scale deployments such as in our studies. Indeed, it relies on a centralised optimisation process that requires global knowledge of the network state and coordination for the UE association process, power control, and resource allocation across all MBSs—including the joint optimisation of the association matrix X, which must be computed and updated centrally. To overcome this limitation, we now explore a distributed approach that preserves the adaptive capabilities of BLASTER without the need for centralised orchestration. A common approach to optimising UE association in a distributed manner is through the handover events defined by the 3GPP [112]. For example, `Event A3` is triggered when a neighbouring cell becomes offset better than the serving cell, i.e.:

$$\mathrm{M}_n + \mathrm{Of}_n + \mathrm{Oc}_n - \mathrm{Hys} > \mathrm{M}_p + \mathrm{Of}_p + \mathrm{Oc}_p + \mathrm{Off} \tag{6.1}$$

where:

- $\mathrm{M}n$, M_p respectively represent the measurement result of the neighbouring and serving cell (RSRP in our case).
- Of_n, Of_p represent the frequency offset of the neighbouring and serving cell, expressed in dB.
- Oc_n, Oc_p represent the cell individual offset (CIO) of the neighbouring and serving cell, expressed in dB.
- Off represents the offset parameter for this event, expressed in dB.
- Hys is the hysterisis parameter.

Specifically, by tuning the CIOs, the network can bias handover decisions in favour of underutilised cells to enable load balancing in a distributed manner, for example. However, such optimisation proves computationally intractable for realistic network sizes. Therefore, we propose a ML-based solution rooted in online learning theory, capable of adapting to traffic dynamics in a distributed manner.
The remainder of this chapter is structured as follows. We begin by reviewing relevant literature that has explored distributed approaches to similar optimisation challenges. Next, we formally define the optimisation problem at hand and introduce the proposed solution. Finally, we assess the performance of our approach through a comparative evaluation against two tailored benchmarks, and conclude with a summary of the key findings.

6.2 Contribution

This chapter introduces a learning-based framework, `BCOMD-NETOP`, designed to optimise the performance of integrated TN-NTN. The framework aims to dynamically adapt key control parameters—such as UE association, bandwidth allocation between terrestrial and satellite tiers, and MBS shutdown policies—based on real-time traffic conditions. The core of the method is a constrained online learning algorithm that balances EE and resource allocation fairness. Additionally, the framework employs a mirror descent algorithm named BCOMD proposed in [113] using the Tsallis entropy [114]

as the mirror map in place of the Shannon entropy [115]. This work derives novel performance guarantees specifically for the adversarial setting, extending the theoretical foundation of this approach studied most recently by Deng et al. [116], Shi & Eryilmaz [117] and Zhou & Ji [118]. Also, we propose a novel windowed estimator technique to reduce noise in gradient estimation, leading to improved empirical performance. The effectiveness of the solution is validated through simulations, demonstrating its ability to closely match offline-optimal strategies while remaining responsive to time-varying network conditions.

This chapter includes content that has been published or is under submission in the following venues:

- Published in **2025 IEEE Workshop on Signal Processing and Artificial Intelligence for Wireless Communications (SPAWC)**: *H. Alam, A. De Domenico, T. Si Salem and F. Kaltenberger, "A Multi-Armed Bandit Framework for Online Optimization in Green Integrated Terrestrial and Non-Terrestrial Networks," 2025, pp. 1-5, Surrey, UK*.
- To be Submitted to **IEEE Transactions on Wireless Communications**: *H. Alam, A. De Domenico, T. Si Salem and F. Kaltenberger, "BCOMD-NETOP: an Online Optimisation Framework for Green Integrated Terrestrial and Non-Terrestrial Networks*".

6.3 Related Works

As stated in Sect. 6.1, a number of works address the tuning of handover parameters such as CIO to enable load-aware mobility control. Classical RL approaches, such as done by Asghari et al. [119], utilise Q-learning and SARSA to adjust CIO values in real time, offering improved adaptability in dynamic environments compared to fixed-parameter schemes. Expanding on this, deep RL techniques are adopted in works like those of Alsuhli et al. [120] and Attia et al. [121], where actor-critic methods such as deep deterministic policy gradient (DDPG) and twin delayed deep deterministic (TD3) policy gradient enable continuous control over CIOs and transmission power across large-scale networks. These works reflect a broader trend toward

decentralised and distributed RL frameworks. For instance, the work by Alsuhli et al. [120] on decentralised DDPG explicitly enables MBSs to make local decisions based on their own KPIs, reducing reliance on centralised control and improving scalability in dense deployments. Similarly, Attia et al. [121] propose a layered RL architecture that can be adapted to distributed scenarios, managing both discrete and continuous action spaces in a hybrid formulation. Muñoz et al. [122] propose a fuzzy rule-based approach that enables each femtocell to autonomously adjust its behaviour based on locally observed network conditions. Meanwhile, works like that of Alsuhli et al. [123] incorporate agent-based modelling, where cells act independently but are coordinated through reinforcement mechanisms, a setup well-suited for self-organising networks (SONs).
Altogether, these studies demonstrate that, alongside centralised approaches, there are viable decentralised and distributed solutions for addressing mobility load balancing and handover optimization.

6.4 Problem Formulation

Following the approach of Chapter 5, our objective is to develop a framework that jointly optimises network SLT and TN energy consumption. This is achieved by dynamically adapting resource allocation and controlling UE association in response to network load, while ensuring that the data-rate requirements of all UEs are satisfied.

In order to do that, we are going to select, at each time slot t, an action (or *arm)* a_t among a set of n possible actions $\mathcal{A} = \{1, \dots, n\}$, which corresponds to a specific setting of $\boldsymbol{\theta} = [\varepsilon, \tau_\nu, \tau_{\text{RSRP}}, \alpha]$. Each arm influences network behaviour through a heuristic mechanism, which takes $\boldsymbol{\theta}$ as input and is described in detail in Section 6.5. Based on the selected arm, we will observe a certain cost and constraint: this is a classic representation of a multi-armed bandit (MAB) problem with bandit feedback. Indeed, in those problem settings, an oblivious adversary specifies the loss and constraint values in advance by selecting a loss vector $\mathbf{f}_t \triangleq (f_{t,a})_{a\in\mathcal{A}}$ and a constraint vector $\mathbf{g}_t \triangleq (g_{t,a})_{a\in\mathcal{A}}$ for each time slot $t \in [T]$ at the start of the game. Then, at each time slot t, we select an arm a_t, drawn according to the

probability distribution $\mathbf{x}_t$ over the action space $\mathcal{A}$, where $\mathbf{x}_t$ belongs to the $n-$dimensional simplex:

$$\Delta_n \triangleq \{\mathbf{x} \in [0,1]^n : ||\mathbf{x}||_1 = 1\}. \tag{6.2}$$

To assess network performance at time t, we define a cost function that encapsulates the primary trade-offs involved:

$$f_t(a_t, \mathbf{x}_t) = \zeta \sum_{j \in \mathcal{B}} Q_j(\boldsymbol{\theta}) - \sum_{i \in \mathcal{U}} \log\left(R_i(\boldsymbol{\theta})\right). \tag{6.3}$$

Here, $R_i(\boldsymbol{\theta})$ denotes the throughput experienced by UE i, and $Q_j(\boldsymbol{\theta})$ represents the energy consumption of MBS j, both evaluated under a given network configuration $\boldsymbol{\theta}$. The parameter ζ serves as a regularization factor that balances the trade-off between UE performance (i.e., SLT) and overall network energy consumption, accordingly to the traffic load.
Also, we define the constraint violation incurred by arm a_t as the following:

$$g_t(a_t, \mathbf{x}_t) = \frac{1}{K} \sum_{i \in \mathcal{U}} \mathbb{1}_{\{R_i(\boldsymbol{\theta}) < \rho_i\}}. \tag{6.4}$$

Without loss of generality, the values of the cost and constraint functions are scaled to lie within the ranges $[0, 1]$ and $[-1, 1]$ respectively. In particular, a negative value for the constraint function implies that every UE is satisfied. Note that a UE is also considered unsatisfied if its perceived RSRP falls below a predefined threshold $\mathrm{RSRP}_{\min}$.

Naturally, the cost distribution associated with each arm varies over time, as network demand fluctuates with changes in traffic load. For example, an arm that improves capacity under high-traffic conditions may become suboptimal during periods of low traffic, highlighting the necessity of context-aware arm selection. This inherent non-stationarity in the cost structure aligns with the adversarial bandit-feedback framework presented in [113]. Consequently, we adopt the algorithm proposed in [113], which is specifically designed to accommodate dynamic cost environments while maintaining long-term constraint satisfaction.

We define a *policy* as a sequence of actions taken based on the history of past actions, as well as previously incurred costs and constraints. Furthermore,

let $\mathbf{x}^\star$ denote the *oracle* policy, representing the sequence of actions that minimises the cumulative loss over the entire time horizon:

$$\{\mathbf{x}_t^\star\}_{t=1}^T \in \arg \min_{\{\mathbf{x}_t\}_{t=1}^T \in \times_{t=1}^T \Delta_{n,t}} \left\{ \sum_{t=1}^T f_t(a_t, \mathbf{x}_t) \right\}, \tag{6.5}$$

where $\Delta_{n,t}$ is the set of feasible points within the simplex at time t:

$$\Delta_{n,t} \triangleq \{\mathbf{x} \in \Delta_n : g_t(a_t, \mathbf{x}) \leq 0\}. \tag{6.6}$$

Therefore, our objective is to determine a policy $\boldsymbol{\pi}$ that minimises the cumulative loss relative to the oracle policy, while simultaneously satisfying time-varying constraints. Following the notation introduced in [113], we define the notions of regret and constraint violation, which constitute the primary performance metrics to be minimised:

$$\mathfrak{R}_T(\boldsymbol{\pi}) \triangleq \mathbb{E}_{\boldsymbol{\pi}} \left[\sum_{t=1}^T f_t(a_t, \boldsymbol{\pi}_t) \right] - \sum_{t=1}^T f_t(a_t, \mathbf{x}_t^*), \tag{6.7}$$

$$\mathfrak{V}_T(\boldsymbol{\pi}) \triangleq \mathbb{E}_{\boldsymbol{\pi}} \left[\sum_{t=1}^T g_t(a_t, \boldsymbol{\pi}_t) \right]. \tag{6.8}$$

The first term of (6.7) is the expected cumulative cost incurred by our policy over T time steps and represents the actual performance of our learning algorithm over time. The second term is the cumulative cost of the oracle policy. In essence, determining $\boldsymbol{\pi}$ allows us to identify the best configuration for the parameters in $\boldsymbol{\theta}$ to optimise network performance throughout the day—according to traffic load—while maintaining QoS for the UEs.

6.5 Designed Solution

In this section, we first describe the BCOMD algorithm proposed in [113], as well as the heuristic that we developed which will be embedded within the BCOMD algorithm to create the `BCOMD-NETOP` algorithm to optimise network performance. We then present the theorem that establishes bounds on both dynamic regret and constraint violation. Finally, we propose an enhancement to the `BCOMD-NETOP` algorithm through a windowed estimator approach.

6.5.1 Bandit-feedback Constrained Online Mirror Descent

In this section, we detail the BCOMD algorithm initially presented in [113]. First, we define the expected cost and constraint violation, at time t, as:

$$f_t(\mathbf{x}) \triangleq \mathbf{f}_t \cdot \mathbf{x}, \quad g_t(\mathbf{x}) \triangleq \mathbf{g}_t \cdot \mathbf{x}, \tag{6.9}$$

where $\mathbf{x} \in \Delta_n$.
The algorithm is based on a Lagrangian formulation given by:

$$\Psi(\mathbf{x}, \lambda) \triangleq f_t(\mathbf{x}) + \lambda g_t(\mathbf{x}). \tag{6.10}$$

The first term in the Lagrangian function represents the cost function, while the second term introduces a penalty for soft constraint violations, scaled by the Lagrange multiplier, which serves as a weighting factor. In the bandit-feedback setting, we construct unbiased estimators for the gradients of $f_t(\mathbf{x})$ and $g_t(\mathbf{x})$ as follows:

$$\tilde{\mathbf{f}}_t = \frac{f_t\left(a_t, \mathbf{x}_t\right)}{x_{t,a_t}} \mathbf{e}_{a_t}, \quad \tilde{\mathbf{g}}_t = \frac{g_t\left(a_t, \mathbf{x}_t\right)}{x_{t,a_t}} \mathbf{e}_{a_t}, \tag{6.11}$$

where a_t is the arm selected at time step t, and $\mathbf{e}_{a_t}$ denotes the unit basis vector corresponding to that arm.

Nevertheless, the unbounded variances of these estimators present a major obstacle to establishing reliable performance guarantees in the bandit setting. To mitigate this issue, [113] proposes the use of online mirror descent (OMD), which has demonstrated effectiveness in variance control and offers improved convergence rates compared to conventional online gradient methods.

Definition 1. *A mirror map $\Phi : \mathcal{D} \to \mathbb{R}$ is a function which verifies the following properties:*

1. *The domain $\mathcal{D}$ of Φ is a convex and open set such that the decision set Δ_n is included in its closure, and their intersection is non-empty: $\Delta_n \cap \mathcal{D} \neq \emptyset$.*

2. *The map Φ is strictly convex and differentiable over $\mathcal{D}$.*

3. *The map $\nabla\Phi(\mathbf{x}) : \mathcal{D} \to \mathbb{R}^n$ is surjective.*

4. *The gradient of Φ diverges on the boundary of $\mathcal{D}$.*

Definition 2. *Let $\Phi : \mathcal{D} \to \mathbb{R}$ denote a mirror map. The Bregman projection induced by Φ onto a convex set $\mathcal{S}$ is defined as: $\Pi_{\mathcal{S}}^{\Phi} : \mathbb{R}^n \to \mathcal{S}$*

$$\Pi_{\mathcal{S}}^{\Phi}(\mathbf{y}) \triangleq \arg\min_{\mathbf{x}\in\mathcal{S}} D_{\Phi}(\mathbf{x}, \mathbf{y}), \tag{6.12}$$

where we denote the Bregman divergence as:

$$D_{\Phi}(\mathbf{x}, \mathbf{y}) = \Phi(\mathbf{x}) - \Phi(\mathbf{y}) - \langle \nabla_{\Phi}(\mathbf{y}), \mathbf{x} - \mathbf{y} \rangle. \tag{6.13}$$

In OMD, updates are initially performed in the dual space and subsequently mapped back to the primal space using a mirror map, such as the negative Shannon entropy that is used in [113]. Each step pertaining to the BCOMD algorithm is listed in Algorithm 3 (Lines $16 \to 23$).

6.5.2 BCOMD-NETOP

The proposed framework for evaluating network performance under a given configuration $\boldsymbol{\theta}$ can be decomposed into the following steps:

1. **Initialisation:** Given the input configuration $\boldsymbol{\theta} = [\varepsilon, \tau_{\nu}, \tau_{\mathrm{RSRP}}, \alpha]$, the process begins by associating each UE to the MBS offering the highest RSRP. The resulting load on each MBS is then computed, followed by a redistribution of radio resources between terrestrial and satellite tiers according to the parameter ε.

2. **UE Association:** For each UE i, we introduce a pricing function that incorporates both the received signal power and the current load on MBS j:

$$P_i(j) = \mathrm{RSRP}_{ij} - \alpha\nu_j. \tag{6.14}$$

   A positive value of α penalises heavily loaded MBSs, thereby encouraging a more balanced load distribution across the TN. In contrast, a negative value incentivises associations with already loaded MBSs, potentially increasing the number of idle MBSs. Each UE is then associated with the MBS that maximises this pricing function.

3. **MBS Shutdown:** For each terrestrial MBS j, we verify whether the combined load of MBS j and the satellite is below the threshold τ_ν. If this condition holds, and all UEs served by j receive a satellite RSRP greater than τ_{RSRP}, the UEs are handed over to the satellite, and the MBS is shut down to conserve energy.

4. **Cost and Constraint Evaluation:** The incurred cost and constraint violations are then computed in accordance with (6.3) and (6.4).

`BCOMD-NETOP`, combining the BCOMD approach with the proposed heuristic, is outlined in Algorithm 3. It illustrates the iterative refinement of the action distribution within the OMD framework. At each iteration, the update direction is computed by combining an estimated gradient of the cost function with a weighted sum of the constraint gradient estimates (Lines $21 \rightarrow 22$). These weights are adaptively adjusted in response to the cumulative constraint violations (Line 23), rather than being fixed. This dynamic adaptation enables the policy to balance cost minimisation with constraint satisfaction over time. Moreover, the probability assigned to each action is bounded below by a predefined threshold γ, ensuring sufficient exploration.

6.5.3 Performance Guarantees

In this section, we introduce additional definitions and assumptions necessary to establish a performance guarantee for the BCOMD algorithm when using the Tsallis entropy as the mirror map.

Assumption 1. *There exists a point* $\mathbf{x} \in \Delta_n$ *such that,* $\forall\, t \in [1, T]$*, and* $\kappa > 0$*:*

$$g_t(\mathbf{x}) \leq -\kappa.$$

This assumption ensures that Slater's condition is satisfied, which is instrumental in deriving the performance guarantees presented later. In contrast to [113], which employs the negative Shannon entropy as the mirror map, we consider the Tsallis entropy, a broader generalisation that extends the classical Shannon formulation. While the negative Shannon entropy offers well-established convergence guarantees and smooth multiplicative updates,

Algorithm 3 BCOMD - NETOP

Data: Initial $\mathbf{x}_1 = (1/n)_{a \in \mathcal{A}}$, $\lambda_1 = 0$, Mirror map $\Phi : \mathbb{R}^n \to \mathbb{R}$, learning rate $\eta > 0$, $\gamma \in [0, 1/n]$, $\Omega > 0$

for $t = 1, \ldots, T$ **do**
- **Sample** action $a_t \sim \mathbf{x}_t$ `// Run Framework`
- **Data:** K UEs, L MBs, $\boldsymbol{\theta} = [\varepsilon, \tau_\nu, \tau_{\text{RSRP}}, \alpha]$.
- **Initialization:** Association done through max-RSRP
  - Compute the load for MBS
  - Redistribute the resources according to ε
  - **UE association:**
  - **for** *all UEs* u **do**
    - Associate UE u to MBS j^* such that:
      $j^* = \arg\max_j P_u(j)$ (6.14)
  - **end**
  - Recompute the load for MBS **MBS Shutdown:**
  - **for** *all MBSs* j **do**
    - **if** $\nu_j + \nu_{\text{sat}} \leq \tau_\nu$ **then**
      - **if** *RSRP from satellite of all served UEs by MBS* $j \geq \tau_{\text{RSRP}}$ **then**
        - Associate each UE to the satellite Shutdown MBS j
      - **end**
    - **end**
  - **end**
  - **Incur** $f_t(a_t, \mathbf{x}_t)$ and $g_t(a_t, \mathbf{x}_t)$; `// Bandit-feedback`
  - $\tilde{\mathbf{f}}_t \leftarrow (f_t(a_t, \mathbf{x}_t)/x_{t,a_t})\, \mathbf{e}_{a_t}$; `// Loss gradient estimate`
  - $\tilde{\mathbf{g}}_t \leftarrow (g_t(a_t, \mathbf{x}_t)/x_{t,a_t})\, \mathbf{e}_{a_t}$; `// Constraint gradient estimate`
  - $\tilde{\omega}_t \leftarrow (\Omega/x_{t,a_t})\mathbf{e}_{a_t}$; `// Bias term`
  - $\tilde{\mathbf{b}}_t \leftarrow \tilde{\boldsymbol{\omega}}_t + \tilde{\mathbf{f}}_t + \lambda_t \tilde{\mathbf{g}}_t$; `// Gradient for` $\Psi(\cdot, \lambda_t)$
  - $\mathbf{y}_{t+1} \leftarrow (\nabla\Phi)^{-1}\left(\nabla\Phi(\mathbf{x}_t) - \eta\tilde{\mathbf{b}}_t\right)$; `// Update primal action distribution`
  - $\mathbf{x}_{t+1} \leftarrow \Pi_{\Delta_{n,\gamma}}(\mathbf{y}_{t+1})$; `// Project to feasible simplex`
  - $\lambda_{t+1} \leftarrow (\lambda_t + \mu g_t(a_t))_+$; `// Update dual variable`
- **end**

it restricts the feasible domain to the interior of the probability simplex, requiring a minimum exploration level to prevent zero-probability actions. In contrast, the Tsallis entropy permits sparsity by operating over the full simplex, allowing the algorithm to fully discard suboptimal arms and better adapt to time-varying or adversarial environments. This makes it particularly well-suited for dynamic scenarios, where only a subset of configurations remains relevant at a given time.

Definition 3. *For $q \in]0,1[$, we define the Tsallis entropy as:*

$$\Phi_q(\mathbf{x}) = \frac{1}{1-q}\left[1 - \sum_{i=1}^{n} x_i^q\right] \tag{6.15}$$

Also, as affirmed at the end of Section 6.5.2, the algorithm operates over a restricted subset of the probability simplex $\Delta_{n,\gamma} = \Delta_n \cap [\gamma, 1]^n$. This restriction will also play a critical role when establishing performance guarantees later on.

Finally, as highlighted in Jadbabaie et al. [124], deriving worst-case bounds for dynamic regret without additional assumptions is generally intractable. Therefore, we impose regularity conditions to characterise the non-stationarity of the problem. Specifically, we adopt two distinct metrics to quantify non-stationarity: the *path length*, denoted by $P_T^\star \in \mathbb{R}_{\geq 0}$, which captures variations in the comparator sequence $\{\mathbf{x}_t^\star\}_{t=1}^T$ and thus indirectly reflects changes in the cost functions; and the *temporal variation* of the cost functions, denoted by $V_T \in \mathbb{R}_{\geq 0}$, which directly measures the magnitude of change in the cost functions over time:

$$P_T^\star \triangleq \sum_{t=1}^{T} \left\| \mathbf{x}_t^\star - \mathbf{x}_{t+1}^\star \right\|_1,$$
$$V_T \triangleq \sum_{t=1}^{T} \left\| \mathbf{f}_t - \mathbf{f}_{t+1} \right\|_\infty.$$

There is a subtle difference between those two measures. Indeed, path length captures the cumulative variation of the cost functions with respect to a specific comparator sequence, whereas the temporal variation directly measures the temporal changes in the cost functions themselves.

Given all the above, we can now introduce the regret bound achieved by Algorithm 3:

Theorem 1. *Let* $\eta = \frac{1}{M\sqrt{T}} \min\left\{\sqrt{P_T^*}, V_T^{\frac{1}{3}} T^{\frac{1}{6}}\right\}$, $\mu = \frac{1}{M\sqrt{T}}$ *and* $\gamma = \Theta(\frac{1}{\sqrt{T}})$, *with* M *a large enough constant such that* $\eta \leq \Omega^{-2} \leq 1$ *and* $\mu \leq 1$. *Then, the regret of policy* $\boldsymbol{\pi}$ *obtained from Algorithm 3 satisfies:*

$$\mathfrak{R}_T(\boldsymbol{\pi}) = \tilde{\mathcal{O}}\left(\min\left\{\sqrt{P_T^* T}, V_T^{\frac{1}{3}} T^{\frac{2}{3}}\right\}\right), \tag{6.16}$$

$$\mathfrak{V}_T(\boldsymbol{\pi}) = \tilde{\mathcal{O}}\left(\sqrt{T}\right). \tag{6.17}$$

Note that $\tilde{\mathcal{O}}$ *is a variant of* $\mathcal{O}$, *with logarithmic factors excluded.*

Proof. Please refer to Appendix B. □

6.5.4 Windowed Estimator

In this section, we introduce an enhancement to the BCOMD algorithm. A well-established approach to reducing estimator variance involves averaging observations over multiple time slots, thereby mitigating the inherent noise of each observation. To that end, instead of constructing the estimators of both cost and constraint functions as in (6.11), we create a new class of estimators:

$$\tilde{f}_{t,T_w} = \frac{1}{T_w}\left(\sum_{i=t-T_w}^{t} \frac{f_i(a_i, \mathbf{x}_i)}{x_{i,a_i}} \mathbf{e}_{a_i}\right). \tag{6.18}$$

In Section 6.6.2, we discuss how to set T_w empirically, and evaluate the performance of the windowed estimator within the BCOMD algorithm, in comparison to the original estimator.

6.6 Simulation Results & Analysis

In this section, we evaluate the performance of the proposed solution over a 24-hour period under varying traffic conditions. We begin by detailing the simulation settings and baseline comparisons in Section 6.6.1. Next, Section 6.6.2 investigates the effectiveness of the windowed estimator introduced in Section 6.5.4, comparing it against the original variant, followed

by an examination of the convergence behaviour of our algorithm in Section 6.6.3. Section 6.6.4 details how each parameter of $\boldsymbol{\theta}$ evolves through the iterations with the resulting policy. Lastly, we finish by analysing the impact of our algorithm on network ST and energy consumption in Section 6.6.5.

6.6.1 Simulation Settings and Benchmarks

Settings

In this study, the number of UEs varies hourly, following the traffic profile described in Chapter 5. Using a custom-built system-level simulator in compliance with 3GPP guidelines [40], [44], [91], [99]–[101], we generated 7×10^3 network snapshots per hour, resulting in a total of 168×10^3 samples across the day. For each hour, the learned policy was used to select an action, allowing us to assess the resulting network performance. The optimisation parameters took values from the following predefined discrete sets: ε and τ_ν were chosen from $[0.25,\ 0.50,\ 0.75,\ 0.85,\ 0.90]$, τ_{RSRP} from $[-80,\ -90,\ -100,\ -110,\ -120]$ dBm, and α from $[-3,\ -2,\ -1,\ 0,\ 1,\ 2,\ 3]$. Also, similarly to the previous chapter, the UEs are distributed uniformly throughout the study area, with a higher deployment density in the urban region compared to the rural one. Terrestrial MBSs are arranged in a hexagonal grid layout in both environments, following the 3GPP guidelines in [90], with denser deployment in the urban area. Finally, we assume that 80% of UEs are located indoors, in accordance with [91]. The parameter ζ is set to be inversely proportional to the number of UEs in the network. Detailed simulation parameters are provided in Table 6.1. For clarity, we use the terms `BCOMD` and `BCOMD-NETOP` interchangeably in the remainder of the analysis, referring specifically to the implementation described in Algorithm 3, unless stated explicitly.

Benchmarks

For this specific work, we compared the performance of our framework to two relevant benchmarks that are comparable:

Parameter	Value
Total Bandwidth W	40 MHz
Urban/Rural Inter-Site Distance	$500/1\,732$ m
Number of Macro BSs	$1\,776$
Satellite Altitude [40]	600 km
Number of arms n	875
Traffic model parameter λ_U	$600\,000$
Terrestrial Max Tx Power per RE $p_{\max}$ [99]	17.7 dBm
Satellite Max Tx Power per RE $p_{\max}$ [40]	15.8 dBm
Antenna gain (Terrestrial) $G_{\mathrm{T_X}}$ [100]	14 dBi
Antenna gain (Satellite) $G_{\mathrm{T_X}}$ [40]	30 dBi
Shadowing Loss (Terrestrial) SF [91]	4–8 dB
Shadowing Loss (Satellite) SF [44]	0–12 dB
Line-of-Sight Probability (Terrestrial / Satellite)	Refer to [91] / [44]
White Noise Power Density	-174 dBm/Hz
Coverage threshold $\mathrm{RSRP}_{\min}$	-120 dBm
Urban/Rural UEs distribution proportion	$40\%/60\%$
UE Antenna gain G_{UE} [44]	0 dBi

Tab. 6.1: Simulation parameters.

`Static-Opt` The `Static-Opt` benchmark, which represents the optimal fixed distribution in hindsight, is computed by solving a convex optimisation problem that minimises the average cost over the entire time horizon, subject to the averaged constraint being satisfied. This benchmark assumes full knowledge of all cost and constraint realisations in advance and thus serves as a strong baseline for assessing the performance of online algorithms under both objective and constraint metrics.

`FTL` The Follow-The-Leader (`FTL`) benchmark, in contrast, simulates a myopic strategy that selects the optimal fixed decision at each time step based on all past observations up to that point. Specifically, at each round, the decision is obtained by minimising the average of previously observed costs, subject to satisfying the corresponding averaged constraints. This benchmark reflects an adaptive baseline that reacts

to historical data, making it a useful comparator for evaluating how quickly online algorithms track changing environments.

6.6.2 Windowed Estimator Parameter Tuning and Performance Analysis

In this section, we empirically determine the optimal value of the window size T_w for the estimator introduced in (6.18), and assess its performance relative to the original (non-windowed) estimator. To this end, Fig. 6.1 presents the final time-averaged cost achieved under various choices of T_w. The results indicate that a moderate window size—specifically, $T_w^\star = 50$—yields the lowest cost, suggesting an effective balance between variance reduction and reactivity to changes in observed costs. We adopt this empirically chosen configuration as the default setting in the following experiments. Once T_w

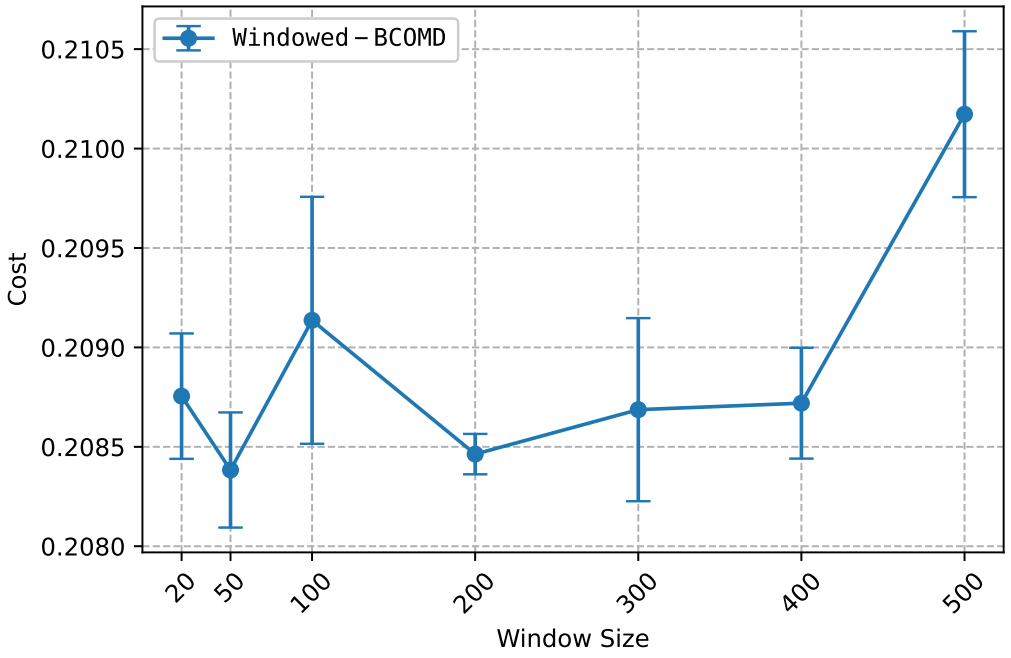

Fig. 6.1: Time-averaged cost for various window sizes.

is set, we compare the performance of the windowed and vanilla `BCOMD` estimators across a wide range of learning rates, as shown in Fig. 6.2. Similar to Fig. 6.1, we display the final time-averaged cost achieved by both

estimators under each configuration. We notice that the windowed estimator consistently yields lower costs, outperforming the vanilla estimator across the entire range of values for η, thereby empirically confirming its robustness and superiority. This improvement stems from the reduced variance in gradient estimates introduced by the windowing mechanism, which allows for more stable and effective learning updates. Additionally, we observe that the best performance is achieved for $\eta^\star = 10^{-3}$, where the final cost reaches approximately 0.10, a significant drop from nearly 0.35 observed at suboptimal settings.

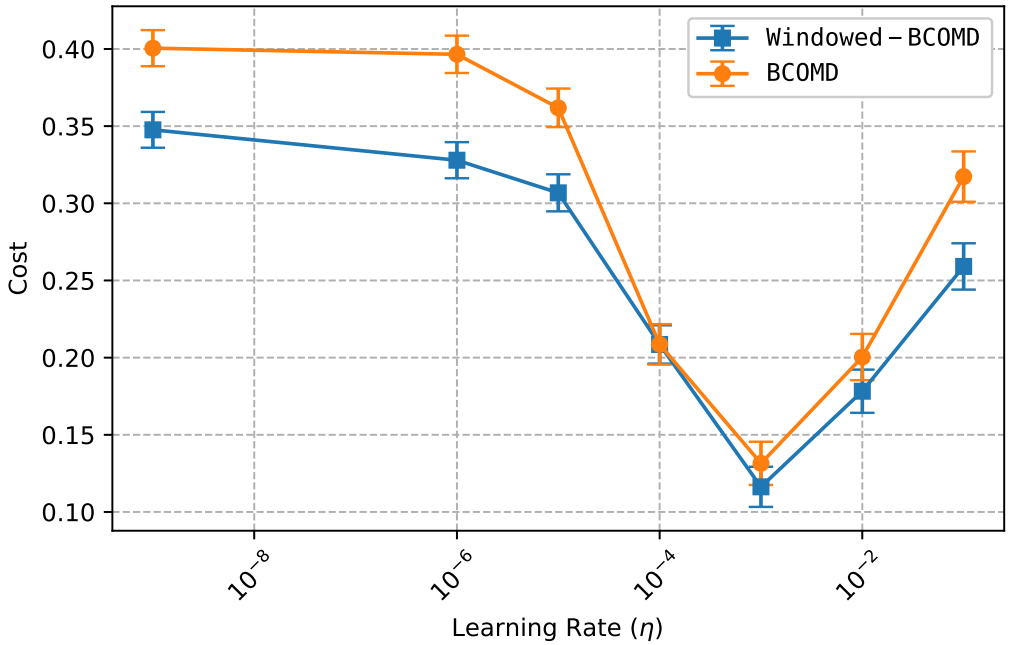

Fig. 6.2: Performance comparison of vanilla and windowed estimators under the `BCOMD` algorithm ($T_w = 50$).

Based on the findings above, we adopt the windowed estimator for all subsequent analyses, with the window size and learning rate fixed to their empirically optimal values, $T_w^\star$ and $\eta^\star$, respectively. Therefore, any reference to `BCOMD` in the following performance evaluations or comparisons will implicitly refer to this improved, windowed variant.

6.6.3 Convergence Analysis

In Fig. 6.3, we illustrate the learning dynamics of the BCOMD algorithm over the complete set of samples. Indeed, we show the time-averaged cost and constraint violations over the 168×10^3 snapshots. The plotted curves correspond to cumulative averages, with the respective confidence bounds reflected through the shaded bands. The steady decline of the cost indicates that the BCOMD algorithm progressively improves its control decisions, refining the selection policy to reduce long-term costs. Concurrently, the constraint

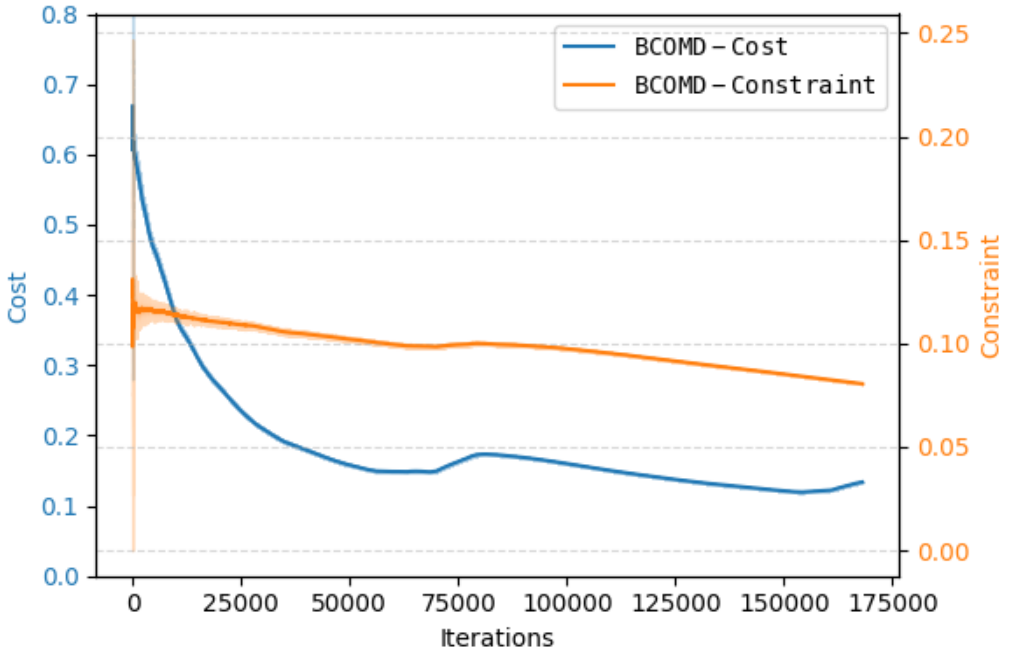

Fig. 6.3: Convergence of BCOMD: time-averaged cost and constraint violations.

violation curve shows a clear downward trend, suggesting that the algorithm adapts to the network constraints over time. This joint evolution confirms that the BCOMD algorithm not only converges over time, but also effectively balances optimisation of network performance and feasibility through online correction of its policy.

6.6.4 Control Parameters Evolution Analysis

In this section, we analyse how the policy influences the evolution of each parameter in $\boldsymbol{\theta}$ and provide insights into the resulting behaviour. From the learned probability distributions over each hour, we derive the marginal distribution of each parameter in $\boldsymbol{\theta}$, yielding the most likely value for each. These representative values are summarised in Table 6.2 across 4-hour intervals.

Parameter Value \ Hour	**0–4**	**4–8**	**8–12**	**12–16**	**16–20**	**20–24**
ε	0.85	0.85	0.75	0.75	0.75	0.85
τ_{RSRP} (dBm)	-110	-120	-100	-90	-90	-100
τ_{ν}	0.85	0.90	0.75	0.50	0.50	0.85
α	-1	-2	+1	+2	+2	-1

Tab. 6.2: Most probable parameter values across time-of-day for `BCOMD-NETOP`.

Table 6.2 reveals clear temporal trends in the parameters of $\boldsymbol{\theta}$. The resource allocation parameter ε increases during low-traffic periods and decreases during peak hours, in line with 3GPP recommendations [40]. This behaviour is a direct consequence of the cost function (6.3), which prioritises energy efficiency when traffic is low. Indeed, allocating more resources to the satellite enables the shutdown of additional terrestrial MBSs while still preserving sufficient capacity for the terrestrial MBSs to serve active UEs. During high-traffic periods, ε is reduced, though not to its minimum possible values (e.g., $\varepsilon = 0.25$ or 0.5). The algorithm learns that restricting satellite resources would hinder its ability to accommodate handovers from overloaded terrestrial cells, thereby reducing overall network capacity.

A similar adaptive trend is observed for the RSRP threshold τ_{RSRP}. The threshold is relaxed during low-traffic hours, allowing more UEs to associate with the satellite and contributing to traffic offloading and energy savings. In contrast, τ_{RSRP} becomes stricter when traffic is high, ensuring that only UEs with strong satellite signals are offloaded. This limits the resource usage of the satellite tier and ensures that offloaded UEs can still meet their data-rate requirements.

The load threshold τ_{ν} also adapts to traffic conditions, mirroring the behaviour of ε. Higher values during low demand encourage aggressive MBSs shutdowns for energy-saving purposes, while lower thresholds in peak hours

limit shutdowns to nearly idle sites, avoiding coverage gaps that could degrade user experience.
Finally, the observed behaviour of the parameter α is consistent with the intended design described in Section 6.5.2. Indeed, during low-traffic periods, α takes a negative value, effectively making heavily loaded cells more attractive and thus concentrating the load to allow for more MBSs to shut down. Conversely, in high-traffic conditions, α becomes positive to promote load balancing by steering UEs away from congested cells.

6.6.5 Network Performance Analysis

This section examines the impact of the learned policy and the resultant setting of $\boldsymbol{\theta}$ on key network performance metrics under `BCOMD-NETOP`, and compares them to the benchmarks presented above.

Impact of Satellite Network

Figure 6.4 illustrates the evolution of the proportion of UEs associated to the satellite for the three strategies: `BCOMD-NETOP`, `FTL`, and `Static-Opt`. Both `BCOMD-NETOP` and `FTL` consistently associate a higher proportion of UEs to the satellite compared to `Static-Opt` in low-traffic periods (2 to 8 AM), while during high-traffic hours, all three strategies converge to similar levels. Indeed, those dynamic strategies associate associate up to 3 times more UEs to the satellite during low-traffic period (approximately 30–35%) than the `Static-Opt` baseline (roughly 10 %). This increased usage stems from their adaptive nature—`BCOMD-NETOP` learns optimal policies over time using online feedback, while `FTL` exploits past observations to make myopic but responsive decisions. Therefore, they both identify that allocating more resources to the satellite during low traffic leads to a smaller cost, and adapt their behaviour accordingly. In contrast, as stated before, the `Static-Opt` strategy is computed offline with full knowledge of observed costs and is designed to minimise long-term average cost under constraints. As such, it conservatively utilises satellite resources, resulting in a lower overall proportion of UEs associated to the satellite. This behaviour is expected, as `Static-Opt` reflects the globally optimal resource distribution, allocating fewer resources to

the satellite to preserve them for the TN and ensure consistent constraint satisfaction. The higher satellite usage seen in BCOMD-NETOP and FTL thus reflects the ability of these strategies to dynamically adjust to varying traffic demand, offering improved short-term flexibility and responsiveness.

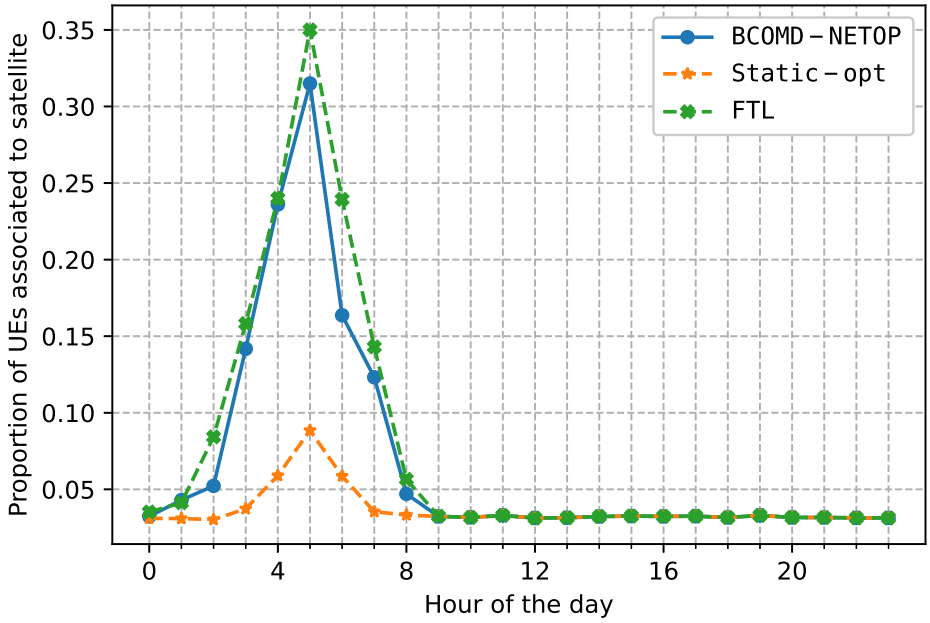

Fig. 6.4: Daily profile of the proportion of UEs associated to the satellite.

Analysis on Network Energy Consumption

Next, we study how the energy consumption of the TN fluctuates across the day. To that end, Fig. 6.5 illustrates the evolution of TN energy consumption throughout the day for the three strategies detailed previously, with an inset zooming into the low-traffic interval. Firstly, in low traffic, we notice that both BCOMD-NETOP and FTL display lower energy consumption than the Static-Opt baseline, with the energy consumption being decreased by an average of roughly 4.5 %. This difference arises from the larger share of the bandwidth being allocated to the satellite in these strategies. Indeed, a higher amount of resources are available for the satellite which leads to a greater number of UEs being handed over to it, as observed in Fig. 6.4. This results in a more proficient offloading of the traffic and leads to larger number of MBSs being shut down. Indeed, as stated previously, the more

conservative approach of `Static-Opt` regarding the satellite usage limits the potential gains in terms of energy saving during off-peak periods.
As traffic increases, the difference between `BCOMD-NETOP` and `Static-Opt` narrows down and is virtually similar. This is explained by the fact that our algorithm adapts to the traffic and identifies that the priority is to enhance the capacity of the network, which hampers energy saving. On the opposite, we notice that the `FTL` baseline consistently consumes less energy than the two other strategies, with an average decrease of $2.5\ \%$ in high traffic. This is explained by the nature of the `FTL`: as the decision is taken based on previous observations, this strategy greedily follows the optimal decision for the past, which leads to a higher proportion of the bandwidth allocated to the satellite even when the traffic increases. However, this apparent efficiency comes with hidden costs, as we will see in the following sections.

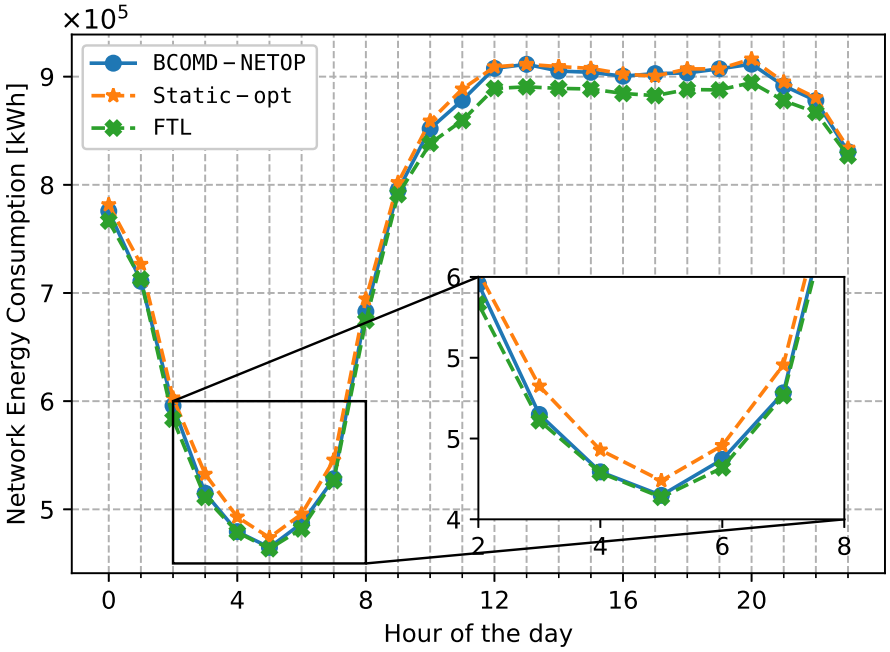

Fig. 6.5: Daily profile of the TN energy consumption.

Analysis of UE Satisfaction

We study the UE satisfaction constraint violation. To that end, Fig. 6.6 depicts the proportion of UEs who are not satisfied throughout the day for our framework as well as the two benchmarks mentioned previously. This figure clearly

shows that BCOMD-NETOP consistently achieves the lowest violation levels throughout the day, indicating its superior ability to maintain UE QoS. In contrast, FTL exhibits the highest proportion of constraint violations, particularly during high-traffic periods (approximately 10 AM to 10 PM), where its violation rate approaches $30\ \%$. This significant performance gap is primarily caused by the inherent lag in decision-making of the FTL strategy. Indeed, as a myopic, reactive algorithm, FTL relies solely on historical observations, which leads to delayed adaptations to traffic surges. Consequently, as we can see in Fig. 6.5, this strategy prioritises energy saving, which comes at the expense of the signal quality, as aggressively shutting down more MBSs in high traffic results in coverage holes and the inability to satisfy all UEs.

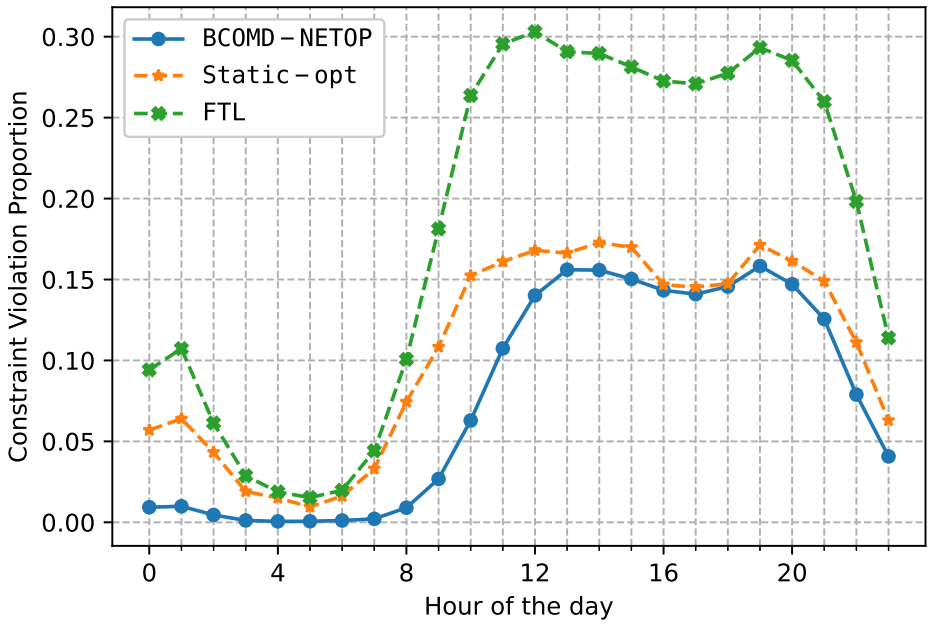

Fig. 6.6: Daily profile of the proportion of unsatisfied UEs.

On the other hand, BCOMD-NETOP outperforms both benchmarks due to its adaptive, learning-based design. Indeed, it continuously adjusts the network control parameters in response to current conditions, thereby minimising violations. The key mechanism behind this responsiveness is the primal-dual update structure, which dynamically increases the Lagrange multiplier λ_t (Line 23 in Algorithm 3) whenever constraint violations grow. This penalises

actions that lead to poor QoS and naturally steers the algorithm toward more feasible solutions in future time steps. Unlike BCOMD-NETOP, FTL lacks any such corrective mechanism—it cannot anticipate or counteract the effects of constraint violations. Meanwhile, Static-Opt, though more stable than FTL, remains a fixed offline solution and is inherently unable to react to dynamic network states.

Analysis on Network Sum Throughput

Finally, we analyse the evolution of network ST: Fig. 6.7 depicts the ST of the network throughout the day for our algorithm and the two benchmarks. During low-traffic hours, both BCOMD-NETOP and FTL outperform the Static-Opt benchmark by approximately $7\ \%$ and $8.5\ \%$ respectively.
However, as traffic ramps up during daytime, the performance gap between

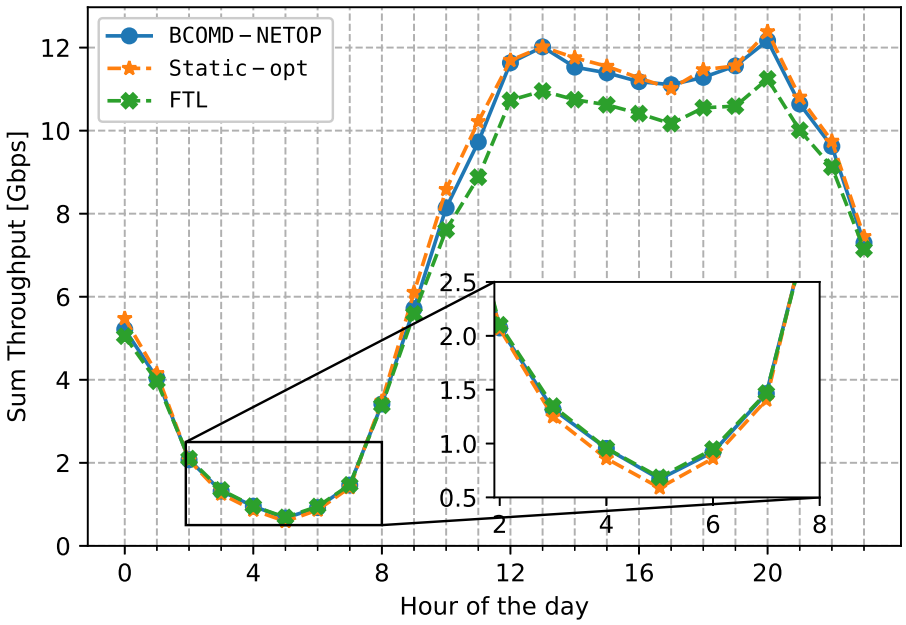

Fig. 6.7: Daily network ST profile.

BCOMD-NETOP and Static-Opt diminishes close to 0. In fact, the two strategies closely track each other, delivering comparable throughput levels on average. This indicates that BCOMD-NETOP effectively matches the globally

optimised behaviour of `Static-Opt` even under high load, thanks to its adaptive design and continual parameter tuning.
In stark contrast, the network ST under the `FTL` strategy significantly degrades, underperforming by as much as $10\ \%$ compared to the other strategies. This drop in performance directly correlates with the higher proportion of unsatisfied UEs shown in Fig. 6.6, many of whom fall into coverage holes due to the lag in adapting to rapidly shifting traffic conditions. These UEs receive negligible or null throughput, dragging down the overall system capacity. These results underscore the resilience and adaptivity of `BCOMD-NETOP` in maintaining performance in dynamic environments.

6.7 Conclusion & Perspectives

In this chapter, we introduced a comprehensive online learning framework that leverages the BCOMD algorithm to dynamically optimise network control parameters affecting UE association, bandwidth allocation, and MBS shutdown. Our proposed solution successfully adapts to fluctuating traffic conditions, prioritising energy efficiency during low-demand periods while ensuring robust UE satisfaction during high traffic. Through extensive simulations, we demonstrated that our framework closely tracks the offline optimal benchmark, achieving a near-optimal trade-off between network energy consumption and capacity in real time.
Also, we leverage a generalised Tsallis mirror map in our implementation, which enables sparse action distributions and improved adaptability in dynamic settings, compared to prior methods based on Shannon entropy. We derive formal performance guarantees for this new mirror map, establishing regret and constraint violation bounds under adversarial conditions. Additionally, we proposed a novel windowed class of estimators, which significantly improves gradient estimate stability by reducing observation noise, yielding enhanced empirical performance.

7

Conclusion & Perspectives

This thesis addressed the pressing problem of how to efficiently operate integrated TN-NTNs systems, especially under dynamic traffic conditions and stringent energy and coverage constraints. Although integrated TN-NTNs offer significant potential, prior research has generally treated the non-terrestrial tier as a static coverage enhancement layer, without leveraging its ability to dynamically support traffic load balancing or contribute to energy savings in the TN. Moreover, existing works have largely overlooked the joint optimisation of spectrum sharing between the terrestrial and non-terrestrial tiers, failing to fully exploit the flexible role that the latter tier can play, adapting its role according to time-varying network conditions and traffic demands.
In contrast, we developed an optimisation framework that demonstrated that the non-terrestrial tier can play a context-aware role: acting as a high-capacity overlay to assist with load balancing during peak hours, and serving as a resilient fallback layer that enables energy-efficient operation of the terrestrial tier during low-traffic periods. By dynamically adjusting UE association, bandwidth partitioning, and terrestrial MBS activation, the proposed framework unlocks the full potential of TN-NTNs as a self-optimising and traffic-aware architecture for next-generation networks.

In Chapter 4, after identifying the shortcomings of traditional max-RSRP association mechanisms, we developed a utility-based framework which optimises UE association using a pricing method, the terrestrial MBSs transmission power, as well as the bandwidth allocation between both terrestrial and non-terrestrial tiers in high traffic. The framework was able to distribute the load efficiently, enhancing the network SLT, and showcased the strengths of LEO satellites by reducing considerably the coverage holes. Furthermore, by analysing the scenario in which both tiers share the available bandwidth,

we highlighted the trade-off between reducing coverage gaps and maximising the network SLT.

Building on this, we developed BLASTER in Chapter 5, a novel algorithm designed to adapt the role of satellites throughout the day. By optimising a varying utility function which finds the best compromise between reducing energy consumption and enhancing network SLT depending on the traffic load, we were able to display the dynamic role satellites can play during an entire day. In low-traffic conditions, the non-terrestrial tier assumes a central role by offloading UEs from terrestrial MBSs, thereby enabling their shutdown and conserving energy. In contrast, during periods of high traffic, it shifts to a supporting role—primarily serving cell-edge UEs to ease congestion—while also reallocating part of its resources to reinforce the terrestrial tier. BLASTER demonstrated significant energy savings and enhanced throughput, while maintaining service continuity.

Finally, recognising the need for scalable and distributed solutions, we developed a comprehensive online learning framework based on the BCOMD algorithm in Chapter 6, enabling dynamic optimisation of key network control parameters, including UE association, bandwidth allocation, and MBS shutdown decisions. This framework mirrored the behaviour of BLASTER, successfully adapting to the varying traffic, while achieving results on par with oracle solutions.

Each of these contributions were rigorously evaluated against comparable benchmarks, and results consistently showed meaningful improvements in relevant metrics such as throughput, user satisfaction, and energy consumption.

These contributions not only address key limitations in the current research landscape but also align closely with the broader vision of future 6G networks. The integration of NTN technology is increasingly seen as a cornerstone of 6G, with standardisation bodies such as the 3GPP actively working to incorporate TN-NTNs into the 5G and beyond through Releases 17 to 20. While full-scale deployment of NTNs remains a long-term goal, the potential benefits are far-reaching. These include bridging the digital divide, supporting global IoT applications, enhancing resilience in disaster-prone regions, and enabling more inclusive access to connectivity—particularly for remote or underserved

populations. The frameworks presented in this thesis contribute to this trajectory by proposing practical methods for large-scale optimisation of integrated TN-NTNs.

Perspectives

Throughout our work, we identified several promising directions to explore to enhance the proposed frameworks and broaden their applicability:

BLASTER Convexity Analysis

Although BLASTER has demonstrated strong performance and there is empirical proof that the optimisation problem is convex, a formal investigation into its convexity properties remains an open challenge. Establishing whether the underlying optimisation problem is convex—or identifying convex subsets—would help provide theoretical convergence guarantees for the algorithm.

Interference Analysis

In our simulations, we primarily considered a single-satellite NTN overlaying our study area. However, in practical deployments, multiple satellites may operate concurrently, potentially causing inter-satellite and cross-link interference. Indeed, the co-existence of multiple satellites in the same area would alter the signal quality received from the non-terrestrial tier, and may lead to differing results from the one in our work. Hence, future work should incorporate interference modelling and coordination strategies in multi-satellite settings to improve the accuracy and reliability of performance evaluations.

Uplink Analysis

Our current study focuses on DL optimisation, where UE experience is often most impacted. Nevertheless, acUL performance is equally critical, especially in applications such as IoT or remote sensing. Extending the proposed models to account for UL constraints such as power limitations for example, would offer a more comprehensive network perspective.

Integrated HAPS-Satellite Layout Analysis

Building upon the foundation laid by BLASTER, our ongoing work explores the integration of an intermediate High-Altitude Platform Station (HAPS) layer into the existing TN-NTN architecture. The inclusion of HAPS introduces new modelling dimensions and challenges. For instance, when both non-terrestrial tiers (HAPS and satellites) operate within the same frequency band, inter-tier interference becomes a critical factor that can significantly degrade overall network performance. Conversely, adopting a three-way bandwidth split among terrestrial, HAPS, and satellite tiers can mitigate interference but introduces a more intricate resource allocation problem. In this latter case, maintaining fairness and managing handovers across all three tiers may require new optimisation strategies.

UAV CIO Optimisation

As discussed in Chapter 6, employing deep RL techniques to optimise the CIOs based on handover events defined by the 3GPP—as explored by Alsuhli et al. [120] and Attia et al. [121]—proves computationally intractable when applied to a coverage area as large as that of a LEO satellite beam. The sheer number of terrestrial MBSs within such a region leads to an enormous state and action space, making real-time training and inference impractical. In contrast, UAVs typically serve much smaller coverage areas, encompassing fewer terrestrial MBSs, which significantly reduces the problem complexity. This makes deep RL-based CIO optimisation a far more viable and scalable solution in UAV-assisted scenarios, and one direction of research that we would look into in the future.

Decentralised Optimisation Beyond BCOMD

A promising direction for future research involves exploring alternative decentralised learning frameworks for network control in integrated TN-NTNs. While we considered online learning methods such as BCOMD, more flexible and fine-grained approaches are emerging. In particular, the distributed combinatorial MAB framework presented by Wang et al. [125] offers a powerful paradigm for real-time, agent-level optimisation. Similar methods could enable each network node/BS to independently select from a multi-dimensional action space based on local observations and performance feedback, without requiring global coordination.

Moreover, the use of weighted reward functions within combinatorial MAB schemes could allow explicit control over the trade-offs between the different key performance indicators (KPIs) we monitor. Adapting such methods to the TN-NTN context could enhance scalability under varying traffic and mobility patterns.

8

Appendices

Appendix A - Proof of Proposition 1

First, we inject (5.9) into formula (5.10) to get:

$$\mathcal{D}(\mu) = \mathcal{L}(X^\star, \mu) = \frac{1}{2}\|X^\star\|_F^2 - \mathrm{Tr}\left(X^{\star T}\tilde{X}\right) + \frac{1}{2}\|\tilde{X}\|_F^2\left[\left(X^\star \odot \beta\right)\cdot p\right]^T \mu - \left(\mathrm{RSRP}_{\min}\cdot \mathbb{1}_K\right)^T \mu. \tag{.1}$$

Then, keeping the same notations as above, we notice that:

$$\left[\left(X^\star \odot \beta\right)\cdot p\right]^T \mu = \mathrm{Tr}\left(X^\star\left(\beta \odot p^{\mathrm{PAD}} \odot \mu^{\mathrm{PAD}}\right)^T\right), \tag{.2}$$

Indeed, developing the left component of (.2), we get:

$$\begin{aligned}
\left[\left(X^\star \odot \beta\right)\cdot p\right]^T \mu &= \left[\begin{bmatrix} x^*_{11} & \cdots & x^*_{1L} \\ \vdots & \ddots & \vdots \\ x^*_{K1} & \cdots & x^*_{KL} \end{bmatrix} \odot \begin{bmatrix} \beta_{11} & \cdots & \beta_{1L} \\ \vdots & \ddots & \vdots \\ \beta_{K1} & \cdots & \beta_{KL} \end{bmatrix} \cdot \begin{bmatrix} p_1 \\ \vdots \\ p_L \end{bmatrix}\right]^T \begin{bmatrix} \mu_1 \\ \vdots \\ \mu_L \end{bmatrix} \\
&= \left[\begin{bmatrix} x^*_{11}\beta_{11} & \cdots & x^*_{1L}\beta_{1L} \\ \vdots & \ddots & \vdots \\ x^*_{K1}\beta_{K1} & \cdots & x^*_{KL}\beta_{KL} \end{bmatrix} \cdot \begin{bmatrix} p_1 \\ \vdots \\ p_L \end{bmatrix}\right]^T \begin{bmatrix} \mu_1 \\ \vdots \\ \mu_L \end{bmatrix} \\
&= \begin{bmatrix} \sum_{j=1}^{L} x^*_{1j}\beta_{1j}p_j \\ \vdots \\ \sum_{j=1}^{L} x^*_{Kj}\beta_{Kj}p_j \end{bmatrix}^T \begin{bmatrix} \mu_1 \\ \vdots \\ \mu_L \end{bmatrix} = \sum_{i=1}^{K}\mu_i\left(\sum_{j=1}^{L} x^*_{ij}\beta_{ij}p_j\right)
\end{aligned}$$

Then, focusing on the right component of (.2), we have:

$$
\begin{aligned}
& X^{\star}\left(\beta \odot p^{\mathrm{PAD}} \odot \mu^{\mathrm{PAD}}\right)^{T} \\
&= \begin{bmatrix} x_{11}^{*} & \cdots & x_{1L}^{*} \\ \vdots & \ddots & \vdots \\ x_{K1}^{*} & \cdots & x_{KL}^{*} \end{bmatrix} \cdot \left(\begin{bmatrix} \beta_{11} & \cdots & \beta_{1L} \\ \vdots & \ddots & \vdots \\ \beta_{K1} & \cdots & \beta_{KL} \end{bmatrix} \odot \begin{bmatrix} p_1 & \cdots & p_L \\ \vdots & \ddots & \vdots \\ p_1 & \cdots & p_L \end{bmatrix} \odot \begin{bmatrix} \mu_1 & \cdots & \mu_1 \\ \vdots & \ddots & \vdots \\ \mu_K & \cdots & \mu_K \end{bmatrix} \right)^{T} \\
&= \begin{bmatrix} x_{11}^{*} & \cdots & x_{1L}^{*} \\ \vdots & \ddots & \vdots \\ x_{K1}^{*} & \cdots & x_{KL}^{*} \end{bmatrix} \begin{bmatrix} \beta_{11}p_1\mu_1 & \cdots & \beta_{1L}p_L\mu_1 \\ \vdots & \ddots & \vdots \\ \beta_{K1}p_1\mu_K & \cdots & \beta_{KL}p_L\mu_K \end{bmatrix}^{T} \\
&= \begin{bmatrix} x_{11}^{*} & \cdots & x_{1L}^{*} \\ \vdots & \ddots & \vdots \\ x_{K1}^{*} & \cdots & x_{KL}^{*} \end{bmatrix} \begin{bmatrix} \beta_{11}p_1\mu_1 & \cdots & \beta_{K1}p_1\mu_K \\ \vdots & \ddots & \vdots \\ \beta_{1L}p_L\mu_1 & \cdots & \beta_{KL}p_L\mu_K \end{bmatrix} \\
&= \begin{bmatrix} \sum_{j=1}^{L} x_{1j}^{*}\left(\beta_{1j}p_j\mu_1\right) & \cdots & \cdots \\ \vdots & \ddots & \vdots \\ \cdots & \cdots & \sum_{j=1}^{L} x_{Kj}^{*}\left(\beta_{Kj}p_j\mu_K\right) \end{bmatrix} \\
&= \begin{bmatrix} \mu_1\left(\sum_{j=1}^{L} x_{1j}^{*}\beta_{1j}p_j\right) & \cdots & \cdots \\ \vdots & \ddots & \vdots \\ \cdots & \cdots & \mu_K\left(\sum_{j=1}^{L} x_{Kj}^{*}\beta_{Kj}p_j\right) \end{bmatrix}
\end{aligned}
$$

Then, by applying the trace operator, we effectively get:

$$
\mathrm{Tr}\left(X^{\star}\left(\beta \odot p^{\mathrm{PAD}} \odot \mu^{\mathrm{PAD}}\right)^{T}\right) = \sum_{i=1}^{K} \mu_i \left(\sum_{j=1}^{L} x_{ij}^{*}\beta_{ij}p_j\right)
$$

Injecting (.2) into (.1) and noticing that , we obtain:

$$
\begin{aligned}
\mathcal{D}(\mu) = & \frac{1}{2}||X^{\star}||_F^2 - \mathrm{Tr}\left(X^{\star}\left[\tilde{X} - \beta \odot p^{\mathrm{PAD}} \odot \mu^{\mathrm{PAD}}\right]^{T}\right) \\
& - \left(RSRP_{\min} \cdot \mathbb{1}_K\right)^{T}\mu,
\end{aligned}
\tag{.3}
$$

which concludes the proof of the proposition.

Appendix B - Proof of Theorem 1

Preliminary Lemmas

Lemma 1. *The iterates produced by Algorithm 3 and the Tsallis entropy mirror map* (6.15)*, with the cost and constraint functions respectively* $\{f_s\}_{s=1}^t$ *and* $\{g_s\}_{s=1}^t$*, satisfy the following:*

$$y_{t+1} = \left[x^{q-1} - \frac{q-1}{q}\eta\tilde{b}_t\right]^{\frac{1}{q-1}}. \tag{.4}$$

Proof. Using the fact that:

$$\nabla_{\Phi_q}(x) = \frac{q}{q-1}x^{q-1}, \tag{.5}$$

we can derive the inverse function as:

$$\nabla^{-1}_{\Phi_q}(y) = \left[\frac{q-1}{q}y\right]^{\frac{1}{q-1}}. \tag{.6}$$

Then, combining with the update step in Line 19, we obtain:

$$\begin{aligned} y_{t+1} &= \left[\frac{q-1}{q}\left[\nabla_{\Phi_q}(x) - \eta\tilde{b}_t\right]\right]^{\frac{1}{q-1}} \\ &= \left[\frac{q-1}{q}\left[\frac{q}{q-1}x^{q-1} - \eta\tilde{b}_t\right]\right]^{\frac{1}{q-1}} \\ &= \left[x^{q-1} - \frac{q-1}{q}\eta\tilde{b}_t\right]^{\frac{1}{q-1}}. \end{aligned}$$

□

Lemma 2. *Under the Tsallis entropy mirror map* (6.15)*, the primal iterates of Algorithm 3 verify:*

$$\mathbb{E}\left[D_{\Phi}(x_t, y_{t+1})|\mathcal{H}_{t-1}\right] \leq \frac{3n\eta^2}{2q}\gamma^{q-2}\left[1+\lambda_t^2+\Omega^2\right], \tag{.7}$$

where $\mathcal{H}_{t-1} \triangleq \{a_1, \ldots, a_{t-1}\}$ *is the history of actions selected up to time* $t-1$*.*

Proof. We start this proof by showing that $\nabla_{\Phi_q}(x)$ is Lipschitz. Firstly, we know that:

$$\left\|\nabla_{\Phi_q}(y) - \nabla_{\Phi_q}(x)\right\|_1 = \frac{q}{1-q}\sum_{i=1}^{n}\left|y_i^{q-1} - x_i^{q-1}\right|. \tag{.8}$$

Then, we use the fact that $f(x) = x^{q-1}$ is $|q-1|\gamma^{q-2}-$Lipschitz, since $\forall i \in \{1, \ldots, n\}, x_i, y_i \in [\gamma, 1]$.

Applying the mean-value theorem to f, we get:

$$|f(y_i) - f(x_i)| = |y_i^{q-1} - x_i^{q-1}| \leq |q-1|\gamma^{q-2}|y_i - x_i|, \tag{.9}$$

where we used the fact that the derivative of f is bounded by $|q-1|\gamma^{q-2}$.

Injecting (.9) into (.8), we can upper-bound the left component as:

$$\begin{aligned}
\left\|\nabla_{\Phi_q}(y) - \nabla_{\Phi_q}(x)\right\|_1 &\leq \frac{q}{1-q}\sum_{i=1}^{n}(1-q)\gamma^{q-2}|y_i - x_i| && \text{(.10)}\\
&\leq q\sum_{i=1}^{n}\gamma^{q-2}\max_i\{y_i - x_i\} && \text{(.11)}\\
&\leq q\gamma^{q-2}\sum_{i=1}^{n}||y-x||_\infty && \text{(.12)}\\
&\leq nq\gamma^{q-2}||y-x||_\infty. && \text{(.13)}
\end{aligned}$$

Hence, we have shown that $\nabla_{\Phi_q}(x)$ is $nq\gamma^{q-2}-$ Lipschitz, which is equivalent to $\Phi_q(x)$ being $nq\gamma^{q-2}-$smooth.

However, as stated in Lemma 3.4 of Bubeck [126], a $\beta-$smooth function f verifies:

$$||f(y) - f(x) - \langle \nabla g(x), y - x \rangle||_1 \leq \frac{\beta}{2}\|y - x\|_\infty^2. \tag{.14}$$

By definition of the Bregman divergence, this implies that:

$$|D_\Phi(x, y)| \leq \frac{nq\gamma^{q-2}}{2}\|y - x\|_\infty^2 \quad \forall x, y \in \Delta_n. \tag{.15}$$

Then, using the Taylor-Young formula to approximate y_{t+1} based on (.4), we get:

$$y_{t+1} \approx x_t - \frac{\eta}{q}\tilde{b}_t. \tag{.16}$$

Therefore, we have:

$$\|y_{t+1} - x_t\|_\infty^2 \approx \|x_t - \frac{\eta}{q}\tilde{b}_t - x_t\|_\infty^2 \approx \frac{\eta^2}{q^2}\|\tilde{b}_t\|_\infty^2. \tag{.17}$$

We can then inject this previous result in the right component of (.15) to obtain:

$$D_\Phi(x_t, y_{t+1}) \leq \frac{nq\gamma^{q-2}}{2} \times \frac{\eta^2}{q^2}\|\tilde{b}_t\|_\infty^2. \tag{.18}$$

Taking the expectation and using the fact that $\tilde{b}_t = \tilde{\omega}_t + \tilde{f}_t + \lambda_t \tilde{g}_t$:

$$\mathbb{E}\left[D_\Phi(x_t, y_{t+1})|\mathcal{H}_{t-1}\right] \leq \frac{\eta^2 n\gamma^{q-2}}{2q}\mathbb{E}\left[\|\tilde{b}_t\|_\infty^2\right]. \tag{.19}$$

We notice that:

$$\begin{aligned}\|\tilde{b}_t\|_\infty^2 &= \left(\max_{a=1,\dots,n} \tilde{\omega}_{t,a} + \tilde{f}_{t,a} + \lambda_t \tilde{g}_{t,a}\right)^2 \\ &\leq (\Omega + 1 + \lambda_t)^2 \leq 3\Omega^2 + 3 + 3\lambda_t^2 \\ &\leq 3\left(1 + \lambda_t^2 + \Omega^2\right),\end{aligned}$$

where we used the fact that $(x + y + z)^2 \leq 3x^2 + 3y^2 + 3z^2$.

Finally, using this previous inequality, we obtain the result:

$$\mathbb{E}\left[D_\Phi(x_t, y_{t+1})|\mathcal{H}_{t-1}\right] \leq \frac{3n\eta^2}{2q}\gamma^{q-2}\left[1 + \lambda_t^2 + \Omega^2\right]. \tag{.20}$$

□

Lemma 3. *Under the Tsallis entropy mirror map* (6.15)*, the Bregman divergence with variables* $x, y \in \Delta_{n,\gamma}$ *is upper bounded as:*

$$D_\Phi(x, y) \leq 4\mathrm{C}_{\gamma,\mathrm{q}}, \tag{.21}$$

where $\mathrm{C}_{\gamma,\mathrm{q}} = \frac{q}{1-q}\gamma^{q-1}$.

Proof. First, let us develop the full-form expression of the Bregman divergence:

$$D_\Phi(x, y) = \frac{1}{1-q}\left[\sum_i x_i^q - \sum_i y_i^q + q\sum_{i=1}^n y_i^{q-1}(x_i - y_i)\right]. \tag{.22}$$

Then, by applying the mean-value theorem to the function $f(z) = z^q$, we know that:

$$\exists\, c \in [\min(x_i, y_i), \max(x_i, y_i)] \quad \text{s.t.} \quad x_i^q - y_i^q = f'(c)(x_i - y_i). \tag{.23}$$

Using this, we obtain:

$$\begin{aligned} D_q(x, y) &= \frac{1}{1-q}\sum_{i=1}^n \left[qc^{q-1}(x_i - y_i) + qy_i^{q-1}(x_i - y_i)\right] \\ &= \frac{q}{1-q}\sum_{i=1}^n \left[c^{q-1}(x_i - y_i) + y_i^{q-1}(x_i - y_i)\right] \\ &= \frac{q}{1-q}\sum_{i=1}^n (x_i - y_i)\left[c^{q-1} + y_i^{q-1}\right]. \end{aligned}$$

By definition of $c \in \Delta_{n,\gamma}$ and noting that $x \rightarrowtail x^{q-1}$ is a non-increasing function, we have:

$$\begin{cases} c^{q-1} \leq \gamma^{q-1} \\ y_i^{q-1} \leq \gamma^{q-1}. \end{cases}$$

This yields:

$$D_q(x, y) \leq \frac{2\,q\,\gamma^{q-1}}{1-q}\sum_{i=1}^n (x_i - y_i). \tag{.24}$$

Finally, by observing that $\|x-y\|_1 \leq \underbrace{\|x\|_1 + \|y\|_1}_{:=2}$, we get:

$$D_q(x,y) \leq 4\frac{q}{1-q}\gamma^{q-1}. \tag{.25}$$

□

Lemma 4. *Under the Tsallis entropy mirror map* (6.15)*, for all* t*, the variables* λ_t *and* x_t *in Algorithm 3 verify:*

$$\begin{aligned}\mathbb{E}\left[\Psi_t(x_t,\lambda) - \Psi_t(x,\lambda_t)\right] &\leq \mathbb{E}\left[\left(\frac{1}{\eta}D_\Phi(x_t,y_{t+1}) + \frac{\mu}{2}\right)\right] \\ &+ \mathbb{E}\left[\frac{1}{\eta}\left(D_\Phi(x,x_t) - D_\Phi(x,x_{t+1})\right) + \frac{1}{2\mu}\left((\lambda_t-\lambda)^2 - (\lambda_{t+1}-\lambda)^2\right)\right],\end{aligned}$$

for $x \in \Delta_n$, $\lambda \geq 0$.

Proof. The proof is provided in [113]. □

Lemma 5. *Under the Tsallis entropy mirror map* (6.15)*, the primal iterates of Algorithm 3 satisfy:*

$$\begin{aligned}\frac{1}{2\,\mu}\mathbb{E}\left[\lambda_{t+1}^2 - \lambda_t^2\right] \leq 2 - \kappa\mathbb{E}[\lambda_t] + \frac{1}{\eta}\mathbb{E}\left[D_\Phi(x^\star,x_t) - D_\Phi(x^\star,x_{t+1})\right] \\ + \frac{3n\eta}{2q}\,\gamma^{q-2}\left[1 + \mathbb{E}[\lambda_t^2] + \Omega^2\right] + \frac{\mu}{2}.\end{aligned}$$

for $x^* \in \Delta_n$ *satisfying Assumption 1.*

Proof. Using Lemma 4, we know that:

$$\begin{aligned}\mathbb{E}\left[\Psi_t(x_t,0) - \Psi_t(x,\lambda_t)\right] \leq \mathbb{E}\left[\frac{1}{\eta}\left(D_\Phi(x,x_t) - D_\Phi(x,x_{t+1})\right)\right] + \frac{1}{2\mu}\left[\lambda_t^2 - \lambda_{t+1}^2\right] \\ + \mathbb{E}\left[\frac{1}{\eta}D_\Phi(x_t,y_{t+1}) + \frac{\mu}{2}\right]\end{aligned}$$

$$\begin{aligned}\Leftrightarrow \frac{1}{2\mu}\left[\lambda_{t+1}^2 - \lambda_t^2\right] + \mathbb{E}\left[\Psi_t(x_t,0) - \Psi_t(x,\lambda_t)\right] \leq \mathbb{E}\left[\frac{1}{\eta}\left(D_\Phi(x,x_t) - D_\Phi(x,x_{t+1})\right)\right] \\ + \frac{1}{\eta}\mathbb{E}\left[D_\Phi(x_t,y_{t+1})\right] + \frac{\mu}{2}.\end{aligned}$$

Then, using Lemma 2, we get:

$$\frac{1}{2\mu}\left[\lambda_{t+1}^2-\lambda_t^2\right]+\mathbb{E}\left[\Psi_t(x_t,0)-\Psi_t(x,\lambda_t)\right]\leq\mathbb{E}\left[\frac{1}{\eta}\left(D_\Phi(x,x_t)-D_\Phi(x,x_{t+1})\right)\right]+\frac{3n\eta}{2q}\gamma^{q-2}\left[1+\lambda_t^2+\Omega^2\right]+\frac{\mu}{2}.$$

However, by noting that $\Psi_t(x_t,0)-\Psi_t(x,\lambda_t)=f_t(x_t)-f_t(x)-\lambda_t\,g_t(x)$ and using Assumption 1, we obtain:

$$\frac{1}{2\mu}\left[\lambda_{t+1}^2-\lambda_t^2\right]\leq 2-\kappa\mathbb{E}[\lambda_t]+\frac{1}{\eta}\mathbb{E}\left[D_\Phi(x^\star,x_t)-D_\Phi(x^\star,x_{t+1})\right]+\frac{3n\eta}{2q}\,\gamma^{q-2}\left[1+\mathbb{E}[\lambda_t^2]+\Omega^2\right]+\frac{\mu}{2}.$$

□

Lemma 6. *For a fixed $y\in\Delta_{n,\gamma}$, $D_\Phi(\cdot,y)$ is $2\,\mathrm{C}_{\gamma,\mathrm{q}}$–Lipschitz.*

Proof. Let $x',\ x^{"}\in\Delta_{n,\gamma}$, we have:

$$D_\Phi(x',y)-D_\Phi(x'',y)=\frac{1}{1-q}\Big[\sum_{i=1}^n {x_i'}^q-\sum_{i=1}^n {y_i}^q+q\sum_{i=1}^n y_i^{q-1}(x_i'-y_i)-\sum_{i=1}^n {x_i''}^q+\sum_{i=1}^n {y_i}^q-q\sum_{i=1}^n y_i^{q-1}(x_i''-y_i)\Big]$$

Then, we obtain:

$$\begin{aligned}D_\Phi(x',y)-D_\Phi(x'',y)&=\frac{1}{1-q}\Big[\sum_{i=1}^n {x_i'}^q-\sum_{i=1}^n {x_i''}^q+q\sum_{i=1}^n y_i^{q-1}x_i'-q\sum_{i=1}^n y_i^{q-1}x_i''\Big]\\&=\frac{1}{1-q}\Big[\sum_{i=1}^n({x_i'}^q-{x_i''}^q)+q\sum_{i=1}^n y_i^{q-1}\left[x_i'-x_i''\right]\Big]\end{aligned}$$

Similarly to (.23), we use the mean-value theorem to upper-bound the left component:

$$\begin{aligned}
&D_\Phi(x', y) - D_\Phi(x'', y) \\
&\leq \frac{1}{1-q}\Big[q\gamma^{q-1}\sum_{i=1}^{n}[x'_i - x''_i] + q\gamma^{q-1}\sum_{i=1}^{n}[x'_i - x''_i]\Big] \\
&\leq 2\frac{q}{1-q}\gamma^{q-1}\Big[\sum_{i=1}^{n}[x'_i - x''_i]\Big] \\
&\leq 2\frac{q}{1-q}\gamma^{q-1}\left\|x' - x''\right\|_1 .
\end{aligned}$$

□

Lemma 7. *Let $\gamma \in \mathbb{R}_{>0}$ and $\{x^\star_{t,\gamma}\}_{t=1}^T$ be the projection of the oracle sequence* (6.5) *onto $\Delta_{n,\gamma}$. Then, under the Tsallis entropy* (6.15)*, the primal decisions $\{x_t\}_{t=1}^T$ of Algorithm 3 verify the following:*

$$\sum_{t=1}^{T} D_\Phi(x^\star_{t,\gamma}, x_t) - D_\Phi(x^\star_{t,\gamma}, x_{t+1}) \leq 2\mathrm{C}_{\gamma,\mathrm{q}}\left[2 + \sum_{t=1}^{T-1}\left\|x^\star_{t+1} - x^\star_t\right\|_1\right], \qquad (.26)$$

where $\mathrm{C}_{\gamma,\mathrm{q}} = \frac{q}{1-q}\gamma^{q-1}$.

Proof. We start by rewriting the sum by extracting the first and last component to get:

$$\begin{aligned}
\sum_{t=1}^{T} D_\Phi(x^\star_{t,\gamma}, x_t) - D_\Phi(x^\star_{t,\gamma}, x_{t+1}) = &\underbrace{D_\Phi(x^\star_{1,\gamma}, x_1)}_{\leq 4\mathrm{C}_{\gamma,\mathrm{q}}\ \text{(Lemma 3)}} - \underbrace{D_\Phi(x^\star_{T,\gamma}, x_{T+1})}_{\geq 0} \\
&+ \sum_{t=1}^{T-1}\Big[D_\Phi(x^\star_{t+1,\gamma}, x_{t+1}) - D_\Phi(x^\star_{t,\gamma}, x_{t+1})\Big]
\end{aligned}$$

$$
\begin{aligned}
&\leq 4\mathrm{C}_{\gamma,\mathrm{q}} + \sum_{t=1}^{T-1} \underbrace{D_{\Phi}(x^{\star}_{t+1,\gamma}, x_{t+1}) - D_{\Phi}(x^{\star}_{t,\gamma}, x_{t+1})}_{\leq 2\mathrm{C}_{\gamma,\mathrm{q}} \left\| x^{\star}_{t+1,\gamma} - x^{\star}_{t,\gamma} \right\|_1} \\
&\leq 4\mathrm{C}_{\gamma,\mathrm{q}} + 2\mathrm{C}_{\gamma,\mathrm{q}} \sum_{t=1}^{T-1} \left\| x^{\star}_{t+1} - x^{\star}_{t} \right\|_1 \\
&\leq 2\mathrm{C}_{\gamma,\mathrm{q}} \left[2 + \sum_{t=1}^{T-1} \left\| x^{\star}_{t+1} - x^{\star}_{t} \right\|_1 \right].
\end{aligned}
$$

□

Lemma 8. *Under the Tsallis entropy* (6.15)*, the dual variables* λ_t*,* $t \in [1, T]$ *in Algorithm 3 are bounded by:*

$$
\Omega \triangleq \frac{4\mathrm{C}_{\gamma,\mathrm{q}}}{\kappa} \left(\frac{\mu}{\eta} \right) + \frac{3n}{2\kappa} \cdot \frac{\eta\, \gamma^{q-2}}{q} + \frac{1}{2\kappa}\mu + \frac{3n}{\kappa} \cdot \frac{\gamma^{q-2}}{q} + \frac{2}{\kappa} + 1, \tag{.27}
$$

where $\eta \leq \Omega^{-2}$ *and* $\mu > 0$*.*

Proof. We adopt a similar approach to the one presented in [113]. First case: $t \leq \frac{1}{\mu}$
In that case, we have:

$$
\lambda_t \leq \lambda_{t-1} + \mu \leq \mu t \leq 1 \leq \Omega.
$$

Second case: $\frac{1}{\mu} \leq t \leq T$

We prove this by contradiction: let us assume that T_0 is the first time slot for which $\lambda_{\mathrm{T}_0} > \Omega$, which implies:

$$
\lambda_{\mathrm{T}_0 - \frac{1}{\mu}} \leq \Omega < \lambda_{\mathrm{T}_0}. \tag{.28}
$$

This yields the following:

$$
\frac{1}{\mu} \sum_{t=T_0-\frac{1}{\mu}}^{T_0-1} \mathbb{E}\left[\lambda^2_{t+1} - \lambda^2_t \right] = \frac{1}{\mu}\, \mathbb{E}\left[\lambda^2_{T_0} - \lambda^2_{T_0-\frac{1}{\mu}} \right] > \Omega^2 - \Omega^2 > 0.
$$

Then, using Lemma 5, we have:

$$\frac{1}{\mu}\sum_{t=T_0-\frac{1}{\mu}}^{T_0-1}\mathbb{E}\left[\lambda_{t+1}^2-\lambda_t^2\right]\leq\sum_{t=T_0-\frac{1}{\mu}}^{T_0-1}2\Bigg[2-\kappa\,\mathbb{E}[\lambda_t]+\frac{1}{\eta}\mathbb{E}\left[D_\Phi(x^\star,x_t)-D_\Phi(x^\star,x_{t+1})\right]$$
$$+\frac{3n\eta}{2q}\gamma^{q-2}\left(1+\mathbb{E}[\lambda_t^2]+\Omega^2\right)+\frac{\mu}{2}\Bigg]$$

$$\leq 2\Bigg[\frac{2}{\mu}-\kappa\sum_{t=T_0-\frac{1}{\mu}}^{T_0-1}\mathbb{E}[\lambda_t]+\frac{1}{\eta}\underbrace{\sum_{t=T_0-\frac{1}{\mu}}^{T_0-1}\mathbb{E}\left[D_\Phi(x^\star,x_t)-D_\Phi(x^\star,x_{t+1})\right]}_{:=(\bigstar)}$$
$$+\frac{3n\eta\,\gamma^{q-2}}{2q\mu}+\frac{3n\eta\,\gamma^{q-2}}{2q}\sum_{t=T_0-\frac{1}{\mu}}^{T_0-1}\mathbb{E}[\lambda_t^2]+\frac{3n\eta\,\gamma^{q-2}}{2q\mu}\Omega^2+\frac{1}{2}\Bigg].$$

By telescoping the sum in ($\bigstar$), and applying Lemma 3, we obtain:

$$\leq 2\Bigg[\frac{2}{\mu}-\kappa\sum_{t=T_0-\frac{1}{\mu}}^{T_0-1}\mathbb{E}[\lambda_t]+\frac{4\mathrm{C}_{\gamma,\mathrm{q}}}{\eta}+\frac{3n\eta\,\gamma^{q-2}}{2q\mu}+\frac{3n\eta\,\gamma^{q-2}\Omega^2}{2q\mu}$$
$$+\frac{3n\eta\,\gamma^{q-2}}{2q}\sum_{t=T_0-\frac{1}{\mu}}^{T_0-1}\mathbb{E}[\lambda_t^2]+\frac{1}{2}\Bigg].$$

Since $\lambda_{T_0}>\Omega$, we know that we have:

$$\sum_{t=T_0-\frac{1}{\mu}}^{T_0-1}\mathbb{E}[\lambda_t]>\sum_{t=T_0-\frac{1}{\mu}}^{T_0-1}(\Omega-s\mu)=\frac{\Omega}{\mu}-\mu\sum_{t=T_0-\frac{1}{\mu}}^{T_0-1}s$$
$$>\frac{\Omega}{\mu}-\mu\,\frac{1}{\mu^2}\geq\frac{\Omega}{\mu}-\frac{1}{\mu},$$

where $s \leq \frac{1}{\mu}$.
Combined with the fact that $\sum_{t=T_0-\frac{1}{\mu}}^{T_0-1} \mathbb{E}[\lambda_t^2] \geq \frac{\Omega^2}{\mu}$, we have:

$$\frac{1}{\mu} \sum_{t=T_0-\frac{1}{\mu}}^{T_0-1} \mathbb{E}\left[\lambda_{t+1}^2 - \lambda_t^2\right] \leq 2\left[\frac{2}{\mu} - \frac{\kappa\,\Omega}{\mu} + \frac{\kappa}{\mu} + \frac{4\mathrm{C}_{\gamma,\mathrm{q}}}{\eta} + \frac{3n\eta\,\gamma^{q-2}}{2q\mu} + \frac{3n\eta\,\gamma^{q-2}\Omega^2}{q\mu} + \frac{1}{2}\right].$$

Considering $\eta \leq \Omega^{-2}$ yields:

$$0 < 2\left[\frac{2}{\mu} - \frac{\kappa\Omega}{\mu} + \frac{\kappa}{\mu} + \frac{4\mathrm{C}_{\gamma,\mathrm{q}}}{\eta} + \frac{3n\mu\,\gamma^{q-2}}{2q\mu} + \frac{3n\,\gamma^{q-2}}{q\mu} + \frac{1}{2}\right].$$

Finally, by multiplying both sides by $\frac{\mu}{2\,\kappa}$, we obtain:

$$\Omega < \frac{4\mathrm{C}_{\gamma,\mathrm{q}}}{\kappa}\left(\frac{\mu}{\eta}\right) + \frac{3n}{2\kappa} \cdot \frac{\eta\,\gamma^{q-2}}{q} + \frac{1}{2\kappa}\mu + \frac{3n}{\kappa} \cdot \frac{\gamma^{q-2}}{q} + \frac{2}{\kappa} + 1 = \Omega,$$

which is a contradiction. This hereby proves that $\lambda_t \leq \Omega$, $\forall t \in [1, T]$. □

Lemma 9. *Given a comparator sequence $\{u_t\}_{t=1}^T$ in Δ_n, we apply Algorithm 3 under the Tsallis entropy mirror map* (6.15)*. Then, we establish the following regret guarantee:*

$$\mathbb{E}\left[\sum_{t=1}^{T} f_t(a_t) - f_t(u_t)\right] \leq \left[\frac{2\mathrm{C}_{\gamma,\mathrm{q}}}{\eta_0}\left(2 + \sum_{t=1}^{T-1} \|u_t - u_{t+1}\|_1\right) + \eta_0\right]\sqrt{\beta T} + \frac{\mu T}{2} + 2(1+\Omega)\gamma\sqrt{T},$$

where $\beta = \frac{n\,\gamma^{q-2}}{q}\left(\frac{3}{2} + 3\Omega^2\right)$, $\eta = \frac{\eta_0}{\sqrt{\beta T}}$ and $\eta_0 > \sqrt{2\mathrm{C}_{\gamma,\mathrm{q}}}$.

Proof. We start by stating that:

$$\begin{aligned}\mathbb{E}\left[\sum_{t=1}^{T} f_t(a_t) - \sum_{t=1}^{T} f_t(x_t^\star)\right] &= \mathbb{E}\left[\sum_{t=1}^{T} \mathbb{E}\left[f_t(a_t) \mid \mathcal{H}_{t-1}\right] - \sum_{t=1}^{T} f_t(x_t^\star)\right] \\ &= \mathbb{E}\left[\sum_{t=1}^{T} f_t(x_t) - \sum_{t=1}^{T} f_t(x_t^\star)\right] \\ &\leq \mathbb{E}\left[\sum_{t=1}^{T} f_t(x_t) - \sum_{t=1}^{T} f_t(x_{\gamma,t}^\star)\right] + 2(1+\Omega)\gamma T.\end{aligned}$$

Then, using Lemma 4 yields:

$$\begin{aligned}\sum_{t=1}^{T} \mathbb{E}\left[\psi_t(x_t,\lambda) - \psi_t(x_{t,\gamma}^\star,\lambda_t)\right] &\leq \sum_{t=1}^{T}\left[\frac{1}{\eta}\mathbb{E}\left[D_\Phi(x_{t,\gamma}^\star,x_t) - D_\Phi(x_{t,\gamma}^\star,x_{t+1})\right]\right. \\ &\quad + \frac{\mu}{2} + \frac{1}{2\mu}\mathbb{E}\left[(\lambda-\lambda_t)^2 - (\lambda-\lambda_{t+1})^2\right] \\ &\quad \left. + \frac{1}{\eta}\mathbb{E}\left[D_\Phi(x_t,y_{t+1})\right]\right] \\ &\leq \frac{1}{\eta}\sum_{t=1}^{T}\mathbb{E}\left[D_\Phi(x_{t,\gamma}^\star,x_t) - D_\Phi(x_{t,\gamma}^\star,x_{t+1})\right] \\ &\quad + \sum_{t=1}^{T}\frac{1}{2\mu}\mathbb{E}\left[(\lambda-\lambda_t)^2 - (\lambda-\lambda_{t+1})^2\right] \\ &\quad + \sum_{t=1}^{T}\frac{1}{\eta}\mathbb{E}\left[D_\Phi(x_t,y_{t+1})\right] + \frac{\mu T}{2} \\ &\leq \frac{1}{\eta}\left[2\mathrm{C}_{\gamma,\mathrm{q}}\left(2 + \sum_{t=1}^{T-1}\left\|u_t - u_{t+1}\right\|_1\right)\right] \\ &\quad + \sum_{t=1}^{T}\frac{1}{2\mu}\mathbb{E}\left[(\lambda_t-\lambda)^2 - (\lambda_{t+1}-\lambda)^2\right] \\ &\quad + \sum_{t=1}^{T}\mathbb{E}\left[\frac{1}{\eta}D_\Phi(x_t,y_{t+1})\right] + \frac{\mu T}{2}\end{aligned}$$

By applying Lemmas 2 and 8, we obtain:

$$\begin{aligned}\sum_{t=1}^{T} \mathbb{E}\left[\psi_t(e_{a_t},\lambda) - \psi_t(x_{\gamma,t}^\star,\lambda_t)\right] &\leq \frac{1}{\eta}\left[2\mathrm{C}_{\gamma,\mathrm{q}}\left(2 + \sum_{t=1}^{T-1}\left\|\mu_t - \mu_{t-1}\right\|_1\right) + \lambda^2\right] \\ &\quad + \frac{\mu T}{2} + \frac{n\eta\,\gamma^{q-2}}{q}\left(\frac{3}{2} + 3\Omega^2\right)T.\end{aligned}$$

Then, if we set λ to 0, we have the following:

$$\sum_{t=1}^{T} \mathbb{E}\left[\psi_t(e_{a_t}, \lambda) - \psi_t(x^\star_{r_t,\gamma}, \lambda_t)\right] = \sum_{t=1}^{T} f_t(x_t) - f_t(x^\star_{r_t}) - \sum_{t=1}^{T} \lambda_t \underbrace{g_t(x^\star_{r_t})}_{\leq 2\gamma}. \quad (.29)$$

Injecting (.29) into the previous inequality, we get:

$$\sum_{t=1}^{T} f_t(x_t) - f_t(x^\star_{\gamma,t}) \leq \frac{1}{\eta}\left[2\mathrm{C}_{\gamma,\mathrm{q}}\left(2 + \sum_{t=1}^{T-1} \|u_t - u_{t-1}\|_1\right)\right] + \frac{\mu T}{2} + \frac{n\eta\,\gamma^{q-2}}{q}\left(\frac{3}{2} + 3\Omega^2\right)T + 2\gamma\Omega T.$$

Finally, we conclude the proof by setting $\beta = \frac{n\,\gamma^{q-2}}{q}\left(\frac{3}{2} + 3\Omega^2\right)$ and $\eta = \frac{\eta_0}{\sqrt{\beta T}}$. □

Lemma 10. *Given a comparator sequence $\{u_t\}_{t=1}^T$ in Δ_n, we apply Algorithm 3 under the Tsallis entropy mirror map* (6.15)*. Then, we establish the following regret guarantee:*

$$\mathbb{E}\left[\sum_{t=1}^{T} f_t(a_t) - f_t(u_t)\right] \leq 3\eta_0\sqrt{\beta T} + 2(1+\Omega)\gamma T + \frac{\mu T}{2} + \frac{2\mathrm{C}_{\gamma,\mathrm{q}} T V_T}{\eta_0^2 - 2\mathrm{C}_{\gamma,\mathrm{q}}} \quad \mathbb{1}\left\{\sum_{t=1}^{T-1} \|u_t - u_{t+1}\|_1 > \frac{\eta_0^2 - 2\mathrm{C}_{\gamma,\mathrm{q}}}{\mathrm{C}_{\gamma,\mathrm{q}}}\right\},$$

where $\beta = \frac{n\,\gamma^{q-2}}{q}\left(\frac{3}{2} + 3\Omega^2\right)$, $\eta = \frac{\eta_0}{\sqrt{\beta T}}$ and $\eta_0 > \sqrt{2\mathrm{C}_{\gamma,\mathrm{q}}}$.

Proof. We follow the proof structure of [113]. We start by defining the following set:

$$\mathcal{U}_T \triangleq \left\{\mu_1, \ldots, \mu_T \in \Delta_n \;\middle|\; \sum_{t=1}^{T-1} \|u_t - u_{t+1}\|_1 \leq \frac{\eta_0^2 - 2\mathrm{C}_{\gamma,\mathrm{q}}}{\mathrm{C}_{\gamma,\mathrm{q}}}, g_t(u_t) \leq 0,\ \forall t \in [T]\right\} \quad (.30)$$

and $u^\star$ such that:

$$\{u_t^\star\}_{t=1}^T \in \arg\min_{\{u_t\}_{t=1}^T \in \mathcal{U}_T} \sum_{t=1}^{T} f_t(u_t). \quad (.31)$$

Considering the above, we have:

$$\begin{aligned}\mathbb{E}\left[\sum_{t=1}^{T} f_t(a_t) - f_t(u_t)\right] &= \mathbb{E}\left[\sum_{t=1}^{T} \left(f_t(a_t) - f_t(u_t) + f_t(u_t^\star) - f_t(u_t^\star)\right)\right] \\ &\leq \mathbb{E}\left[\sum_{t=1}^{T} \left(f_t(a_t) - f_t(u_t^\star)\right)\right] + \sum_{t=1}^{T} \left(f_t(u_t^\star) - f_t(u_t)\right) \\ &\leq \left[\frac{2\mathrm{C}_{\gamma,\mathrm{q}}}{\eta_0}\left(2 + \sum_{t=1}^{T-1} \left\|u_t - u_{t+1}\right\|_1\right) + \eta_0\right]\sqrt{\beta T} + \frac{\mu T}{2} \\ &\quad + 2(1+\Omega)\gamma\sqrt{T} + \sum_{t=1}^{T} \left(f_t(u_t^\star) - f_t(u_t)\right),\end{aligned}$$

Since $\{u_t^\star\} \in \mathcal{U}_T$, we have:

$$\begin{aligned}\mathbb{E}\left[\sum_{t=1}^{T} f_t(a_t) - f_t(u_t)\right] &\leq 3\eta_0\sqrt{\beta T} + \frac{\mu T}{2} + 2(1+\Omega)\gamma\sqrt{T} + \sum_{t=1}^{T} f_t(u_t^\star) - f_t(u_t) \\ &\leq 3\eta_0\sqrt{\beta T} + \frac{\mu T}{2} + 2(1+\Omega)\gamma\sqrt{T} \\ &\quad + \left[\sum_{t=1}^{T} f_t(u_t^\star) - f_t(u_t)\right] \mathbb{1}\left\{\sum_{t=1}^{T-1} \left\|u_t - u_{t+1}\right\|_1 > \frac{\eta_0^2 - 2\mathrm{C}_{\gamma,\mathrm{q}}}{\mathrm{C}_{\gamma,\mathrm{q}}}\right\},\end{aligned}$$

where we used the fact that

$$\sum_{t=1}^{T} f_t(u_t^\star) - f_t(u_t) \leq 0 \quad \text{if } (u_1, \ldots, u_T) \in \mathcal{U}_T.$$

Then, similarly to the proof in [113], we partition the time horizon into B equally sized batches, assigning a fixed comparator to each batch, which leads to:

$$\sum_{t=1}^{T} \left\|\mathbf{u}_t - \mathbf{u}_{t+1}\right\|_1 \leq 2B. \tag{.32}$$

Taking $B = \frac{\eta_0^2 - 2\mathrm{C}_{\gamma,\mathrm{q}}}{\mathrm{C}_{\gamma,\mathrm{q}}}$, $x_t^\star = \arg\min_x f_t(x)$ yields:

$$\begin{aligned}
\sum_{t=1}^{T} f_t(u_t^\star) - f_t(u_t) &\leq \sum_{t=1}^{T} f_t(u_t^\star) - f_t(x_t^\star) \\
&= \sum_{k=1}^{B} \sum_{t \in \mathcal{T}_k} f_t(u_t^\star) - f_t(x_t^\star) \\
&\leq \sum_{k=1}^{B} \sum_{t \in \mathcal{T}_k} f_t(x_k^\star) - f_t(x_t^\star) \\
&\leq \frac{T}{B} \sum_{k=1}^{B} \max_{t \in \mathcal{T}_k} \left\{ f_t(x_k^\star) - f_t(x_t^\star) \right\},
\end{aligned}$$

where $t_k \in \mathcal{T}_k \triangleq \left[(k-1)\frac{T}{B} + 1, k\frac{T}{B} \right]$ is considered fixed.

Then, as proven in [113], we have for any given $t_k \in \mathcal{T}_k$:

$$f_t(x_k^\star) - f_t(x_t^\star) \leq 2 \sum_{s \in \mathcal{T}_k} \sup_{x \in \Delta_n} |f_s(x) - f_{s-1}(x)|. \tag{.33}$$

Injecting (.33), we finally get:

$$\begin{aligned}
\sum_{t=1}^{T} \left(f_t(u_t^\star) - f_t(u_t) \right) &\leq \frac{T}{B} \sum_{k=1}^{B} \max_{t \in \mathcal{T}_k} \left\{ f_t(x_k^\star) - f_t(x_t^\star) \right\} \\
&\leq 2\frac{T}{B} \sum_{k=1}^{B} \sum_{s \in \mathcal{T}_k} \sup_{x \in \Delta_n} |f_s(x) - f_{s-1}(x)| \\
&= 2\frac{T}{B} V_T = \frac{2\mathrm{C}_{\gamma,\mathrm{q}} T V_T}{\eta_0^2 - 2\mathrm{C}_{\gamma,\mathrm{q}}},
\end{aligned}$$

which concludes the proof. □

Proof of Theorem 1

Now that all the necessary lemmas are proven, we can proceed with the proof of the main theorem.

Proof. From Lemmas 9 and 10, we have the following:

$$\mathbb{E}\left[\sum_{t=1}^{T} f_t(a_t) - f_t(u_t^\star)\right] \leq \frac{\mu T}{2} + 2(1+\Omega)\gamma T + \min\left\{3\eta_0\sqrt{\beta T} + \frac{2\mathrm{C}_{\gamma,\mathrm{q}} T V_T}{\eta_0^2 - 2\mathrm{C}_{\gamma,\mathrm{q}}}; \left[\frac{2\mathrm{C}_{\gamma,\mathrm{q}}\,(2+P_T)}{\eta_0} + \eta_0\right]\sqrt{\beta T}\right\},$$

where $\eta = \frac{\eta_0}{\sqrt{\beta T}}$, for $\eta_0 = \min\left\{\sqrt{P_T^*}, V_T^{\frac{1}{3}} T^{\frac{1}{6}}\right\}$. This yields the result outlined:

$$\mathbb{E}\left[\sum_{t=1}^{T} f_t(a_t) - f_t(u_t^\star)\right] = \mathcal{O}\left(\min\left\{\sqrt{P_T^\star T},\, V_T^{1/3} T^{2/3}\right\}\right). \tag{.34}$$

For the constraint violation regret, the proof is similar to [113]. First, we notice that:

$$\frac{1}{\mu}\,\mathbb{E}\left[\lambda_{t+1} - \lambda_t \,|\, \mathcal{H}_{t-1}\right] \geq g_t(x_t).$$

Finally, for $\mu = \Theta(\frac{1}{\sqrt{T}})$, we have:

$$\begin{aligned}
\mathbb{E}\left[\sum_{t=1}^{T} g_t(a_t)\right] &= \mathbb{E}\left[\sum_{t=1}^{T} g_t(x_t)\right] \\
&\leq \mathbb{E}\left[\sum_{t=1}^{T} \frac{1}{\mu}\,\mathbb{E}\left[\lambda_{t+1} - \lambda_t \,|\, \mathcal{H}_{t-1}\right]\right] \\
&= \frac{1}{\mu}\,\mathbb{E}[\lambda_{T+1}] \leq \frac{\Omega}{\mu} \\
&= \mathcal{O}\left(\sqrt{T}\right),
\end{aligned}$$

where we used Lemma 8 and the fact that the choice of M yields $\eta \leq \Omega^{-2}$. □

Bibliography

[1] J. G. Andrews *et al.*, "What will 5g be?", *IEEE Journal on Selected Areas in Communications*, vol. 32, no. 6, pp. 1065–1082, 2014. DOI: 10.1109/JSAC.2014.2328098.

[2] T. Ahmmed *et al.*, "The digital divide in canada and the role of leo satellites in bridging the gap", *IEEE Communications Magazine*, vol. 60, no. 6, pp. 24–30, 2022. DOI: 10.1109/MCOM.001.2100795.

[3] G. Geraci *et al.*, "Integrating terrestrial and non-terrestrial networks: 3d opportunities and challenges", *IEEE Communications Magazine*, vol. 61, no. 4, pp. 42–48, 2023. DOI: 10.1109/MCOM.002.2200366.

[4] M. Benzaghta *et al.*, "Uav communications in integrated terrestrial and non-terrestrial networks", in *2022 IEEE GLOBECOM*, Dec. 2022, pp. 1–6. DOI: 10.48550/ARXIV.2208.02683.

[5] GSMA, *The 5g guide: A preference for operators*, 2019.

[6] GSMA, *5g energy efficiencies: Green is the new black*, 2020.

[7] GSMA, *Going green: Measuring the energy efficiency of mobile networks*, 2024.

[8] D. López-Pérez *et al.*, "A survey on 5g radio access network energy efficiency: Massive mimo, lean carrier design, sleep modes, and machine learning", *IEEE Communications Surveys & Tutorials*, vol. 24, no. 1, pp. 653–697, 2022. DOI: 10.1109/COMST.2022.3142532.

[9] K. T. Li *et al.*, "A techno-economic assessment and tradespace exploration of low earth orbit mega-constellations", *IEEE Communications Magazine*, vol. 61, no. 2, pp. 24–30, 2023. DOI: 10.1109/MCOM.001.2200312.

[10] L. Toka *et al.*, "Integrating the skies for 6g: Techno-economic considerations of leo, haps, and uav technologies", *IEEE Communications Magazine*, vol. 62, pp. 44–51, Nov. 2024. DOI: 10.1109/MCOM.003.2400120.

[11] O. B. Osoro *et al.*, "Sustainability assessment of low earth orbit (leo) satellite broadband mega-constellations", 2023. arXiv: 2309.02338 [astro-ph.EP].

[12] J. Li, H. Lu, K. Xue, and Y. Zhang, "Temporal netgrid model-based dynamic routing in large-scale small satellite networks", *IEEE Transactions on Vehicular Technology*, vol. 68, no. 6, pp. 6009–6021, 2019. DOI: 10.1109/TVT.2019.2910570.

[13] T. Chen *et al.*, "Network energy saving technologies for green wireless access networks", *IEEE Wireless Communications*, vol. 18, no. 5, 2011. DOI: 10.1109/MWC.2011.6056690.

[14] M. Alsabah *et al.*, "6g wireless communications networks: A comprehensive survey", *IEEE Access*, vol. 9, pp. 148 191–148 243, 2021. DOI: 10.1109/ACCESS.2021.3124812.

[15] O. Kodheli *et al.*, "Satellite communications in the new space era: A survey and future challenges", *IEEE Communications Surveys & Tutorials*, vol. 23, no. 1, pp. 70–109, 2021. DOI: 10.1109/COMST.2020.3028247.

[16] G. Wikström *et al.*, "Challenges and technologies for 6g", in *2020 2nd 6G Wireless Summit (6G SUMMIT)*, 2020, pp. 1–5. DOI: 10.1109/6GSUMMIT49458.2020.9083880.

[17] G. Gui *et al.*, "6g: Opening new horizons for integration of comfort, security, and intelligence", *IEEE Wireless Communications*, vol. 27, no. 5, pp. 126–132, 2020. DOI: 10.1109/MWC.001.1900516.

[18] U. Challita *et al.*, "Network formation in the sky: Unmanned aerial vehicles for multi-hop wireless backhauling", in *GLOBECOM 2017 - 2017 IEEE Global Communications Conference*, 2017, pp. 1–6. DOI: 10.1109/GLOCOM.2017.8254715.

[19] M. Giordani *et al.*, "Non-terrestrial networks in the 6g era: Challenges and opportunities", *IEEE Network*, vol. 35, no. 2, 2021. DOI: 10.1109/MNET.011.2000493.

[20] F. Tariq *et al.*, "A speculative study on 6g", *IEEE Wireless Communications*, vol. 27, no. 4, pp. 118–125, 2020. DOI: 10.1109/MWC.001.1900488.

[21] M. Erdelj *et al.*, "Wireless sensor networks and multi-uav systems for natural disaster management", *Computer Networks*, vol. 124, pp. 72–86, 2017, ISSN: 1389-1286. DOI: https://doi.org/10.1016/j.comnet.2017.05.021. [Online]. Available: https://www.sciencedirect.com/science/article/pii/S1389128617302220.

[22] Z. Yang *et al.*, "Energy efficient resource allocation in uav-enabled mobile edge computing networks", *IEEE Transactions on Wireless Communications*, vol. 18, no. 9, pp. 4576–4589, 2019. DOI: 10.1109/TWC.2019.2927313.

[23] F. Zhou *et al.*, "Mobile edge computing in unmanned aerial vehicle networks", *IEEE Wireless Communications*, vol. 27, no. 1, pp. 140–146, 2020. DOI: 10.1109/MWC.001.1800594.

[24] Y. Zeng *et al.*, "Cellular-connected uav: Potential, challenges, and promising technologies", *IEEE Wireless Communications*, vol. 26, no. 1, pp. 120–127, 2019. DOI: 10.1109/MWC.2018.1800023.

[25] M. M. U. Chowdhury *et al.*, *Ensuring reliable connectivity to cellular-connected uavs with up-tilted antennas and interference coordination*, 2021. arXiv: 2108.05090 [eess.SP]. [Online]. Available: https://arxiv.org/abs/2108.05090.

[26] W. Xia *et al.*, "Generative neural network channel modeling for millimeter-wave uav communication", *IEEE Transactions on Wireless Communications*, vol. 21, no. 11, pp. 9417–9431, 2022. DOI: 10.1109/TWC.2022.3176480.

[27] A. Garcia-Rodriguez *et al.*, "The essential guide to realizing 5g-connected uavs with massive mimo", *IEEE Communications Magazine*, vol. 57, no. 12, pp. 84–90, 2019. DOI: 10.1109/MCOM.001.1800919.

[28] C. D'Andrea *et al.*, "Analysis of uav communications in cell-free massive mimo systems", *IEEE Open Journal of the Communications Society*, vol. 1, pp. 133–147, 2020. DOI: 10.1109/OJCOMS.2020.2964983.

[29] A. Mohammed, A. Mehmood, F.-N. Pavlidou, and M. Mohorcic, "The role of high-altitude platforms (haps) in the global wireless connectivity", *Proceedings of the IEEE*, vol. 99, no. 11, pp. 1939–1953, 2011. DOI: 10.1109/JPROC.2011.2159690.

[30] X. Cao, P. Yang, M. Alzenad, X. Xi, D. Wu, and H. Yanikomeroglu, "Airborne communication networks: A survey", *IEEE Journal on Selected Areas in Communications*, vol. 36, no. 9, pp. 1907–1926, 2018. DOI: 10.1109/JSAC.2018.2864423.

[31] G. Djuknic *et al.*, "Establishing wireless communications services via high-altitude aeronautical platforms: A concept whose time has come?", *IEEE Communications Magazine*, vol. 35, no. 9, pp. 128–135, 1997. DOI: 10.1109/35.620534.

[32] S. Karapantazis *et al.*, "Broadband communications via high-altitude platforms: A survey", *IEEE Communications Surveys & Tutorials*, vol. 7, no. 1, pp. 2–31, 2005. DOI: 10.1109/COMST.2005.1423332.

[33] W. Saad *et al.*, "A vision of 6g wireless systems: Applications, trends, technologies, and open research problems", *IEEE Network*, vol. 34, no. 3, pp. 134–142, 2020. DOI: 10.1109/MNET.001.1900287.

[34] S. Chen *et al.*, "Vision, requirements, and technology trend of 6g: How to tackle the challenges of system coverage, capacity, user data-rate and movement speed", *IEEE Wireless Communications*, vol. 27, no. 2, pp. 218–228, 2020. DOI: 10.1109/MWC.001.1900333.

[35] N. Rajatheva *et al.*, *White paper on broadband connectivity in 6g*, 2020. arXiv: 2004.14247 [eess.SP]. [Online]. Available: https://arxiv.org/abs/2004.14247.

[36] F. Rinaldi *et al.*, "Non-terrestrial networks in 5g & beyond: A survey", *IEEE Access*, vol. 8, pp. 165 178–165 200, 2020. DOI: 10.1109/ACCESS.2020.3022981.

[37] C. Liu *et al.*, "Cell-free satellite-uav networks for 6g wide-area internet of things", *IEEE Journal on Selected Areas in Communications*, vol. 39, no. 4, pp. 1116–1131, 2021. DOI: 10.1109/JSAC.2020.3018837.

[38] Y. Wang *et al.*, "Hybrid satellite-uav-terrestrial networks for 6g ubiquitous coverage: A maritime communications perspective", *IEEE Journal on Selected Areas in Communications*, vol. 39, no. 11, pp. 3475–3490, 2021. DOI: 10.1109/JSAC.2021.3088692.

[39] M. Giordani *et al.*, "Toward 6g networks: Use cases and technologies", *IEEE Communications Magazine*, vol. 58, no. 3, pp. 55–61, 2020. DOI: 10.1109/MCOM.001.1900411.

[40] 3GPP TSG RAN, "TR 38.821, Solutions for NR to support non-terrestrial networks (NTN)", *V16.1.0*, May 2021.

[41] H.-L. Maattanen *et al.*, "5g nr communication over geo or leo satellite systems: 3gpp ran higher layer standardization aspects", in *2019 IEEE Global Communications Conference (GLOBECOM)*, 2019, pp. 1–6. DOI: 10.1109/GLOBECOM38437.2019.9014090.

[42] C.-T. Liu and J.-Y. Pan, "Optimal beamwidth for maximizing uplink coverage probability in quasi earth-fixed leo satellite communication system", *Electronics*, vol. 13, no. 7, 2024, ISSN: 2079-9292. DOI: 10.3390/electronics13071349. [Online]. Available: https://www.mdpi.com/2079-9292/13/7/1349.

[43] 3GPP TSG SA, "TS 22.261; Service requirements for the 5G system (Release 15)", *V15.9.0*, Sep. 2021.

[44] 3GPP TSG RAN, "TR 38.811, Study on New Radio (NR) to support non-terrestrial networks", *V15.4.0*, Sep. 2020.

[45] 3GPP TSG SA, "TR 22.822; Study on using satellite access in 5G (Release 16)", *V16.0.0*, Jul. 2018.

[46] 3GPP TSG SA, "TS 23.501; System architecture for the 5G System (Release 17)", *V17.7.0*, Dec. 2022.

[47] 3GPP TSG SA, "TS 23.502; Procedures for the 5G System (5GS)(Release 17)", *V17.7.0*, Dec. 2022.

[48] 3GPP TSG SA, "TS 23.503; Policy and charging control framework for the 5G System (5GS); Stage 2 (Release 17)", *V17.7.0*, Dec. 2022.

[49] 3GPP TSG RAN, "TR 38.863; Non-terrestrial networks (NTN) related RF and co-existence aspects (Release 17)", *V17.4.0*, Mar. 2025.

[50] 3GPP TSG RAN, "NR; User Equipment (UE) radio transmission and reception; Part 5: Satellite access Radio Frequency (RF) and performance requirements(Release 17)", *V17.0.0*, Jun. 2022.

[51] 3GPP TSG RAN, "NR; Satellite Access Node radio transmission and reception (Release 17)", *V17.0.0*, Jun. 2022.

[52] 3GPP TSG RAN, "NR; User Equipment (UE) radio transmission and reception; Part 5: Satellite access Radio Frequency (RF) and performance requirements(Release 18)", *V18.5.0*, Jan. 2025.

[53] 3GPP TSG RAN, "NR; Satellite Access Node radio transmission and reception (Release 18)", *V18.5.0*, Jan. 2025.

[54] G. Kwon, W. Shin, A. Conti, W. C. Lindsey, and M. Z. Win, "Access-backhaul strategy via gnb cooperation for integrated terrestrial-satellite networks", *IEEE Journal on Selected Areas in Communications*, vol. 42, no. 5, pp. 1403–1419, 2024. DOI: 10.1109/JSAC.2024.3365877.

[55] X. Li and B. Shang, "Advancing multi-connectivity in satellite-terrestrial integrated networks: Architectures, challenges, and applications", *IEEE Network*, pp. 1–1, 2025. DOI: 10.1109/MNET.2025.3546646.

[56] Y. Sadovaya *et al.*, "Enhancing service continuity in non-terrestrial networks via multi-connectivity offloading", *IEEE Communications Letters*, vol. 28, no. 10, pp. 2333–2337, 2024. DOI: 10.1109/LCOMM.2024.3434400.

[57] F. Khoramnejad and E. Hossain, "Carrier aggregation, load balancing, and backhauling in non-terrestrial networks: Generative diffusion model-based optimization", *IEEE Transactions on Wireless Communications*, vol. 24, no. 5, pp. 4483–4499, 2025. DOI: 10.1109/TWC.2025.3542126.

[58] Y. Cao, S.-Y. Lien, and Y.-C. Liang, "Deep reinforcement learning for multi-user access control in non-terrestrial networks", *IEEE Transactions on Communications*, vol. 69, no. 3, pp. 1605–1619, 2021. DOI: 10.1109/TCOMM.2020.3041347.

[59] G. Sun, Y. Wang, H. Yu, and M. Guizani, "Proportional fairness-aware task scheduling in space-air-ground integrated networks", *IEEE Transactions on Services Computing*, vol. 17, no. 6, pp. 4125–4137, 2024. DOI: 10.1109/TSC.2024.3478730.

[60] B. Lee, J.-H. Lee, and Y.-C. Ko, "Fairness-aware throughput optimization in low earth orbit satellite communication networks using a 3d spherical coordinate system", *IEEE Transactions on Wireless Communications*, vol. 23, no. 10, pp. 14 007–14 019, 2024. DOI: 10.1109/TWC.2024.3407682.

[61] A. A. Shamsabadi, A. Yadav, and H. Yanikomeroglu, "Impact of objective function on spectral efficiency in integrated haps-terrestrial networks", in *2024 IEEE International Conference on Communications Workshops (ICC Workshops)*, 2024, pp. 1895–1900. DOI: 10.1109/ICCWorkshops59551.2024.10615314.

[62] B. Di *et al.*, "Ultra-dense leo: Integrating terrestrial-satellite networks into 5g and beyond for data offloading", *IEEE Transactions on Wireless Communications*, vol. 18, no. 1, pp. 47–62, 2019. DOI: 10.1109/TWC.2018.2875980.

[63] J. Huang, Y. Yang, J. Lee, D. He, and Y. Li, "Deep reinforcement learning-based resource allocation for rsma in leo satellite-terrestrial networks", *IEEE Transactions on Communications*, vol. 72, no. 3, pp. 1341–1354, 2024. DOI: 10.1109/TCOMM.2023.3331021.

[64] F. Minani, M. Kobayashi, T. Fujihashi, *et al.*, "Channel prediction and fair resource allocation for ntn uplinks by lstm and deep reinforcement learning", *IEEE Transactions on Wireless Communications*, pp. 1–1, 2025. DOI: 10.1109/TWC.2025.3565774.

[65] W. Zhang, P. Liao, D. Yang, Q. Ye, S. Mao, and H. Zhang, " Towards Deterministic Satellite-Terrestrial Integrated Networks via Resource Adaptation and Differentiated Scheduling ", *IEEE Transactions on Mobile Computing*, no. 01, pp. 1–17, May 5555, ISSN: 1558-0660. DOI: 10.1109/TMC.2025.3574740. [Online]. Available: https://doi.ieeecomputersociety.org/10.1109/TMC.2025.3574740.

[66] D. Peng, A. Bandi, Y. Li, S. Chatzinotas, and B. Ottersten, "Hybrid beamforming, user scheduling, and resource allocation for integrated terrestrial-satellite communication", *IEEE Transactions on Vehicular Technology*, vol. 70, no. 9, pp. 8868–8882, 2021. DOI: 10.1109/TVT.2021.3097149.

[67] Y. Zhang, L. Yin, C. Jiang, and Y. Qian, "Joint beamforming design and resource allocation for terrestrial-satellite cooperation system", *IEEE Transactions on Communications*, vol. 68, no. 2, pp. 778–791, 2020. DOI: 10.1109/TCOMM.2019.2950022.

[68] B. Deng *et al.*, "Joint multigroup precoding and resource allocation in integrated terrestrial-satellite networks", *IEEE Transactions on Vehicular Technology*, vol. 68, no. 8, pp. 8075–8090, 2019. DOI: 10.1109/TVT.2019.2924669.

[69] K. Mashiko, H. Hashida, Y. Kawamoto, N. Kato, K. Yoshida, and M. Ariyoshi, "Spectral-efficient dynamic user association in leo satellite constellation-haps cooperative networks", *IEEE Transactions on Cognitive Communications and Networking*, pp. 1–1, 2025. DOI: 10.1109/TCCN.2025.3569603.

[70] Z. Jia, M. Sheng, J. Li, D. Zhou, and Z. Han, "Joint hap access and leo satellite backhaul in 6g: Matching game-based approaches", *IEEE Journal on Selected Areas in Communications*, vol. 39, no. 4, pp. 1147–1159, 2021. DOI: 10.1109/JSAC.2020.3018824.

[71] H. Dahrouj, S. Liu, and M.-S. Alouini, "Machine learning-based user scheduling in integrated satellite-haps-ground networks", *IEEE Network*, vol. 37, no. 2, pp. 102–109, 2023. DOI: 10.1109/MNET.006.2200281.

[72] S. Fu, J. Gao, and L. Zhao, "Collaborative multi-resource allocation in terrestrial-satellite network towards 6g", *IEEE Transactions on Wireless Communications*, vol. 20, no. 11, pp. 7057–7071, 2021. DOI: 10.1109/TWC.2021.3080578.

[73] F. Rinaldi *et al.*, "Cooperative resource allocation in integrated terrestrial/non-terrestrial 5g and beyond networks", in *2020 IEEE GLOBECOM*, 2020, pp. 1–6. DOI: 10.1109/GLOBECOM42002.2020.9321985.

[74] R. Liu, K. Guo, K. An, Y. Huang, F. Zhou, and S. Zhu, "Resource allocation for cognitive satellite-hap-terrestrial networks with non-orthogonal multiple access", *IEEE Transactions on Vehicular Technology*, vol. 72, no. 7, pp. 9659–9663, 2023. DOI: 10.1109/TVT.2023.3252642.

[75] R. A.Ayoubi *et al.*, "Imt to satellite stochastic interference modeling and coexistence analysis of upper 6 ghz-band service", *IEEE Open Journal of the Communications Society*, vol. 4, pp. 1156–1169, 2023. DOI: 10.1109/OJCOMS.2023.3275114.

[76] T.-S. R. Niloy *et al.*, "Interference analysis of coexisting 5g networks and ngso fss receivers in the 12-ghz band", *IEEE Wireless Communications Letters*, vol. 12, no. 9, pp. 1528–1532, 2023. DOI: 10.1109/LWC.2023.3281769.

[77] E. Kim, I. P. Roberts, and J. G. Andrews, "Feasibility analysis of in-band coexistence in dense leo satellite communication systems", *IEEE Transactions on Wireless Communications*, vol. 24, no. 2, pp. 1663–1677, 2025. DOI: 10.1109/TWC.2024.3511660.

[78] T. S. R. Niloy, Z. Hasan, R. Smith, V. R. Anapana, and V. K. Shah, "Context-aware spectrum coexistence of terrestrial beyond 5g networks in satellite bands", in *2024 IEEE International Symposium on Dynamic Spectrum Access Networks (DySPAN)*, 2024, pp. 231–239. DOI: 10.1109/DySPAN60163.2024.10632816.

[79] A. Alidadi Shamsabadi, A. Yadav, O. Abbasi, and H. Yanikomeroglu, "Handling interference in integrated haps-terrestrial networks through radio resource management", *IEEE Wireless Communications Letters*, vol. 11, no. 12, pp. 2585–2589, 2022. DOI: 10.1109/LWC.2022.3210435.

[80] M. M. Rahman, M. Z. Hassan, J. H. Reed, and L. Liu, "Joint interference management and traffic offloading in integrated terrestrial and non-terrestrial networks", *IEEE Transactions on Communications*, pp. 1–1, 2025. DOI: 10.1109/TCOMM.2025.3529659.

[81] A. A. Shamsabadi *et al.*, "Enhancing next-generation urban connectivity: Is the integrated haps-terrestrial network a solution?", *IEEE Communications Letters*, vol. 28, no. 5, pp. 1112–1116, 2024. DOI: 10.1109/LCOMM.2024.3370698.

[82] X. Zhu, C. Jiang, L. Kuang, N. Ge, and J. Lu, "Non-orthogonal multiple access based integrated terrestrial-satellite networks", *IEEE Journal on Selected Areas in Communications*, vol. 35, no. 10, pp. 2253–2267, 2017. DOI: 10.1109/JSAC.2017.2724478.

[83] S. A. Torrens, V. Petrov, and J. M. Jornet, "Modeling interference from millimeter wave and terahertz bands cross-links in low earth orbit satellite networks for 6g and beyond", *IEEE Journal on Selected Areas in Communications*, vol. 42, no. 5, pp. 1371–1386, 2024. DOI: 10.1109/JSAC.2024.3365894.

[84] L. Lei, A. Wang, E. Lagunas, *et al.*, "Spatial–temporal resource optimization for uneven-traffic leo satellite systems: Beam pattern selection and user scheduling", *IEEE Journal on Selected Areas in Communications*, vol. 42, no. 5, pp. 1279–1291, 2024. DOI: 10.1109/JSAC.2024.3383445.

[85] D. Kim, J. Park, J. Choi, and N. Lee, *Spectrum sharing between low earth orbit satellite and terrestrial networks: A stochastic geometry perspective analysis*, 2024. arXiv: 2408.12145 [eess.SP]. [Online]. Available: https://arxiv.org/abs/2408.12145.

[86] Y. Zhang *et al.*, "Resource allocation in terrestrial-satellite-based next generation multiple access networks with interference cooperation", *IEEE Journal on Selected Areas in Communications*, vol. 40, no. 4, pp. 1210–1221, 2022. DOI: 10.1109/JSAC.2022.3145810.

[87] J. Li, K. Xue, D. S. L. Wei, J. Liu, and Y. Zhang, "Energy efficiency and traffic offloading optimization in integrated satellite/terrestrial radio access networks", *IEEE Transactions on Wireless Communications*, vol. 19, no. 4, pp. 2367–2381, 2020. DOI: 10.1109/TWC.2020.2964236.

[88] M. Benzaghta, S. Ammar, D. López-Pérez, B. Shihada, and G. Geraci, *Data-driven cellular mobility management via bayesian optimization and reinforcement learning*, 2025. arXiv: 2505.21249 [cs.IT]. [Online]. Available: https://arxiv.org/abs/2505.21249.

[89] C. Huang, G. Chen, P. Xiao, Y. Xiao, Z. Han, and J. A. Chambers, "Joint offloading and resource allocation for hybrid cloud and edge computing in sagins: A decision assisted hybrid action space deep reinforcement learning approach", *IEEE Journal on Selected Areas in*

Communications, vol. 42, no. 5, pp. 1029–1043, 2024. DOI: 10.1109/JSAC.2024.3365899.

[90] 3GPP TSG RAN, "TR 36.942, E-UTRA; Radio Frequency (RF) system scenarios", *V10.2.0*, Feb. 2010.

[91] 3GPP TSG RAN, "TR 38.901, Study on channel model for frequencies from 0.5 to 100 GHz ", *V17.0.0*, Mar. 2022.

[92] G. Auer *et al.*, "How much energy is needed to run a wireless network?", *IEEE Wireless Communications*, vol. 18, no. 5, pp. 40–49, 2011. DOI: 10.1109/MWC.2011.6056691.

[93] N. Piovesan *et al.*, "Machine learning and analytical power consumption models for 5g base stations", *IEEE Communications Magazine*, vol. 60, no. 10, pp. 56–62, 2022. DOI: 10.1109/MCOM.001.2200023.

[94] D. Lopez-Perez *et al.*, "Data-driven energy efficiency modeling in large-scale networks: An expert knowledge and ml-based approach", *IEEE Transactions on Machine Learning in Communications and Networking*, vol. PP, pp. 1–1, Jan. 2024. DOI: 10.1109/TMLCN.2024.3407691.

[95] Q. Ye *et al.*, "User association for load balancing in heterogeneous cellular networks", *IEEE Transactions on Wireless Communications*, vol. 12, no. 6, pp. 2706–2716, 2013. DOI: 10.1109/TWC.2013.040413.120676.

[96] K. Shen *et al.*, "Distributed pricing-based user association for downlink heterogeneous cellular networks", *IEEE Journal on Selected Areas in Communications*, vol. 32, no. 6, pp. 1100–1113, 2014. DOI: 10.1109/JSAC.2014.2328143.

[97] S. Boyd *et al.*, "Subgradient methods", *lecture notes of EE392o, Stanford University, Autumn Quarter*, vol. 2004, Jan. 2003.

[98] W. Yu *et al.*, "Multicell coordination via joint scheduling, beamforming, and power spectrum adaptation", *IEEE Transactions on Wireless Communications*, vol. 12, no. 7, pp. 1–14, 2013. DOI: 10.1109/TWC.2013.052313.121128.

[99] 3GPP TSG RAN, "TR 36.814, E-UTRA; Further advancements for E-UTRA physical layer aspects", *V9.2.0*, Mar. 2017.

[100] 3GPP TSG RAN, "TR 36.931, E-UTRA; Radio Frequency (RF) requirements for LTE Pico Node B", *V17.0.0*, Mar. 2022.

[101] 3GPP TSG RAN, "TR 36.763, Study on Narrow-Band Internet of Things (NB-IoT) / enhanced Machine Type Communication (eMTC) support for Non-Terrestrial Networks (NTN) ", *V17.0.0*, Jun. 2021.

[102] E. Oh *et al.*, "Dynamic base station switching-on/off strategies for green cellular networks", *IEEE transactions on wireless communications*, vol. 12, no. 5, pp. 2126–2136, 2013.

[103] X. Chen *et al.*, "Energy-efficiency oriented traffic offloading in wireless networks: A brief survey and a learning approach for heterogeneous cellular networks", *IEEE Journal on Selected Areas in Communications*, vol. 33, no. 4, pp. 627–640, 2015.

[104] S. Kaiming *et al.*, "Flexible multiple base station association and activation for downlink heterogeneous networks", *IEEE Signal Processing Letters*, vol. 24, no. 10, pp. 1498–1502, Oct. 2017. DOI: 10.1109/lsp.2017.2738027.

[105] W. Teng *et al.*, "Joint optimization of base station activation and user association in ultra dense networks under traffic uncertainty", *IEEE Transactions on Communications*, vol. 69, no. 9, pp. 6079–6092, 2021. DOI: 10.1109/TCOMM.2021.3090794.

[106] C. E. Kement *et al.*, "Sustaining dynamic traffic in dense urban areas with high altitude platform stations (haps)", *IEEE Communications Magazine*, vol. 61, no. 7, pp. 150–156, 2023. DOI: 10.1109/MCOM.001.2200584.

[107] B. Çiloğlu *et al.*, *Cell switching in haps-aided networking: How the obscurity of traffic loads affects the decision*, 2024. arXiv: 2405.00387 [cs.NI].

[108] T. Song *et al.*, "High altitude platform stations: The new network energy efficiency enabler in the 6g era", in *2024 IEEE WCNC*, 2024, pp. 1–6. DOI: 10.1109/WCNC57260.2024.10571153.

[109] Y. Shi *et al.*, "Group sparse beamforming for green cloud-ran", *Wireless Communications, IEEE Transactions on*, vol. 13, Oct. 2013. DOI: 10.1109/TWC.2014.040214.131770.

[110] J. B. Rosen, "The gradient projection method for nonlinear programming. part i. linear constraints", *Journal of the Society for Industrial and Applied Mathematics*, vol. 8, no. 1, pp. 181–217, 1960. DOI: 10.1137/0108011.

[111] N. Parikh *et al.*, "Proximal algorithms", *Found. Trends Optim.*, vol. 1, no. 3, pp. 127–239, Jan. 2014, ISSN: 2167-3888.

[112] 3GPP TSG RAN, "TR 36.331, E-UTRA; Radio Resource Control (RRC); Protocol Specification", *V8.6.0*, Jul. 2009.

[113] T. S. Salem, "Adversarial multi-armed bandits with constraints in dynamic environments", *Under Submission Process*, 2025.

[114] C. Tsallis, "Possible generalization of Boltzmann-Gibbs statistics", *Journal of Statistical Physics*, vol. 52, no. 1-2, pp. 479–487, Jul. 1988. DOI: 10.1007/BF01016429.

[115] C. E. Shannon, "A mathematical theory of communication", *The Bell System Technical Journal*, vol. 27, no. 3, pp. 379–423, 1948. DOI: 10.1002/j.1538-7305.1948.tb01338.x.

[116] Y. Deng *et al.*, *Interference constrained beam alignment for time-varying channels via kernelized bandits*, 2022. arXiv: 2207.00908 [cs.NI]. [Online]. Available: https://arxiv.org/abs/2207.00908.

[117] Z. Shi and A. Eryilmaz, "A bayesian approach for stochastic continuum-armed bandit with long-term constraints", in *Proceedings of The 25th International Conference on Artificial Intelligence and Statistics*, G. Camps-Valls, F. J. R. Ruiz, and I. Valera, Eds., ser. Proceedings of Machine Learning Research, vol. 151, PMLR, Mar. 2022, pp. 8370–8391. [Online]. Available: https://proceedings.mlr.press/v151/shi22c.html.

[118] X. Zhou and B. Ji, *On kernelized multi-armed bandits with constraints*, 2022. arXiv: 2203.15589 [cs.LG]. [Online]. Available: https://arxiv.org/abs/2203.15589.

[119] M. Z. Asghari *et al.*, "Reinforcement learning based mobility load balancing with the cell individual offset", in *2021 IEEE 93rd Vehicular Technology Conference (VTC2021-Spring)*, 2021, pp. 1–5. DOI: 10.1109/VTC2021-Spring51267.2021.9448785.

[120] G. Alsuhli *et al.*, "Mobility load management in cellular networks: A deep reinforcement learning approach", *IEEE Transactions on Mobile Computing*, vol. 22, no. 3, pp. 1581–1598, 2023. DOI: 10.1109/TMC.2021.3107458.

[121] B. Salama Attia *et al.*, "Self-optimized agent for load balancing and energy efficiency: A reinforcement learning framework with hybrid action space", *IEEE Open Journal of the Communications Society*, vol. 5, pp. 4902–4919, 2024. DOI: 10.1109/OJCOMS.2024.3429284.

[122] P. Muñoz *et al.*, "Fuzzy rule-based reinforcement learning for load balancing techniques in enterprise lte femtocells", *IEEE Transactions on Vehicular Technology*, vol. 62, no. 5, pp. 1962–1973, 2013. DOI: 10.1109/TVT.2012.2234156.

[123] G. Alsuhli and other, "Optimized power and cell individual offset for cellular load balancing via reinforcement learning", in *2021 IEEE Wireless Communications and Networking Conference (WCNC)*, 2021, pp. 1–7. DOI: 10.1109/WCNC49053.2021.9417360.

[124] A. Jadbabaie *et al.*, "Online Optimization : Competing with Dynamic Comparators", in *Proceedings of the Eighteenth International Conference on Artificial Intelligence and Statistics*, G. Lebanon and S. V. N. Vishwanathan, Eds., ser. Proceedings of Machine Learning Research, vol. 38, San Diego, California, USA: PMLR, May 2015, pp. 398–406.

[125] R. Wang *et al.*, *D-lora: A distributed parameter adaptation scheme for lora network*, 2025. arXiv: 2501.12589 [cs.NI]. [Online]. Available: https://arxiv.org/abs/2501.12589.

[126] S. Bubeck, *Convex optimization: Algorithms and complexity*, 2015. arXiv: 1405.4980 [math.OC]. [Online]. Available: https://arxiv.org/abs/1405.4980.